Evidence of VHE Gamma-Ray Emission from the Pulsar Nebula around PSR B1509-58

(PSR B1509-58に伴うパルサーネブラからの超高エネルギーガンマ線放射の証拠)

Takashi Sako

Abstract

The gamma-ray pulsar PSR B1509-58 and its surrounding nebulae have been observed by using the 3.8m imaging Čerenkov telescope of the *CANGAROO* collaboration. The observations have been carried out during the years 1996 and 1997 in Woomera, South Australia at the gamma-ray threshold energies of 4 TeV and 1.5 TeV, respectively. Very high-energy gamma-rays are detected in the 1997 data with 4.1 σ significance. The estimated gamma-ray flux is $(3.1 \pm 0.8) \times 10^{-12}\,\mathrm{cm}^{-2}\mathrm{s}^{-1}$ at energies above 1.5 TeV. On the other hand, it was possible only to set a 3σ upper limit of $2.0 \times 10^{-12}\,\mathrm{cm}^{-2}\mathrm{s}^{-1}$ above 4.0 TeV from the observations of 1996. No significant pulsation modulated with the pulsar period has been found in either the 1996 or the 1997 data.

Our results when combined with X-ray observations lead to a value of the magnetic field strength $\simeq 10\ \mu$G, consistent with the equipartition value, in the X-ray nebula surrounding the pulsar. This field strength is much weaker than the one in the Crab nebula.

This is the first evidence of VHE gamma-ray emission from a non-*EGRET* pulsar. It underscores the power of a new criterion for the search for VHE gamma-ray sources, *i.e.*, X-ray synchrotron nebulae driven by young rotation-powered pulsars.

Contents

List of Figures

List of Tables

Chapter 1

Introduction

High-energy phenomena are some of the most interesting aspect in the universe. They provide us with laboratories in extreme physical conditions, which we can not artificially achieve. Cosmic rays, products of such high-energy phenomena, indicate the existence of huge accelerators in the universe. However, due to the magnetic field in the Galaxy, cosmic rays cannot travel directly in a straight line from the accelerators to the Earth. Therefore, it is difficult to find the direction of acceleration sites of cosmic rays from observations on cosmic rays themselves, except in the case of the highest energy cosmic rays whose paths are scarcely bent by magnetic field [23]. It is a long standing problem to identify regions where cosmic rays are accelerated. Information about the acceleration sites of cosmic rays can be also derived by non-thermal photons. Non-thermal photons are expected to be produced at the acceleration sites of cosmic rays through interactions between particles and field. Here, there is no difficulty of the path bending since photons are neutral particles. While there is a difficulty to distinguish non-thermal radiations from thermal radiations in lower energy photons, high-energy gamma-rays truely represent non-thermal phenomena. The importance of gamma-ray astronomy was first pointed out by Hayakawa [21] and Morrison [44]. They predicted some possible gamma-ray sources, which were also possible acceleration sites of cosmic-rays. Although the predictions were made in an early day, only a few satellite experiments have succeeded in finding gamma-ray sources with high confidence levels before 1990's. Twenty-five gamma-ray sources were known, all detected by the *COS-B* satellite above 100 MeV energy region [64] until the launch of the *CGRO (Compton Gamma-Ray Observatory)* satellite in 1991. On the other hand, ground based obser-

vations have reported some detections of sporadic gamma-ray sources at TeV and PeV energies (see [50], for a review). But the detection of a steady gamma-ray emission at a high confidence level was first realized by the *Whipple* Observatory using Imaging Air Čerenkov Telescope in 1989 from the Crab nebula [80].

In 1990's, gamma-ray astronomy has largely developed along two ways. First, the success of the *CGRO* provided us various informations of high-energy phenomena seen through gamma-rays. Especially, the *EGRET* experiment, which observes the highest energy part (30MeV – 30GeV) in the satellite, has found 157 gamma-ray sources in this energy region [71] [72]. Fifty-five of the 157 sources are known to be active galactic nuclei (AGNs) outside of our Galaxy, five are pulsars and five are considered to be supernova remnants (SNRs) [12]. Besides 157 sources, two more pulsars have been found [52] [51]. Approximately a hundred of the sources are still unidentified with any objects known at other wavelengths. Many of these unidentified gamma-ray sources are distributed along the galactic plane and are possibly associated with SNRs or pulsar driven nebulae. However, since the accuracy of the source localization of the *EGRET* is limited to an order of a degree [69], a drastic increase of the number of identifications cannot be expected. So far the young spin-powered pulsars and the AGNs are the typical classes of the objects detected by the *EGRET* in and outside of our Galaxy, respectively.

The other way of the development of gamma-ray astronomy is also progressed with the detections of the gamma-ray emissions from pulsars/nebulae and AGNs. After the detection of the Very High-Energy (VHE) ($>$ 300 GeV) gamma-rays from the Crab nebula by the *Whipple* group, as mentioned above, several ground based telescopes have succeeded to follow it up (see [81], for a review). On the other hand, the outbursts from the AGNs, Mrk421 and Mrk501, have been also detected by the plural VHE gamma-ray telescopes together with instruments operating at other wavelengths [38] and [49]. After these results, VHE gamma-ray observations have begun to play an important role in astronomy. The present gamma-ray sources detected in the energy ranges of satellite and ground based telescopes are shown in Figure 1.1.

The *CANGAROO* telescope, being operated in the southern hemisphere, has the ability to investigate VHE gamma-ray sources in the galactic disc near the galactic center. Besides

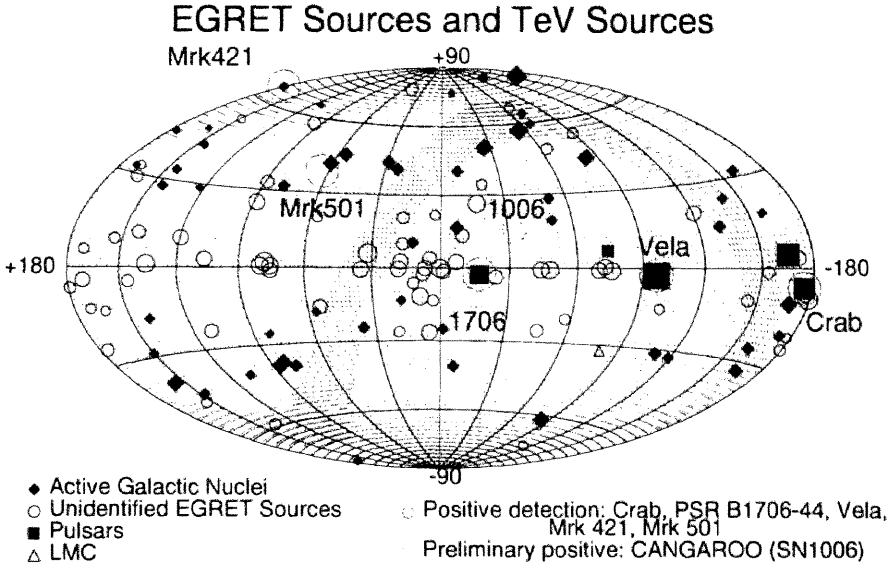

Figure 1.1: Gamma-ray sources detected in the *EGRET* and VHE energy range. Five large circles show the positive detected VHE gamma-ray sources. A middle size cirle shows preliminary source, SN1006. The meshed areas in the left and right show the coverages of the *Whipple* and the *CANGAROO*, respectively.

the Crab nebula [66], PSR B1706-44 [34] and the Vela pulsar [84] are also found to be VHE gamma-ray sources by the *CANGAROO* group. These VHE gamma-rays are understood as emissions from the pulsar nebulae and not from the pulsar magnetosphere [19]. In a pulsar nebula, the first order Fermi acceleration is thought to occur in a shock between a pulsar wind and supernova ejecta or interstellar matter. Studies of emissions from pulsar nebulae should give us good examples to develop particle acceleration models in a shock. Besides the positive detections, an upper limit to the VHE gamma-ray flux is also set for PSR B1055-52 by the *CANGAROO* group, well below the extrapolation of the *EGRET* result [63]. Other *EGRET* pulsars seen in the northern hemisphere, Geminga and PSR B1951+32, were observed by the *Whipple* group and upper limits are obtained [1] [61] for both the objects. Now the study of pulsars and their surrounding nebulae in VHE gamma-ray region comes as a next step after the studies of the *EGRET* pulsars.

It is not necessary that a VHE gamma-ray emitter has a detectable flux in the *EGRET* energy region. Most of the VHE gamma-rays emitted from the present known sources are thought to be result of inverse Compton scattering by relativistic electrons or positrons. Such relativistic electrons (positrons) are expected to emit synchrotron radiation in the X-ray energy range.

(Details depend on the magnetic field strength and the maximum energy of the accelerated particles in the emission region.) Observations of X-ray synchrotron radiation provide us with important information in the studies of VHE gamma-rays. Fortunately, the launches of the two advanced X-ray satellites, the *ASCA* and the *ROSAT*, make it possible to provide spectral and morphological informations of synchrotron X-ray sources with high precisions. With a high sensitivity up to higher energy (> 2 keV) X-rays, the *ASCA* satellite has found synchrotron X-ray emissions from many pulsar nebulae and supernova remnants [32] [36]. These observations encourage us (the *CANGAROO* group) to observe them in VHE energy region.

PSR B1509-58, the object studied in this thesis, is a pulsar detected in radio [82], X-ray [42] and low energy gamma-rays (< 1 MeV) [3]. Around the pulsar, a synchrotron X-ray nebula is found by Seward *et al.* [58], Tamura *et al.* [65] and Trussoni *et al.* [76]. Although an excess of the gamma-ray signals from the direction of this pulsar is found by the *EGRET* with low significance, only an upper limit to high-energy gamma-ray flux has been set by Brazier *et al.* [5] and Fierro [13]. (Details of this object are described in Section 3.4.) The flux of VHE gamma-rays from this object emitted through inverse Compton scattering has been predicted by du Plessis *et al.* [47] to be well within the sensitivity of the *CANGAROO* telescope. The *CANGAROO* group have observed this object in 1996 and 1997 and the results of the analysis are described in this thesis. This is the first evidence of VHE gamma-ray emission from the pulsar/nebula, which is not detected by the *EGRET*.

This thesis is planned as follows. In Chapter 2, the observational concepts and technique of VHE gamma-ray astronomy are introduced. In Chapter 3, physical processes taking place in VHE gamma-ray sources are described. I will concentrate on pulsars and their surrounding environments (nebulae and supernova remnants) as sources. Details of the specific target in this thesis, PSR B1509-58/SNR MSH15-52 are also described in this Chapter. The *CANGAROO* Experiment is explained in Chapter 4 and observation summary is also given in this Chapter. In Chapter 5, the method and the results of analysis are presented. After statistical and physical discussions in Chapter 6, conclusions are summarized in Chapter 7. Finally, potential target sources for future VHE gamma-ray observations are discussed in Chapter 8.

Chapter 2

Very High Energy Gamma-Ray Astronomy

Since the energy spectrum of non-thermal photons follows a power law, photon flux rapidly decreases with increasing an energy. For example, in an observation of a gamma-ray source with a typical flux of 1×10^{-12} cm^{-2} s^{-1} above 1 TeV using a satellite detector having a 1 m^2 effective area, only 0.3 photons can be detected during an year. Detectors with large effective areas, instead of satellite detectors, are necessary for observations in the Very-High Energy (VHE) region. Extensive Air Showers make it possible to realize such observations with large effective areas.

2.1 Extensive Air Showers

A high-energy primary particle such as a proton or a gamma-ray interacts with molecules in the atmosphere of the Earth. Successive cascade of interactions produces a large number of secondary particles. This phenomenon is called an *Extensive Air Shower*. The cascade develops until the energy of secondary particles becomes insufficient to produce next generation of particles. Once the number of the particles reaches the maximum at some altitude, it eventually decreases with further penetration in the atmosphere. In the case of an EAS initiated by a VHE ($\sim$ TeV) primary particle, the secondary particles cannot arrive at the ground level. Therefore it is actually the tertiary particles, which are Čerenkov photons radiated by the relativistic charged secondary particles, that are detected in VHE gamma-ray observations.

Details of this process are described in the next section. By detecting only a small fraction of these secondary (tertiary) particles at a ground-based observatory, we can obtain information about the primary particle. It means that the effective area of the detector for detecting VHE gamma-rays becomes enlarged to the transverse size of an EAS, which is of the order of several 10^4 m^2.

Characteristics of the EAS development are different between the two sorts of primary particles, *i.e.*, electromagnetic components (gamma-rays, electrons and positrons) and hadrons. An EAS originated by an electromagnetic particle develops following pure electromagnetic processes, while an EAS originated by a hadron is a combination of electromagnetic and hadronic interactions. Differences of these two developments of EASs are schematically represented in Figure 2.1 and typical features simulated using Monte Carlo calculations are shown in Figure 2.2. An obvious difference between the two is found in a transverse extension. A hadron initiated shower involves processes of pion production, which produce pions having large transverse momenta. A neutral pion immediately decays in two gamma-rays, which produce electromagnetic cascades. A charged pion interacts with another molecule to produce a successive hadronic cascade, unless it decays into a muon and a neutrino before an interaction. On the other hand, an EAS originated by an electromagnetic particle develops in the atmosphere with small transverse momentum. Distribution of Čerenkov photons at the ground level naturally reflects this difference in the developments of EASs.

2.2 Čerenkov radiation from Extensive Air Shower

Since the refractive index in the atmosphere is slightly larger than unity, n = 1.00029 (at 1 atm, 0°C), a relativistic charged particle, whose speed exceeds the speed of light in the medium, emits Čerenkov photons at a small angle from its moving direction. The emission angle of the Čerenkov photons, θ, is obtained from,

$$cos\theta = \frac{1}{n\beta} . \tag{2.1}$$

Here, n is the refractive index of the air and β is the velocity of the particle in units of the

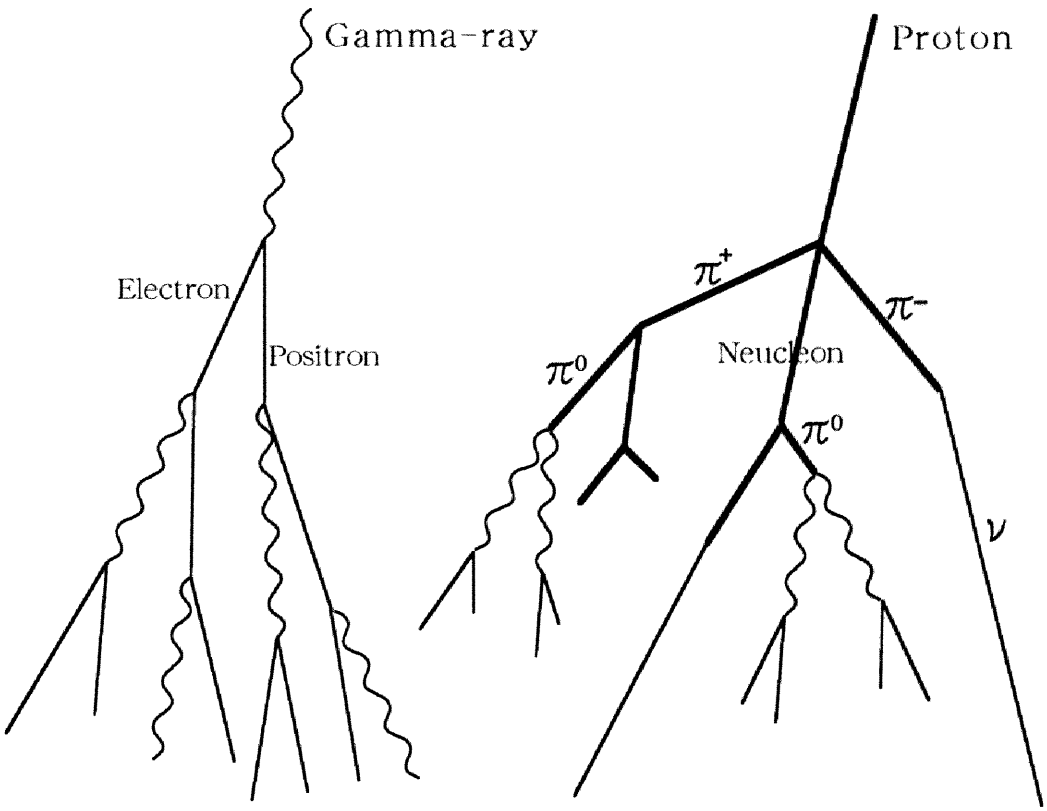

Figure 2.1: Schematic views of developments of EASs. a) Development of a gamma-ray shower. b) Development of a proton shower.

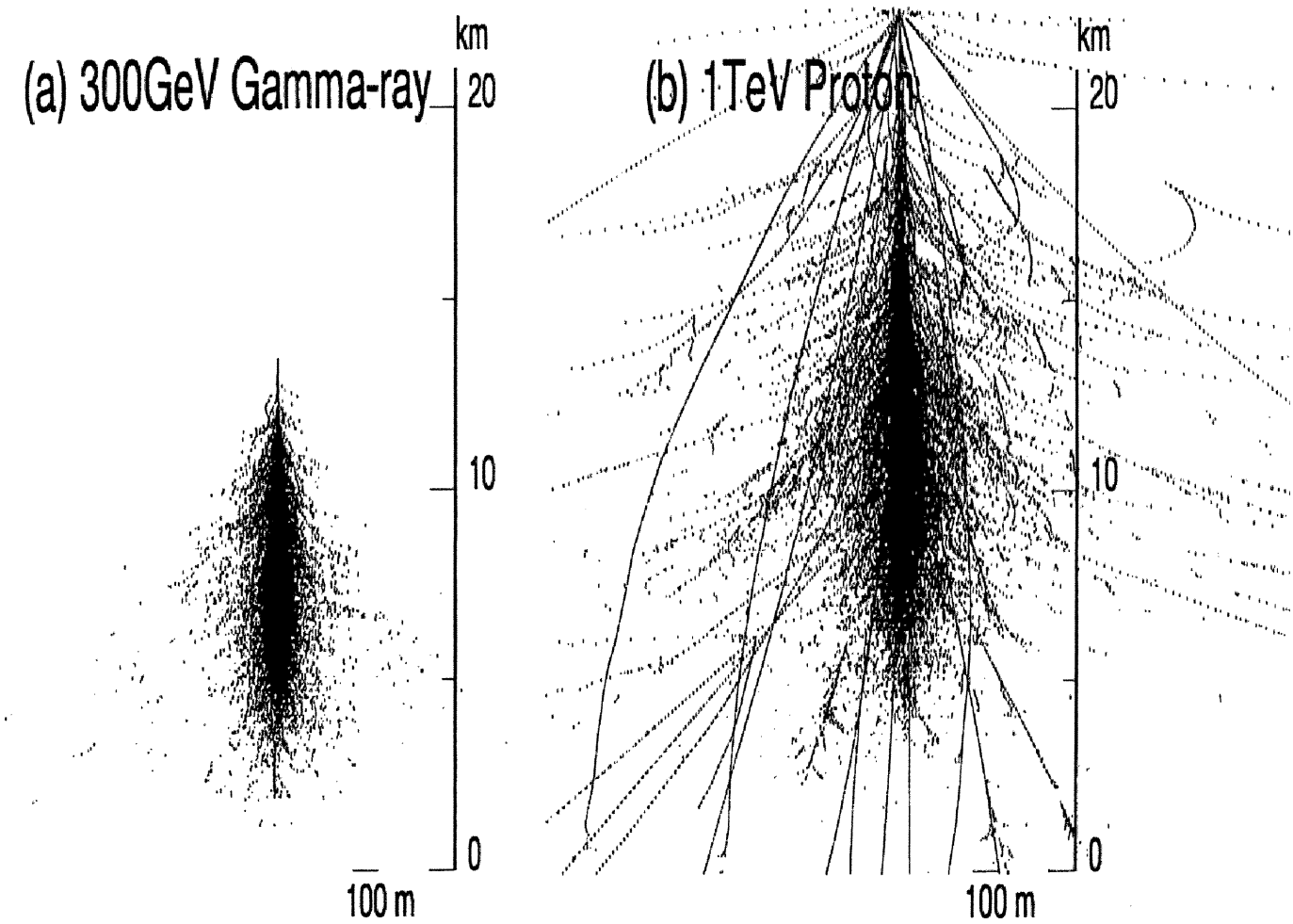

Figure 2.2: Monte Carlo images of the developments of a gamma-ray shower (a) and a proton shower (b). Only trajectories of charged particles are presented.

light velocity, c, in vacuum. The number of photons (dN) emitted in a unit wavelength ($d\lambda$) per unit length along the path (dx) of the relativistic charged particle is represented as,

$$\frac{dN}{d\lambda dx} = 2\pi\alpha\left(1 - \frac{1}{n^2\beta^2}\right)\frac{1}{\lambda^2} \quad . \tag{2.2}$$

Here, $\alpha \equiv \epsilon^2/\hbar c = 1/137$ is the fine structure constant and λ, the wavelength of a Čerenkov photon. The main process to scatter Čerenkov photons in the atmosphere is Rayleigh scattering. The cross section (σ) of Rayleigh scattering has a strong wavelength dependence as $\sigma \propto \lambda^{-4}$. Although the emissivity of photons at shorter wavelength is high, the attenuation in the atmosphere is also severe. After all these considerations are taken into account, the spectrum of Čerenkov photons observed at the ground has a peak around λ=300 nm. So Čerenkov telescopes are optimized to detect photons in these wavelengths.

The distributions of Čerenkov photons on the ground were simulated using Monte Carlo calculations and shown in Figure 2.3 for a gamma-ray and a proton primary EAS. These results show the characteristics of the shower developments very well. A gamma-ray initiated shower makes a uniform distribution of Čerenkov photons, while a proton initiated shower makes an irregular distribution. The lateral extension of Čerenkov photons of a gamma-ray shower reaches $\sim$ 150 m, which results a very large effective area of $\sim 7 \times 10^4$ m^2. Comparing with the area of a typical satellite detector of 1 m^2, we can immediately recognize the great viability of the EAS experiments with effective areas as large as 7×10^4 m^2 in observing the rare VHE gamma-rays. Since Čerenkov photons emitted from an EAS arrive straight at the ground, the angular distribution of photons should represent the *image* of the shower. Developments of the technique to resolve the *images* of EASs have raised VHE gamma-ray astronomy to the present status.

2.3 Imaging Air Čerenkov Telescopes (IACT)

In the observations of VHE gamma-rays, a discrimination of gamma-ray signals from the enormous number of background hadron events is the most important problem. Searches for VHE gamma-ray sources in the early days were carried out, based on finding a difference of the

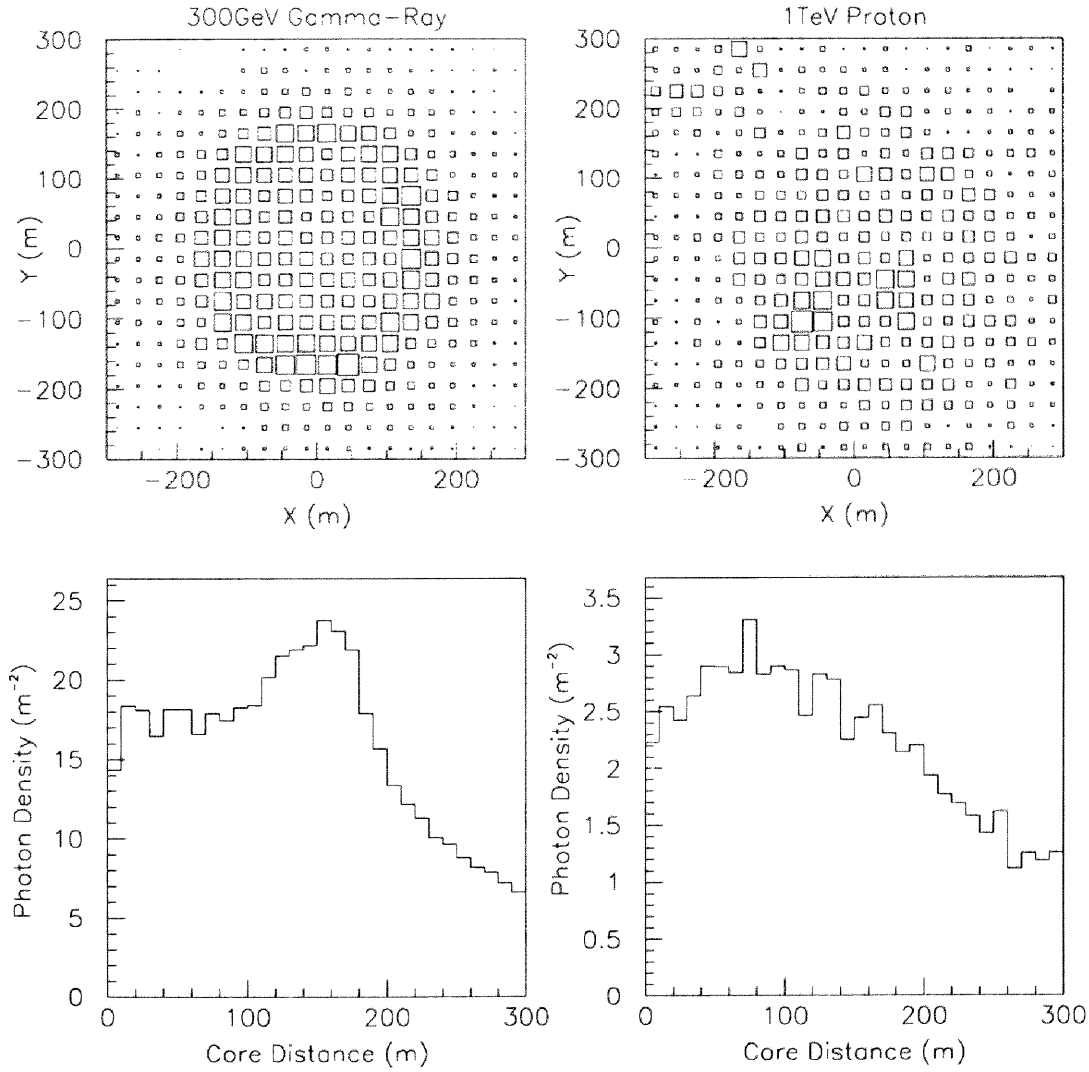

Figure 2.3: Lateral distributions of Čerenkov photons at the ground level. Left figures show the distribution of a gamma-ray initiated shower and right figures show that of a proton initiated shower.

counts of the EASs between the directions of the candidate (ON source) and a control region (OFF source). However, a much more powerful technique to reject the background is needed for more sensitive gamma-ray observations. As mentioned in the previous section, the difference in the characteristics of the developments of EASs can be used to identify the primary particle. Such a powerful method, the *imaging technique*, was proposed by Hill and Porter [24] and first realized by Weekes [79]. The images of EASs are obtained by detecting Čerenkov photons using a reflecting mirror as illustrated in Figure 2.4. As an imaging device to be mounted at the focal plane, an array of small size photomultiplier tubes (PMTs) is used. Detectors using such a technique are called *Imaging Air Čerenkov Telescopes (IACT)*. Typical images of a gamma-ray and a proton initiated showers at the focal plane obtained by Monte Carlo calculations are shown in Figure 2.5. The intensities of Čerenkov photons in each PMT are electronically recorded. The technique to parameterize images and to distinguish gamma-ray initiated showers from hadron initiated showers is described in the following section. Several IACTs are in operation in the world [81] as well as many others under construction, funded and proposed.

2.4 Imaging Technique

A Čerenkov image of an EAS is regarded as an ellipse and characterized by some parameters. In Figure 2.6, the conventional *shape parameters* and *orientation parameters* introduced by Hillas [25] are represented. Distributions of these *image parameters* calculated using Monte Carlo method for both a gamma-ray and a proton primary showers are shown in Figure 2.7. The *asymmetry* parameter is newly introduced by Punch [48], which represents the asymmetry of the intensity of Čerenkov photons along the image axis. A positive *asymmetry* value is expected for an EAS developed towards the outgoing direction with respect to the origin, which is the case of gamma-ray shower if the source is located at the origin. In case of isotropic hadron background, the *asymmetry* parameter distributes evenly in positive and negative values. The clearest difference between the parameter distributions of gamma-ray and proton is found in the *alpha* parameter. In the procedure to discover gamma-ray signals amidst a dominant background

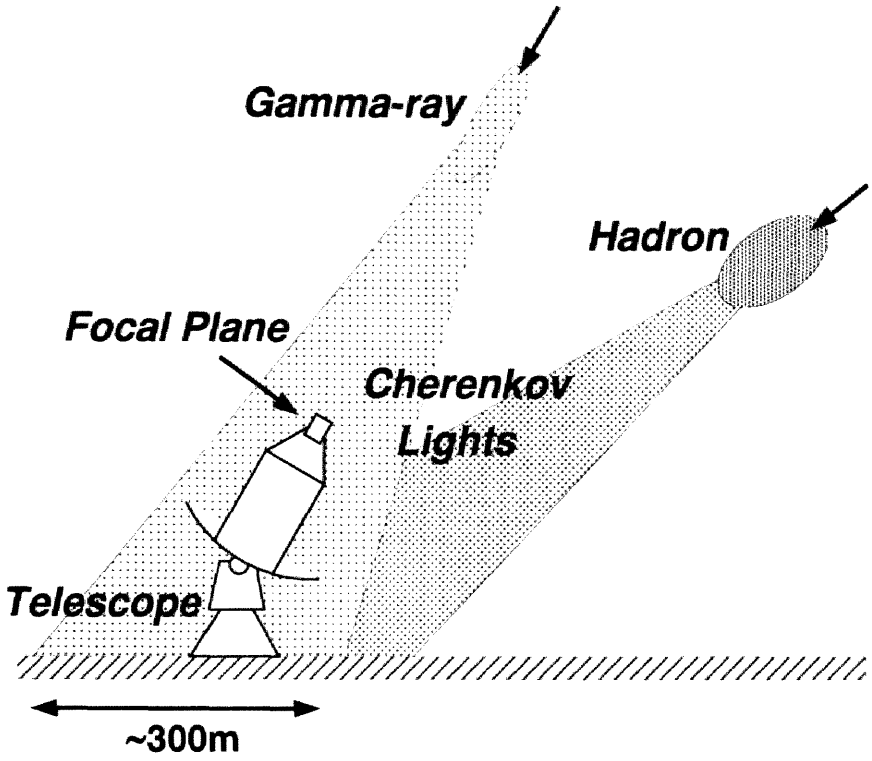

Figure 2.4: Schematic view of the VHE gamma-ray observation.

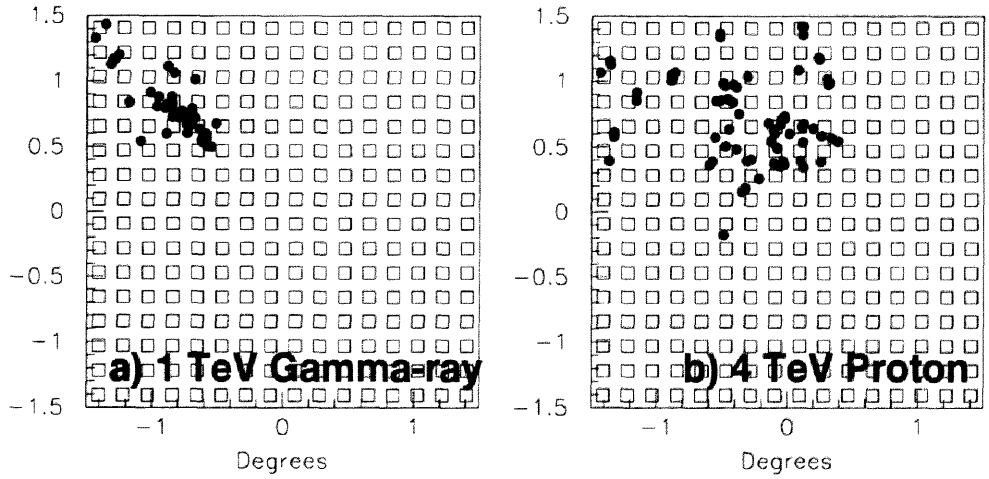

Figure 2.5: Typical Čerenkov images of a gamma-ray (a) and proton (b) initiated shower at the focal plane. Each dot represents a Čerenkov photon. Small squares show the array of PMTs in case of the *CANGAROO* 3.8m telescope.

(proton signals) sea, the parameter cuts are applied to reject background and enhance gamma-ray signals. Criteria for the cuts depend on each detector and on the observational conditions (for example, zenith angle, night sky background and so on) so that they are optimized for the individual case. Usually, after all the cuts except *alpha* and *asymmetry* are applied, the distributions of the *alpha* and *asymmetry* parameters are examined. If a gamma-ray source is located at the origin, which can be arbitrarily defined in the calculation of parameters, the *alpha* distribution of events has an excess at $alpha \sim 0°$ and the *asymmetry* parameter has an excess in the positive value. The VHE gamma-ray sources detected by the various IACTs are already shown in Figure 1.1.

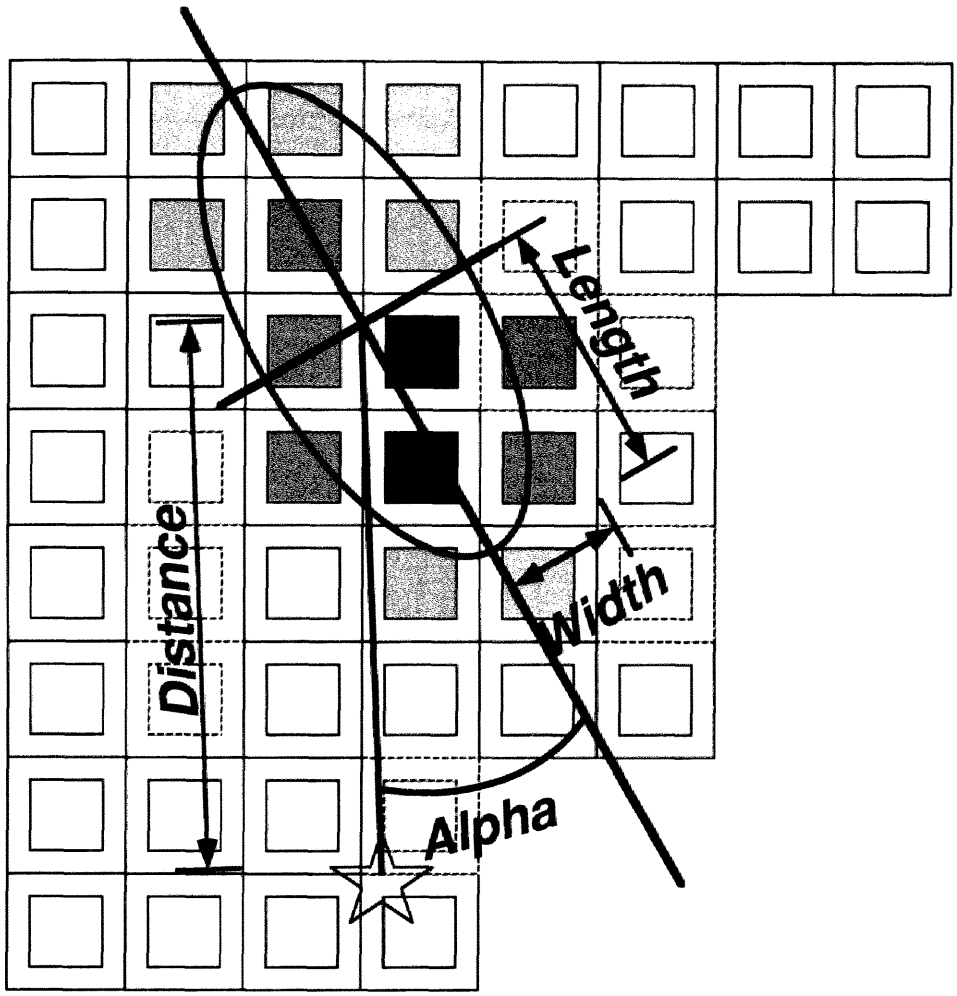

$$\textbf{Concentration} = \frac{\textbf{ADC}_{max} + \textbf{ADC}_{2nd}}{\textbf{sum ADC}}$$

Photomultiplier receiving Cerenkov light

Assumed Source Position

Figure 2.6: Definitions of the *image parameters*

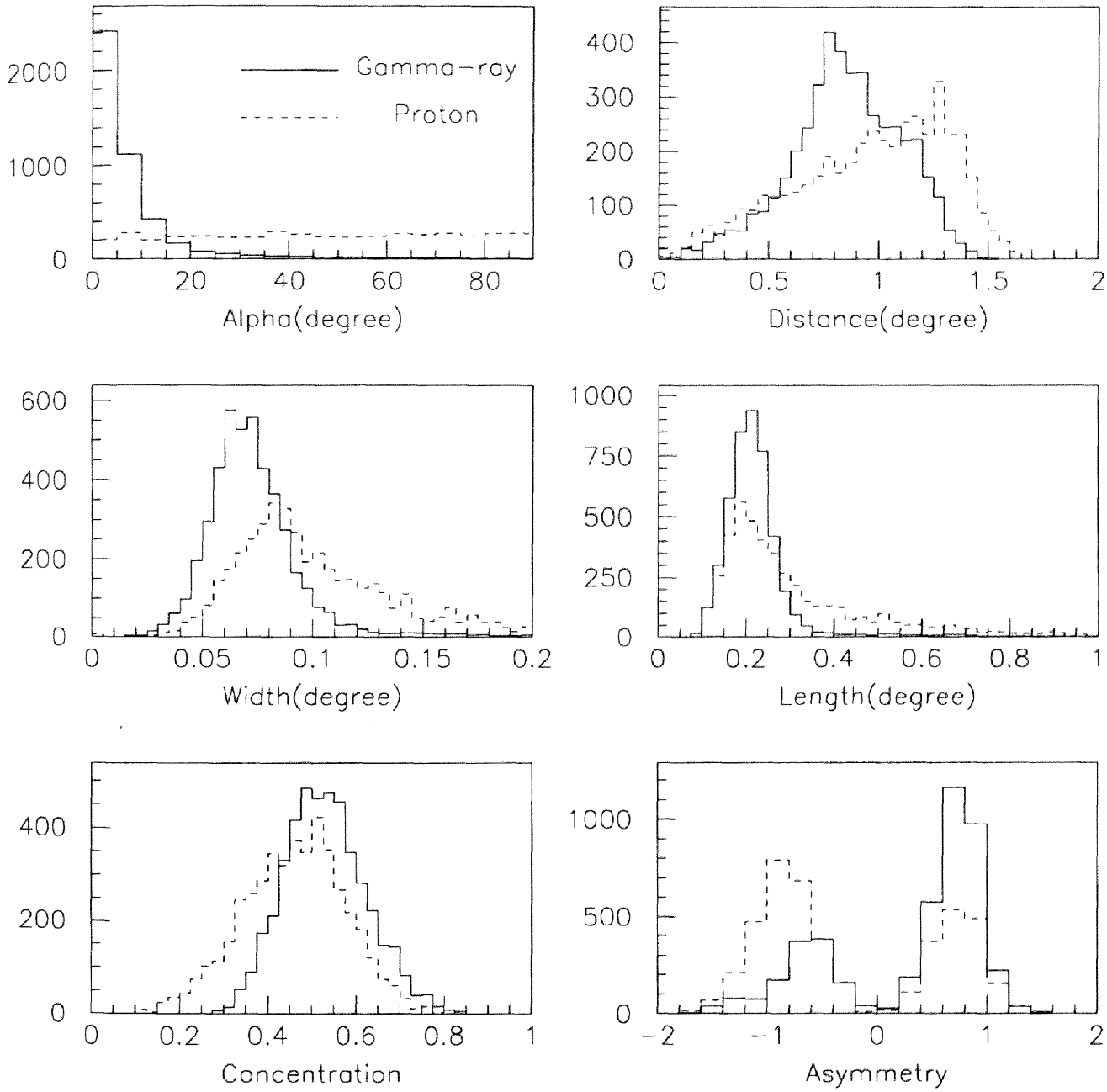

Figure 2.7: Distributions of the *image parameters* (Monte Carlo calculations). Solid lines show the distributions of gamma-ray initiated showers. Dashed lines show those of proton initiated showers.

Chapter 3

High Energy Phenomena around Pulsars

Pulsars and their surrounding nebulae are some of the most plausible acceleration sites of cosmic rays. High-energy phenomena occurring in the near and far regions from a pulsar are described separately in the following sections. The approximate boundary between these two regions is the radius of light cylinder, where the co-rotational speed of the pulsar magnetosphere equals the speed of light. High-energy particles are produced in both the regions through different processes of acceleration. In successive interactions between particles and fields, gamma-rays are expected to be produced and emitted from environments around pulsars.

3.1 Pulsar Kinematics

Pulsars are considered as magnetized rotating neutron stars left after supernova explosions. They are identified by periodic radiations modulated at the rotational period of the pulsars. A pulsar gradually loses its rotational energy and the rotation speed decreases. It results in the observable properties, the period derivatives $\dot{P}$ ($\ddot{P}$ also) as well as the period P. Combining these two observables and basic formulae, some important parameters of a pulsar can be estimated. The characteristic age, τ, is defined as $\tau = P/2\dot{P}$. This gives an approximate time since the birth of the pulsar until now.

The energy loss rate, $\dot{E}_{rot}$, is derived from,

$$-\dot{E}_{rot} = -\frac{d}{dt}\left(\frac{1}{2}I\Omega^2\right) = (2\pi)^2 I\frac{\dot{P}}{P^3} . \tag{3.1}$$

Ω $(= 2\pi/P)$ is the angular velocity of the pulsar. I is the moment of inertia of the pulsar, which is typically $I \sim 10^{45}\mathrm{g\,cm^2}$ and the variation of the I value among pulsars is expected to be small. Adopting the values of the Crab pulsar, *i.e.*, $P = 33$ ms and $\dot{P} = 421 \times 10^{-15}$ $\mathrm{ss^{-1}}$, one can obtain $\dot{E}_{rot} = 4.6 \times 10^{38}$ ergs $\mathrm{s^{-1}}$. If this energy is emitted isotropicaly, the expected energy flux at the Earth becomes $\dot{E}/4\pi R^2 = 9.6 \times 10^{-7}$ ergs $\mathrm{cm^{-2}\ s^{-1}}$, which is the largest value among the known pulsars. (R is the distance from the pulsar to the Earth. In the case of the Crab pulsar, $R = 2.0$ kpc)

An estimation of the surface magnetic field of the pulsar, B_s, is given by Ostriker and Gunn [46] as,

$$B_s \simeq \sqrt{\frac{3c^3P^4\dot{E}}{32\pi^4a^6}} . \tag{3.2}$$

Here, a is the radius of the pulsar itself and is thought to have a value, $a \simeq 10^6$ cm. From Equations(3.1) and (3.2),

$$B_s \simeq 1.0 \times 10^{12}\left(\frac{P}{1\,\mathrm{sec}}\right)^{\frac{1}{2}}\left(\frac{\dot{P}}{10^{-15}\,\mathrm{ss^{-1}}}\right)^{\frac{1}{2}}\ Gauss \tag{3.3}$$

is resulted.

Properties of some of the pulsars are listed in Table 3.1. The pulsars are ranked according 10 the value of the energy flux ($\dot{E}/4\pi R^2$) introduced above.

3.2 Pulsar Magnetosphere

Magnetic field lines around a pulsar are co-rotating at an angular velocity, $\Omega(= 2\pi/P)$, of the pulsar rotation. The distance R_L from the rotation axis of the pulsar is defined as $R_L\Omega = c$, where the co-rotational speed equals the speed of light. This boundary, namely the *light cylinder*, characterizes the inner region as the *pulsar magnetosphere*. The schematic view of a pulsar magnetosphere is represented in Figure 3.1.

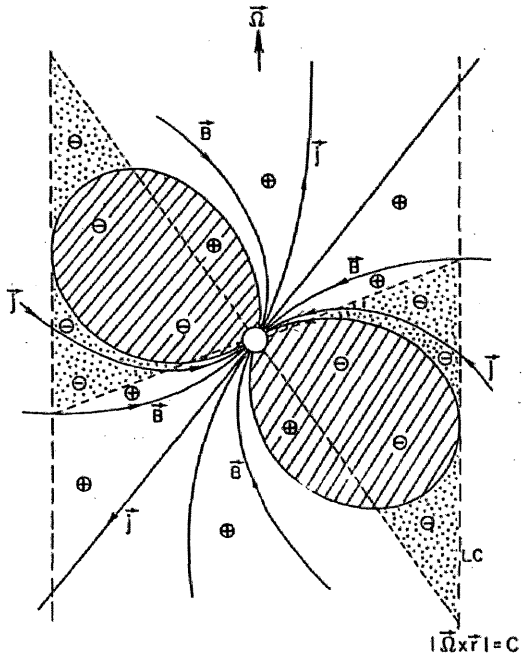

Figure 3.1: Schematic view of a pulsar magnetosphere. Two inclined dashed lines show the null surfaces, where the Goldreich-Julian density of charged particles becomes zero. [10]

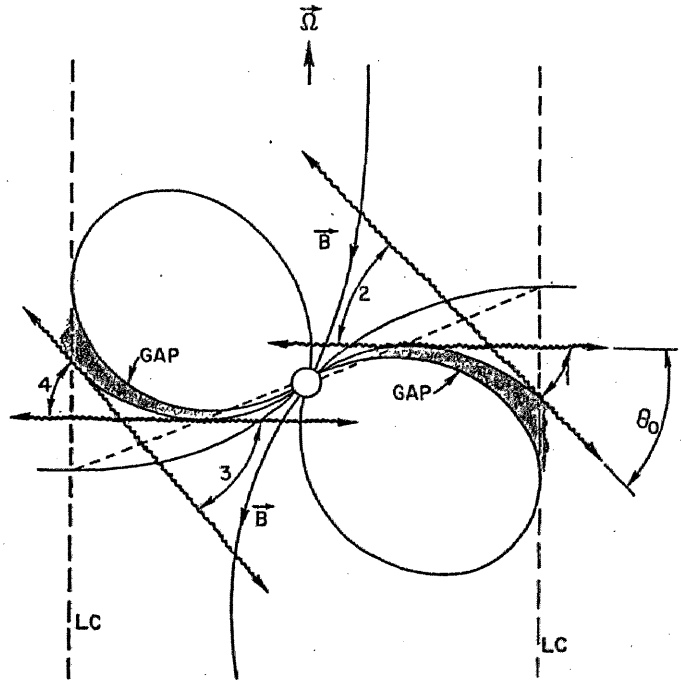

Figure 3.2: Locations of the outer gaps in a pulsar magnetosphere. [10]

Table 3.1: Properties for various pulsars. They are ranked according to $\frac{\dot{E}}{d^2}$. Entries in the columns X_{neb}, EG and VHE signify if the object is detected as a synchrotron X-ray nebula, by the *EGRET* and in VHE gamma-rays, respectively.

Pulsar Name	Period (msec)	log(Age) log(year)	$\log(\dot{E})$ $\log(\text{erg s}^{-1})$	d (kpc)	$\log(\frac{\dot{E}}{d^2})$ $\log(\text{erg cm}^{-2}\text{ s}^{-1})$	X_{neb}	EG	VHE
B0531+21 (Crab)	33	3.10	38.6	2.0	-6.03	√	√	√
B0833-45 (Vela)	89	4.05	36.8	0.50	-6.64	√	√	√
J0633+17 (Geminga)	237	5.53	34.5	0.15	-6.76	√	√	
B1706-44	102	4.24	36.5	1.8	-8.06	√	√	√
B1509-58	150	3.19	37.2	4.4	-8.11	√		?
J0437-47	5.8	9.20	34.1	0.14	-8.30			
B1951+32	40	5.03	36.6	2.5	-8.30	√	√	
B1046-58	124	4.31	36.3	3.0	-8.72	√		
B1823-13	102	4.33	36.5	4.1	-8.86			
B1800-21	134	4.20	36.3	3.9	-8.92			

The pulsar magnetosphere is filled by charged particles with the Goldreich-Julian density [16],

$$\rho = \frac{\nabla \cdot \boldsymbol{E}}{4\pi} = -\frac{\boldsymbol{\Omega} \cdot \boldsymbol{B}}{2\pi c(1 - |\boldsymbol{\Omega} \times \boldsymbol{r}/c|^2)} . \tag{3.4}$$

If all the pulsar magnetosphere is completely sustained by charged particles, any component of electrostatic field parallel to the magnetic field immediately vanishes due to the flow of the charges. In such a condition ($\boldsymbol{E} \cdot \boldsymbol{B} = 0$) particle acceleration along the magnetic field lines cannot be expected. However, the existence of a *gap*, where stable depletion of charges occurs, are predicted in two ways, *i.e.*, the *polar cap* [55] and the *outer gap* [10]. In these gaps, along the electrostatic field which satisfies the condition, $\boldsymbol{E} \cdot \boldsymbol{B} \neq 0$, charged particles are accelerated.

3.2.1 Polar Cap Model

Magnetic field lines, which intersect the light cylinder, do not form closed loops, so they are called *open field lines*. These lines originate in the polar regions of the pulsar surface (the *polar caps*). On the other hand, magnetic field lines that originate in the low latitude regions of the

pulsar surface are named *closed field lines*. This situation is shown in Figure 3.1. Since charged particles are moving along the magnetic field lines, charges on the open field lines are outgoing through the light cylinder. If there is no or insufficient supply of charges, a charge depletion occurs along the open field lines. Ruderman and Sutherland [55] have shown that a gap appears near the pulsar surface, so their acceleration model is called the *polar cap (gap)* model. With the outflow of the charges through the light cylinder, the size of the gap eventually grows. However, because the accelerated particles in the gap produce cascade showers, *i.e.*, curvature radiations of gamma-rays by electrons and positrons and pair creations of electrons and positrons by gamma-rays, the depletion of the charge can be resolved. Ruderman and Sutherland [55] have concluded that a balance between the growth of the gap and the cascade is achieved when the altitude of the gap from the pulsar surface, h, becomes $h \simeq 10^4$ cm. The maximum potential difference in this gap is estimated to be $\simeq 10^{12}$ V.

3.2.2 Outer Gap Model

From the Equation (3.4), we can deduce a charge depletion, $\rho = 0$, on the surfaces where $\boldsymbol{\Omega} \cdot \boldsymbol{B} = 0$. The locations of such surfaces are shown in Figure 3.1. Around these surfaces, it is possible that electrostatic fields satisfying $\boldsymbol{E} \cdot \boldsymbol{B} \neq 0$ are realized. Analogous with the case of the *polar cap* model, particles accelerated along the electrostatic fields, $\boldsymbol{E}$, produce successive electromagnetic cascades and only limited regions can be left to be *gaps*. Cheng, Ho and Ruderman [10] have studied these processes and obtained the places of the gaps. The resultant places of the gaps are also indicated in Figure 3.2. Because the gap is located relatively farther from the pulsar than the *polar cap*, it is named the *outer gap*. In the case of the *polar cap* model, the strong magnetic field near the pulsar surface attenuates the escape of the produced gamma-rays by pair production. However, in the *outer gap* region, the magnetic field strength, which decreases as $\propto r^{-3}$, is relatively weak as a result of which severe attenuation of gamma-rays is avoided.

The two models introduced above are used to explain the pulsed component of gamma-rays detected by the *EGRET* [13]. However, to investigate models of VHE gamma-ray productions, interactions beyond the light cylinder must be considered.

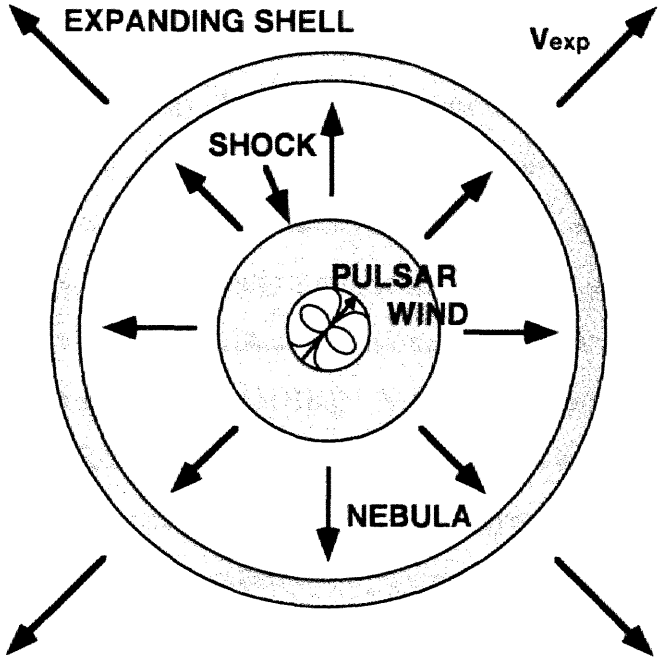

Figure 3.3: Schematic view of a pulsar nebula, according to Harding [19].

3.3 Pulsar Nebulae

Relativistic charged particles passing through the light cylinder flow away from the pulsar magnetosphere. This flow of the charged particles is called the *pulsar wind.* The energy density in the pulsar wind, far from the pulsar magnetosphere, is dominated by that of the particles. In the case of the Crab pulsar/nebula, the ratio (σ) of the magnetic field to the particle energy density in the wind is estimated to be $\sigma \simeq 0.003$. This particle dominant wind terminates when the wind collides with the supernova ejecta, which is expanding with a speed of $v_{exp} \ll c$. In the downstream of this shock surface, the motion of the particles are randomized and the energy densities of the particles and the magnetic field become equipartition. The situation described above is schematically represented in Figure 3.3 (Harding [19]). In the shock region, a first order Fermi acceleration process is expected to occur. The existence of such a non-thermal process is confirmed by the synchrotron emissions observed in the radio to X-ray wavelengths from the extended region around the pulsar, namely the *pulsar nebula* [32]. The basic ideas of the pulsar nebula about the Crab were studied by Rees and Gunn [53].

As mentioned above, a pulsar nebula is found in the radio to X-ray (in some cases gamma-ray) wavelengths through synchrotron radiation from relativistic electrons or positrons. The

existence of relativistic electrons (hereafter it means both electrons and positrons) means a possibility of a VHE gamma-ray emission through inverse Compton scattering of electrons in a photon field. In order to emit a detectable flux of VHE gamma-rays, certain amount of soft energy photons (besides the relativistic particles) must exist as a target for inverse Compton process to take place. The undoubtedly existing candidate for this soft photon is the 2.7 K microwave background radiation (MBR) . Actually, as shown in Section 3.4.4, the energy density of the 2.7 K MBR is sometimes sufficient to result in detectable flux of VHE gamma-rays. Another candidate for the soft photon field is synchrotron emission by the relativistic electrons themselves. This model, called the *Synchrotron Self Compton* (SSC) model, is applied to the emission from the Crab nebula and explains well its spectrum all the way from the radio to VHE gamma-ray wavelengths (about 18 orders of magnitude !!) [33] [30].

Here I consider some important relationships among the relativistic electrons, inverse Compton photons, synchrotron photons and soft photons. If a relativistic electron having a Lorentz factor γ emits a synchrotron photon in the magnetic field B, the characteristic energy of the photon, ϵ_{sync}, is given by,

$$\epsilon_{sync} = 5 \times 10^5 \left(\frac{B_\perp}{1\mu\mathrm{G}}\right)\left(\frac{\gamma}{10^{10}}\right)^2 \ eV \ . \tag{3.5}$$

Here $B_\perp$ is the perpendicular component of the magnetic field with respect to the momentum vector of the electron. The same electron also imports its energy to a soft photon with an energy ϵ_{soft} and boosts the photon energy up to ϵ_{iC} through inverse Compton scattering. The possible maximum value of ϵ_{iC}, ϵ_{iC}^{max}, is realized when the electron and the soft photon collide head-on. If we define the characteristic energy of the scattered photon, ϵ_{iC}, to be $\epsilon_{iC}^{max}/4$, that is expressed as,

$$\epsilon_{iC} \equiv \frac{\epsilon_{iC}^{max}}{4} = \frac{\gamma^2}{1 + 4\epsilon_{soft}\gamma}\,\epsilon_{soft} \ . \tag{3.6}$$

Using two Equations (3.5) and (3.6), and the observed synchrotron spectrum, we can estimate the flux of inverse Compton photons, which are found in the VHE region. In the process of these calculations, the nature of the soft photon field and the magnetic field strength are free

parameters. It means that with a proper assumption about the soft photon, a VHE gamma-ray observation gives us a good estimation of the magnetic field strength in the nebula.

Finally in this section, we can find a simple method to estimate the magnetic field strength without any detailed calculation of the spectrum as described above. From basic arguments of the emission processes of synchrotron radiation and inverse Compton scattering, emission powers, P_{sync} and P_{iC}, are described,

$$P_{sync} = \frac{4}{3}\sigma_T c\gamma^2\beta^2 U_B \tag{3.7}$$

and

$$P_{iC} = \frac{4}{3}\sigma_T c\gamma^2\beta^2 U_{soft} \, . \tag{3.8}$$

Here σ_T is the Thomson cross section, $\sigma_T = 6.7 \times 10^{-25}$ cm^2, and β is the speed of the electron in the units of c. U_B and U_{soft} are the energy densities of the magnetic field and the soft photons, respectively. Combining these equations, we can obtain an important equation,

$$\eta = \frac{P_{iC}}{P_{sync}} = \frac{U_{soft}}{U_B} \, . \tag{3.9}$$

3.4 PSR B1509-58 and Supernova Remnant MSH15-52

3.4.1 Overview

Pulsed emissions from PSR B1509-58 have been detected in radio, X-ray, soft gamma-ray and TeV gamma-ray (transient). Unpulsed emissions from MSH15-52, including the pulsar nebula, are seen in the radio to hard X-ray wavelengths. Neither the pulsed nor the unpulsed emission is detected by the *EGRET* detector [70], although low value unpulsed emissions are reported by Brazier *et al.* [5] and Fierro [13] at significant levels of 2.7 σ and 3.9 σ, respectively.

3.4.2 Age Discrepancy between the Pulsar and the SNR

PSR B1509-58 was discovered as an X-ray pulsar in the year 1982 by Seward and Harnden [57] using the *Einstein* observatory near the center of the supernova remnant MSH15-52. Soon

after this discovery, the pulsation at radio wavelength was found by Manchester, Tuohy and D'Amico [39]. From the observed pulsar period and the first derivative, $P = 150$ ms and $\dot{P} = 1.5 \times 10^{-12}$ ss^{-1}, it is concluded that the characteristic age of this pulsar, $\tau \simeq 1600$ years. This makes it the second youngest among the known pulsars. However, there has appeared a discrepancy between the ages of the pulsar and its embedding supernova remnant because the age of MSH15-52 was estimated to be $\simeq 10^4$ years [11]. Some explanations are offered to solve this discrepancy. Three natural arguments are introduced below (see [58] for the first two and [4] for the last one).

First, an overestimation of the SNR age. Assuming that the supernova explosion was unusually energetic, $E_0 = 10^{52}$ ergs, and occurred in the space with a low density of the interstellar matter (ISM), $n \simeq 0.1$ cm^{-3}, Seward *et al.* [58] obtained the age of the SNR to be $\simeq 2100$ years, which agrees with the pulsar age. They discussed, furthermore, the difficulty of the rather large E_0 and proposed a lower $n \simeq 0.01$ cm^{-3} with a normal $E_0 = 10^{51}$ ergs. However, this pulsar and SNR system are located in the Galactic plane, where n may even exceed 1 cm^{-3}, so that an additional assumption is required to achieve the environment with a very low density. The hypotheses given by Seward *et al.* [58] are, an *interstellar tunnel* arising from a previous supernova explosion and a *bubble* formed by a strong wind of the precursor star.

Second, a possibility that both the pulsar and the SNR are old was discussed. In this case, we must doubt the characteristic age of the pulsar. The validity of the characteristic age, $\tau = P/2\dot{P}$, is tested only in the case of the Crab pulsar ($\tau \simeq 1300$ years with respect to the actual age of $\simeq 950$ years). But Seward *et al.* [58] themselves prefer the first possibility over the second one. Besides the problem of the characteristic age of the pulsar, they insist that there is a difficulty in explaining the existence of the bright X-ray knots in RCW89 (described in Section 3.4.3) with a small energy supply from the old remnant. Thorsett [74] suggests that an ancient guest star occurred in AD185 recorded in China would correspond to the supernova explosion at the birth of PSR B1509-58. If this suggestion is true, the characteristic age of the pulsar will be strongly confirmed.

A third possibility pointed out by Bergh and Kamper [4] is a chance superposition of the pulsar and the SNR on the same line of sight. They have observed the speed of the expansion of the SNR and concluded that the young SNR ages are excluded for both free and Sedov expansion models. After this conclusion, they have calculated the chance probabilities of the superposition of a pulsar and an SNR. Using the accumulated area of the SNRs (61 deg^2, it covers 1.7% of the area concerned here) and the number of the radio pulsars (31 for $P < 1/3$ s and 12 for $P < 1/5$ s) at the Galactic latitude $|b| < 5°$, the chance probabilities were obtained to be 0.53 and 0.20 for the two limits of P. These results mean that the relation between the pulsar and the SNR can be only a chance superposition on the same line of sight. However, concerning the fact that the pulsar is located at the center of the remnant, these probabilities may be reduced to smaller values. Furthermore, a recent X-ray observation indicates a connection between the pulsar nebula and a part of the SNR, RCW89 [65].

This unsolved age problem is also discussed in the following sections.

3.4.3 Morphology

The radio contour map of the supernova remnant MSH15-52 (G320.4-1.2) is shown in Figure 3.4 [43]. The brightest region enclosed by a rectangle in Figure 3.4 has an extension with a diameter of $\simeq 30'$. Two bright arcs, noted the NW and SE arcs, are regarded as parts of the shell of the SNR. In the radio observations, MSH15-52 is classified as a *shell type* supernova remnant. The location of the pulsar PSR B1509-58, indicated in Figure 3.4, is nearly at the center of the arc structure. It supports the true association of the pulsar and the SNR. However, no strong compact source is found at the pulsar position. The strongest emission in the NW arc coincides with the H_α nebula RCW89.

In contrast to the radio feature, a bright X-ray source is found at the pulsar position. Two X-ray nebulae were known since the observation of the *Einstein* satellite [58]. Recent result of the *ROSAT* is shown in Figure 3.5 [76]. Two compact nebulae, the North Nebula (NN) and the South Nebula (SN), are coincident with RCW89 and PSR B1509-58, respectively. The NN is known to have a thermal X-ray spectrum while the emission from the SN is well fitted by a non-thermal spectrum. The emission of the SN in Figure 3.5 looks like having an elongated

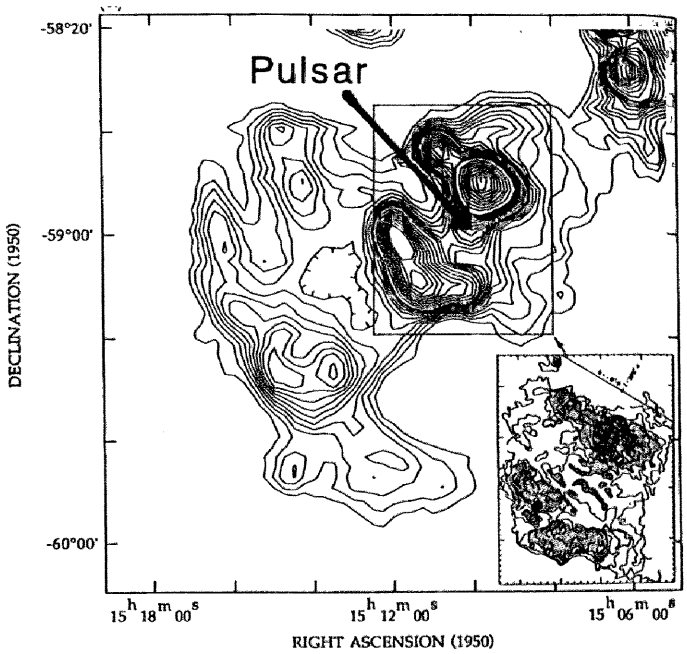

Figure 3.4: Radio contour map of the SNR MSH15-52. The position of the pulsar is indicated by an arrow. Two bright structures, the NW and SW arcs, are clearly seen. [41]

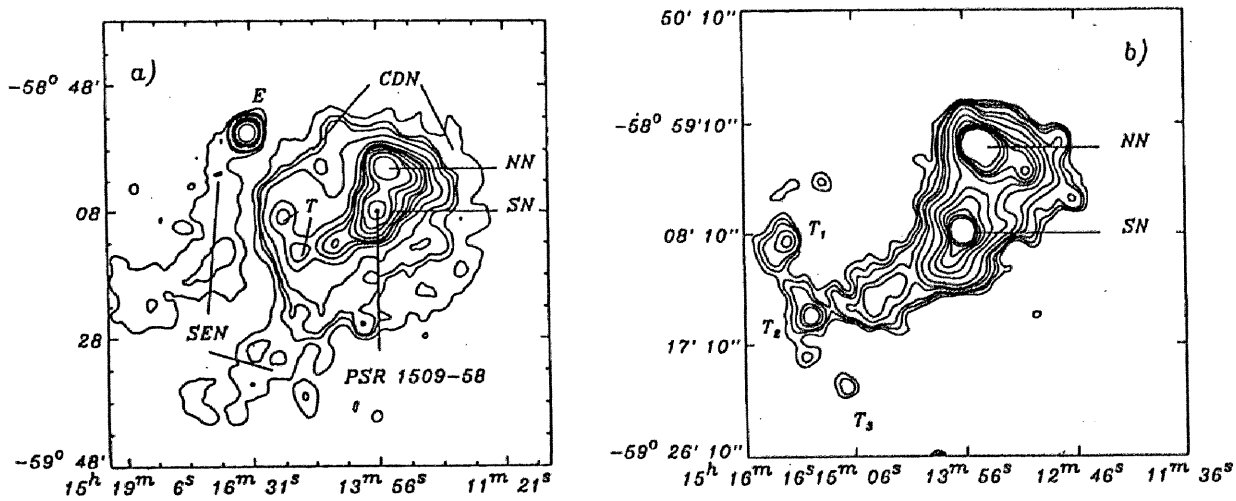

Figure 3.5: X-ray contour maps obtained by the *ROSAT* satellite [72]. Figure (a) shows the whole SNR. Figure (b) shows the brightest two nebulae. One is the non-thermal South Nebula around the pulsar and the other is the thermal North Nebula coincident with the optical filament RCW89.

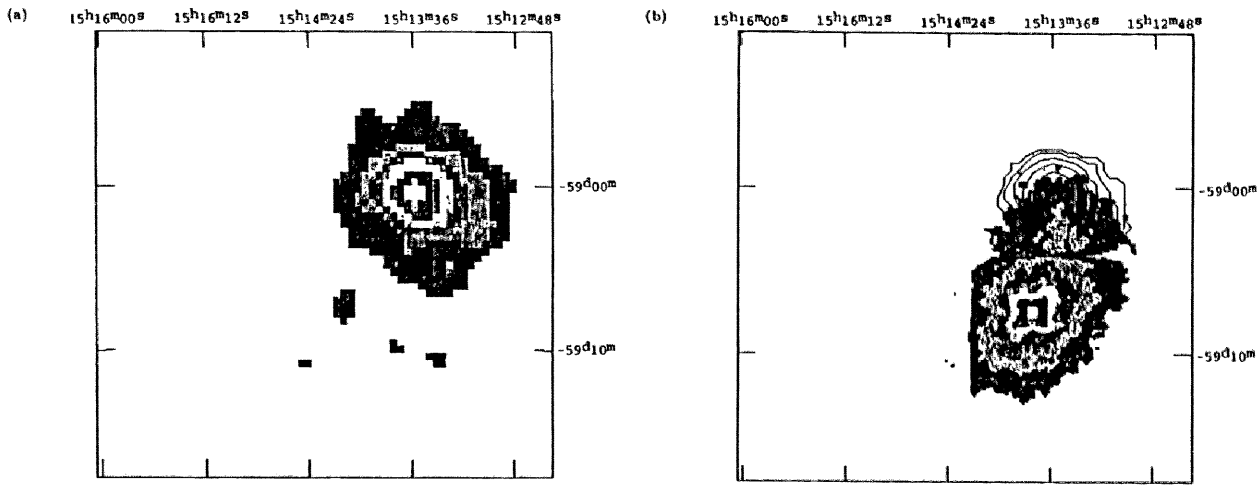

Figure 3.6: The *ASCA* observation of MSH15-52 [65]. Figure (a) is constructed only using thermal photons (Mg K_α line). On the other hand, figure (b) represents the image made by non-thermal photons (> 2.2keV). In figure (b), a non-thermal jet from the pulsar to the center of the thermal nebula is clearly seen.

structure in the north and south derections. Same structure is also resolved by the *ASCA* satellite [65]. In this observation, Tamura *et al.* [65] have reported a striking result. The image reconstructed from only the non-thermal photons (> 2.2 keV) is shown in Figure 3.6. The jet elongating to the north direction terminates at the center of the NN. Tamura *et al.* [65] estimate the energy supplied from the pulsar through the jet is enough to thermalize the NN to the present luminosity. This fact becomes a strong proof of the association of the pulsar with the SNR. At the same time, they pointed out that pure electron flow could not be stopped efficiently by the plasma in the NN and hadronic flow might exist in the jet.

Coming back to Figure 3.5 again, we can find some extended structure, namely the Central Diffuse Nebula (CDN), the Tailed structure (T) and the SE elongated Nebula (SEN), and some associations with the radio structure in Figure 3.4. The extension of the CDN is similar to that of the radio bright region and the tailed structure is located on the SE bright radio shell.

The SEN appears to connect to the weaker extended radio source G320.6-1.6, seen in the left part of Figure 3.4. Trussoni *et al.* [76] suggested the SEN could be a result of the counter jet with respect to the jet flowing to the NN. Such asymmetrical structures caused by two jets can be explained by the difference of the ISM density, *i.e.*, the NN is closer to the galactic plane, where the ISM density is high, while the SEN is extending to the direction with high galactic latitude.

3.4.4 The South Nebula as a Candidate of a VHE Gamma-ray Source

The south nebula (SN) surrounding the pulsar is seen only in the X-ray energy range. Because the spectrum from this nebula is well fitted to power law, the emission is thought to be synchrotron radiation from relativistic electrons accelerated in the shock between the pulsar wind and the supernova ejecta. It implies, then, that the SN can be a good candidate for a VHE gamma-ray source. du Plessis *et al.* [47] have studied the X-ray spectrum obtained by three different experiments in a wide energy range, and predicted spectrum of VHE gamma-ray emission as a function of the magnetic field strength in the nebula (Figure 3.7). They assumed the 2.7K MBR as target photons for inverse Compton radiation. Although the *IRAS* source IRAS 15099-5856 is known to be at the pulsar position [2], association with the pulsar is not clear. Therefore, the contribution of infra-red photons is not taken into account in their calculations. Their predictions are well within or near the sensitivity of the *CANGAROO* telescope. However, the selected range of the parameter B (4μG to 10μG) is very low comparing that in the Crab nebula, $B_{Crab} \simeq 300\mu$G [29]. The validity of this small value of the magnetic field strength is observationally supported. The volume of the SN is estimated to be $> 10^3$ larger than that of the Crab nebula and the energy loss rate, $\dot{E}$, of the pulsar is $\simeq \frac{1}{30}$ of that of the Crab. If the energy released from the pulsar is divided equally into the particles and the magnetic field, we can estimate the equipartition magnetic field strength. The observational results mentioned above deduce the small value of the magnetic field strength from equipartition (Seward *et al.* [59] estimate $B \simeq 7\mu$G).

Another problem is the extremely large difference in the volume of the nebulae between PSR B1509-58 and the Crab nebula in spite of their similar characteristic ages. It can be explained

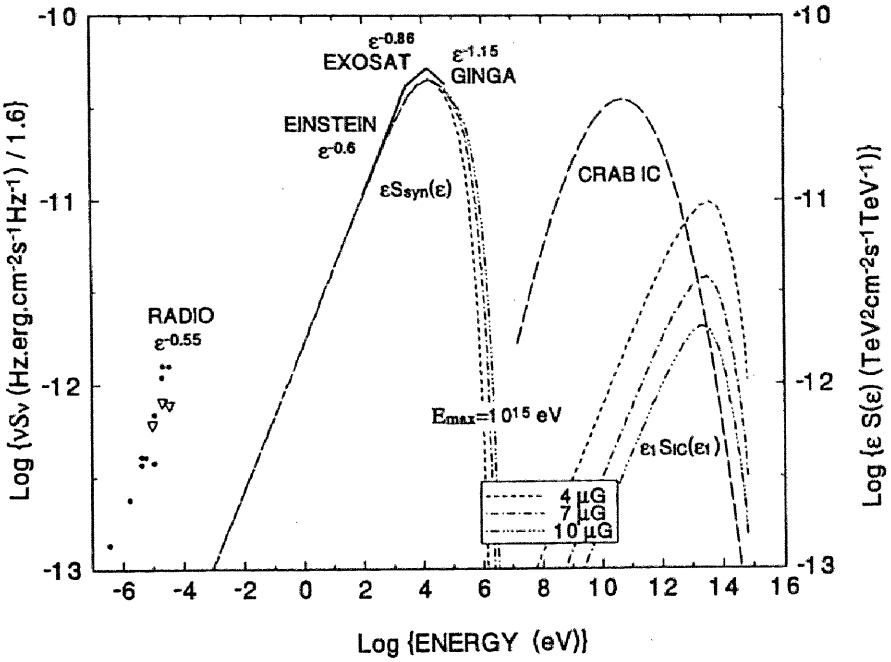

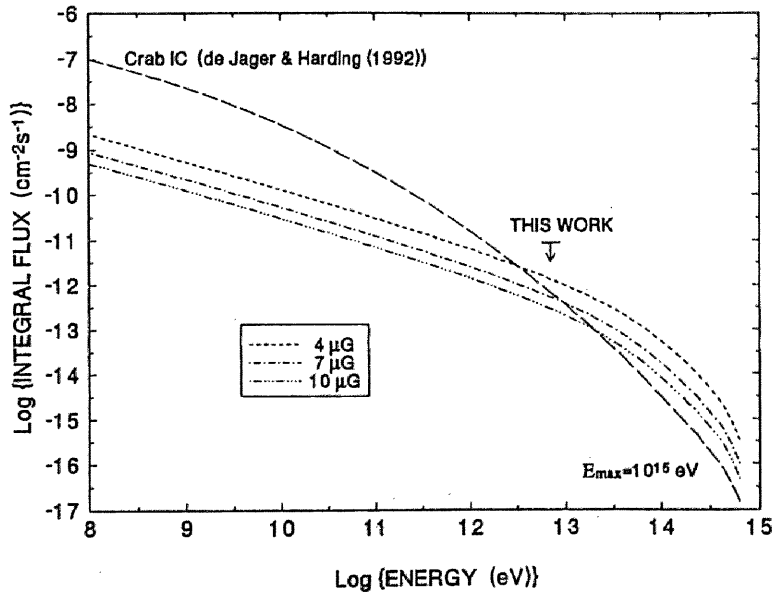

Figure 3.7: VHE gamma-ray fluxes predicted by du Plessis *et al.* [47]. VHE gamma-ray fluxes are represented as a function of the magnetic field strength in the nebula (three dashed lines). In these calculations, 2.7K MBR is assumed as target photons of inverse Compton scattering. 'THIS WORK' means an upper limit obtained by du Plessis *et al.*

by the assumption mentioned in Section 3.4.2. If the supernova remnant has occurred in the ISM with a very low density and the speed of the expansion was extremely high, the resultant size of the nebula becomes large in spite of the young characteristic age of the pulsar. Because the predicted fluxes of VHE gamma-rays depend on the magnetic field strength, a VHE gamma-ray observation can give a good estimation of the magnetic field strength. It is an important parameter in studying the scenarios of the supernovae and the pulsar nebulae.

3.4.5 Pulsed Emission from the Pulsar

The light curves from PSR B1509-58 with a single, broad peak observed over a wide range of wavelengths are shown in Figure 3.8 [77]. As mentioned in Section 3.4.1, the *EGRET* [5] has not detected gamma-ray signal with high statistics in the energy range from 30 MeV to 30 GeV. The upper limit of the flux is an order of magnitude below the extrapolated hard X-ray spectrum recently obtained by Marsden *et al.* [40] using the *RXTE* satellite. This observational break of the spectrum is also reported by Carramiñana and Bennett [8] at about 1 MeV from the *COMPTEL* data. Harding, Baring and Gonthier [20] gave a theoretical explanation of the spectrum break by including $\gamma \rightarrow \gamma\gamma$ attenuation process into the *polar cap* model. This process only takes place in regions where the magnetic field is extremely strong. For the critical magnetic field strength of $B_{cr} = 4.41 \times 10^{13}$ G, if the field concerned satisfies $B \geq 0.3B_{cr}$, the attenuation becomes considerable. Indeed, the surface magnetic field of PSR B1509-58 is estimated to be $B = 1.5 \times 10^{13}$ G $= 0.34B_{cr}$, which is one of the strongest among the known pulsars.

However, although the pulsed emission at energies above MeV is not expected, the detections of the pulsed gamma-rays with energies above about 1.5 TeV are reported by Nel *et al.* [45] using the *Nooitgedacht* telescope. The VHE emissions were detected only in the period between 1985 and 1988, and no emission was seen in the period between 1989 and 1991. In addition to the transient nature with a time scale of a few years, another transient with a time scale of $\simeq 10$ days is reported in the same paper.

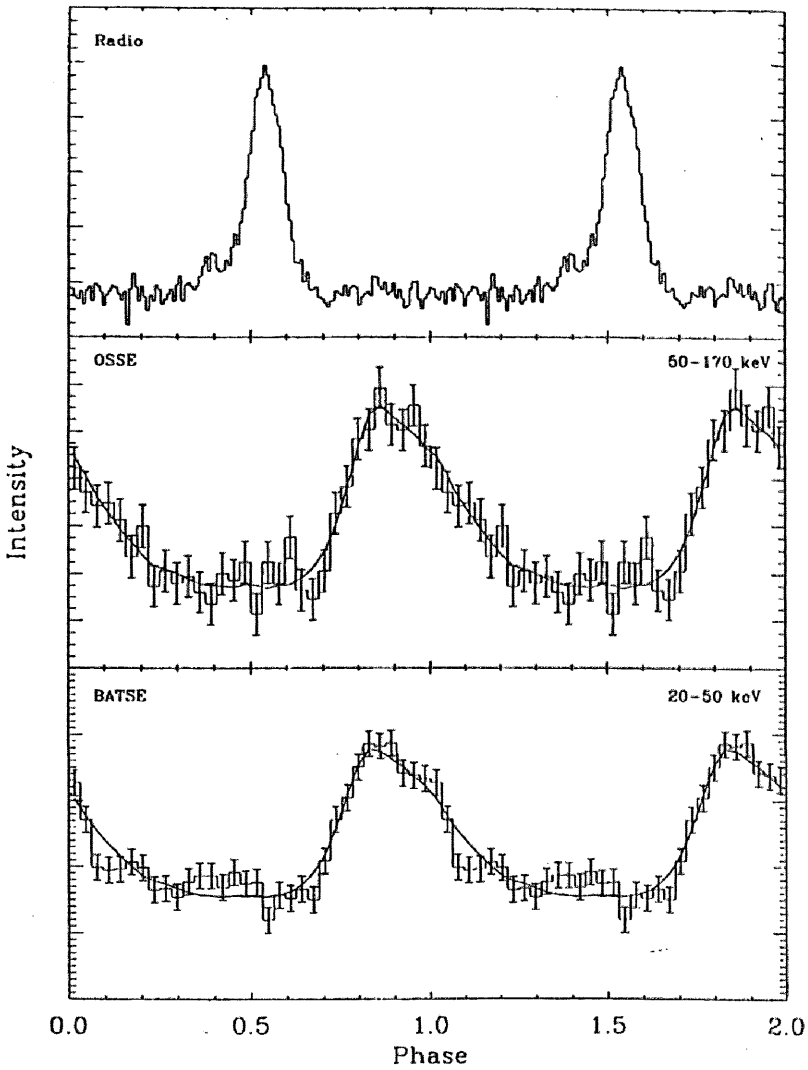

Figure 3.8: Light curves of the pulsed emision from the pulsar PSR B1509-58 in various wavelengths [73].

Chapter 4

The CANGAROO Telescope and Observations

The *CANGAROO* (Collaboration between Australia and Nippon (Japan) for a GAmma-Ray Observatory in the Outback) is the collaboration experiment between Japan and Australia since the year 1992. Two imaging air Čerenkov telescopes are being operated in Woomera (136°47′E, 31°6′S, 160m a.s.l.), South Australia. One is the 3.8 m telescope [17] and the other, the *BIGRAT* (BIcentennial Gamma-RAy Telescope). The distance between two telescopes is 100 m and stereo observations are carried out when some conditions are satisfied [73] [63]. However the observations treated in this thesis have been made only using the 3.8m telescope. Details of 3.8 m telescope are described below. A photograph of the 3.8 m telescope is shown in Figure 4.1.

4.1 The 3.8 m Telescope

The 3.8 m telescope consists of a reflecting mirror with 3.8 m diameter and an imaging camera located at the focal plane of the mirror. The focal length of the optics is also 3.8 m and the f value is $f = 1$. The mirror was originally used as a part of the receiver of the lunar laser at Dodaira, Japan. For this reason, the precision of the mirror surface is much more accurate than those of the reflectors usually used in observations of air Čerenkov images. At the focal plane, the size of an image formed by parallel rays from point object at infinity is estimated to be a few arcmin. This is much smaller than the pixel size of our camera. The mirror is composed of

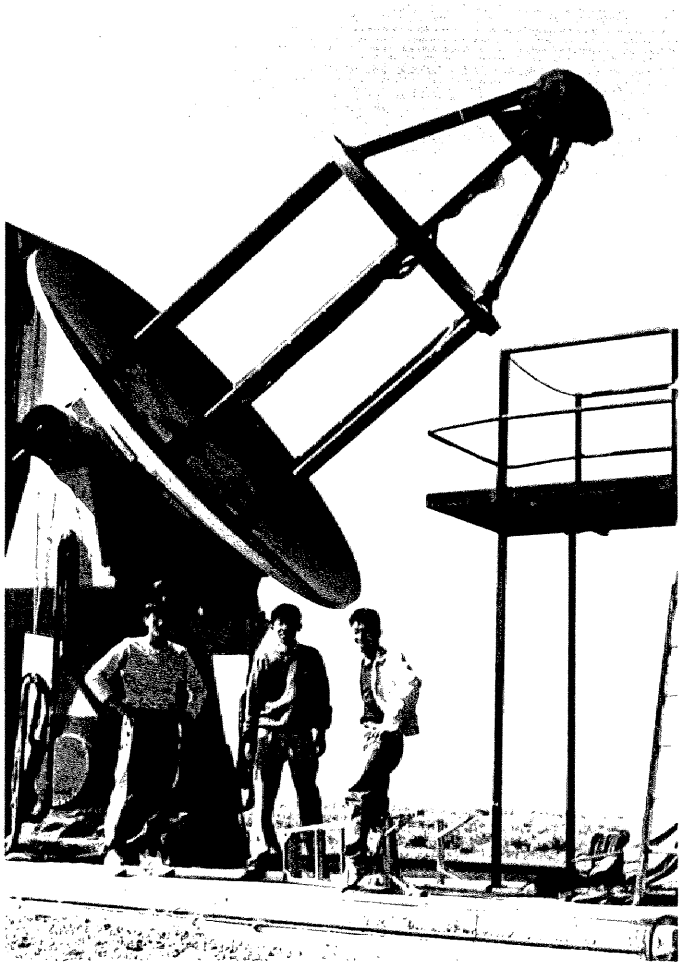

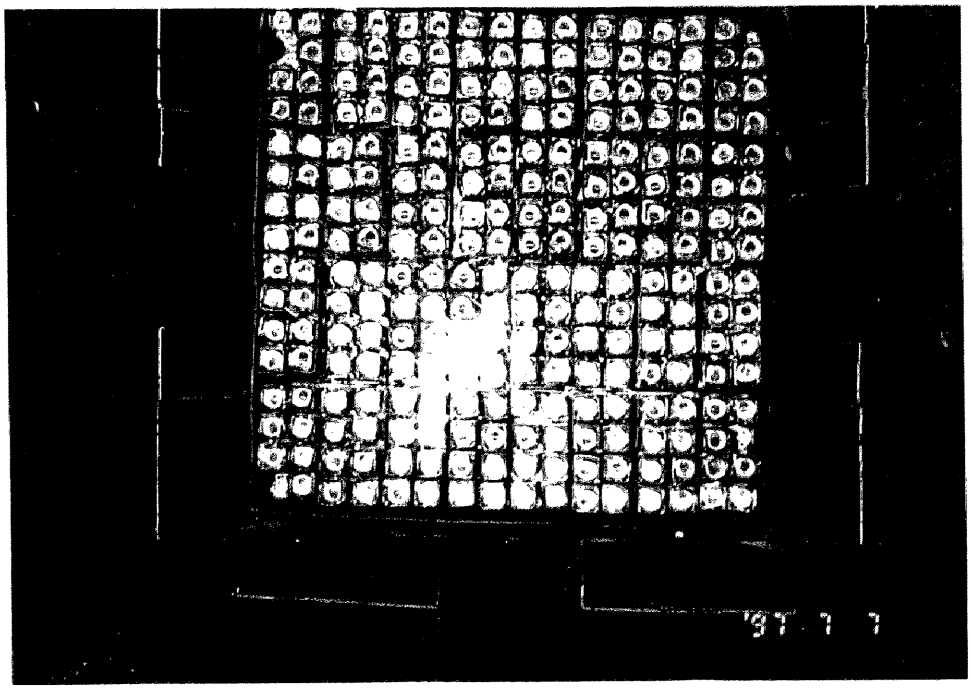

Figure 4.1: The *CANGAROO* 3.8m telescope (top).

Figure 4.2: The imaging camera of the *CANGAROO* 3.8m telescope (bottom).

one inner mirror and six outer mirrors. The combined mirror forms a parabolic surface. The reflectivity of the mirror is estimated to be about $\simeq 45\%$ in the observations of 1996. However, in October 1996, we re-coated the outer mirrors by vacuum evaporation of aluminium at the Anglo Australian Observatory (AAO). This work succeeded in improving the reflectivity of the mirror to a value $\geq 90\%$. It means that the threshold energies of observations are different between 1996 and 1997. Using Monte Carlo calculations, the gamma-ray detection threshold energies are estimated to be 4.0 TeV and 1.5 TeV for 1996 and 1997, respectively. Details of these estimations are described in Chapter 6, where the observational results are compiled.

The imaging camera consists of 256 small square shape photomultipliers (PMTs, HAMAMATSU R2248) arrayed in 16×16. A photograph of the imaging camera is shown in Figure 4.2. The size of each tube is 10 mm ($\frac{3}{8}$ inch). The PMTs are installed at an interval of 12 mm. The total field of view of the camera is about $3^\circ \times 3^\circ$ and the angular separation of each tube from its neighbour (12 mm) corresponds to $0^\circ.18$. PMT R2248 has a sensitivity in the wavelengths from 320 nm to 450 nm with an average quantum efficiency above 20 %. The rise time of an output pulse is 0.9 ns.

The 3.8 m telescope is operated using an alt-azimuth mount. The target position calculated by the control computer (NEC PC9801) and the actual direction of the telescope axis measured by encoders with a precision of $0^\circ.01$ are compared throughout the observation. A computer calculates the difference between them and sends commands to the motor drivers to correct it. The accuracy of the tracking is measured to be within the precision of the encoders, *i.e.*, $0^\circ.01$. In January 1996, the control system has been changed from a pulse motor system to an AC-servo motor system [35]. Before this change, the telescope could not follow a target at a zenith angle about $\leq 5^\circ$, where the azimuthal speed becomes high. But now, the telescope can track a target at a zenith angle 2° with an accuracy of $0^\circ.02$.

4.2 Electronics and Data Acquisition Systems

Signals from PMTs are pre-amplified in the electronics boxes located behind the camera, and are sent to the electronics hut through 30 m long cables. The PMT signals are processed

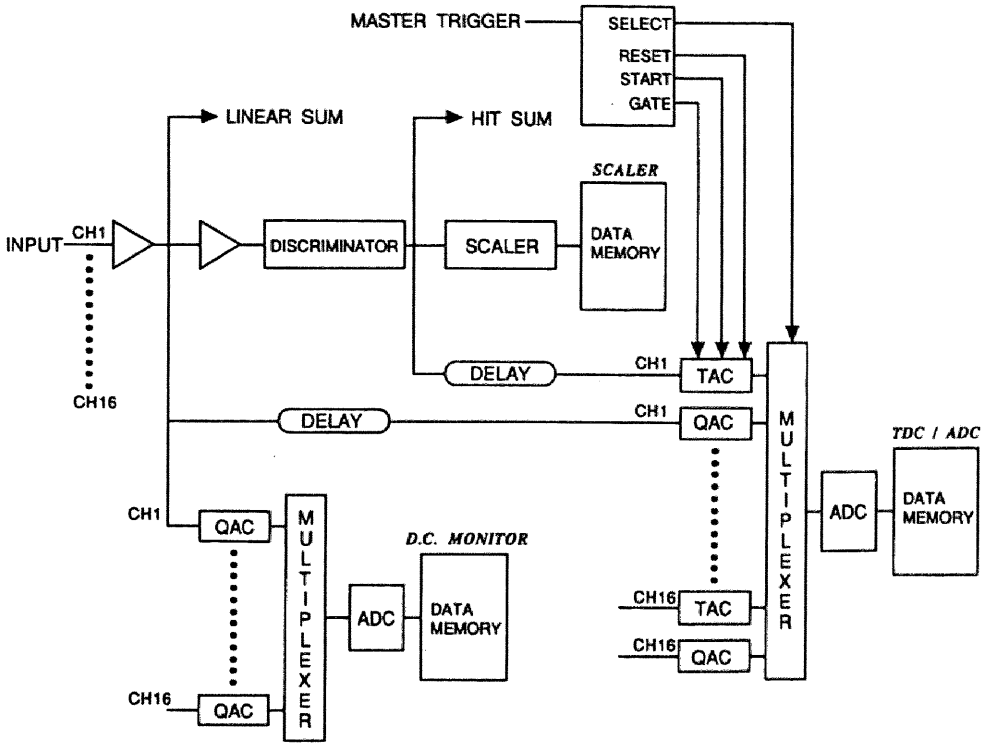

Figure 4.3: Block diagram of the functions of a CCM.

in the CCMs (Čerenkov Circuit Module) installed in the hut. Each CCM processes 16 input signals, so that 16 CCMs are installed. A block diagram of the functions in the CCMs is given in Figure 4.3. The following outputs are produced from the CCMs. ADC and TDC values and counts of hits in 1 ms of each PMT are recorded when a master trigger signal (explained below) is generated. The width of a gate pulse to obtain an ADC value is set to be 60 ns. TDC value represents a relative time interval of each PMT signal and a trigger pulse with a precision of 0.25 ns. Two kinds of analog pulses are also outputs of the CCMs. One is a summation of the amplified linear signals (namely *linear sum*) and the other represents the number of PMTs whose individual signals exceed a threshold level determined in advance (*hit sum*). *Linear sum* and *hit sum* signals coming out of the CCMs are again summed in the NIM modules. These resultant *linear sum* and *hit sum* signals are discriminated and a coincidence of the two pulses generates a master trigger to record an event (Figure 4.4). The threshold levels to discriminate each PMT signal, *linear sum* and *hit sum* are adjusted to be about 3 photoelectrons, 10 photoelectrons and 5 PMTs, respectively.

Event arrival times measured by a crystal clock are recorded as well as the information on

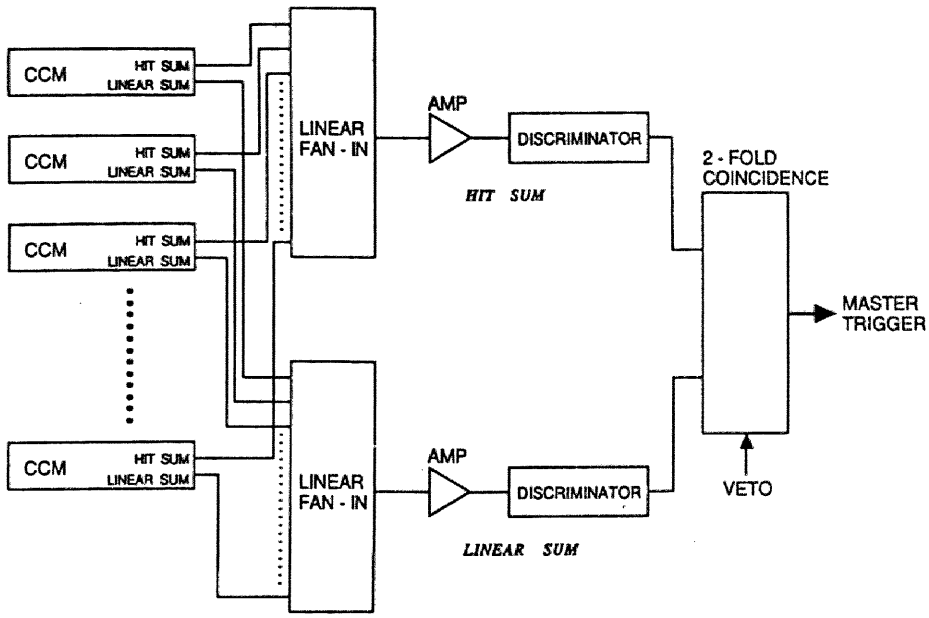

Figure 4.4: Block diagram to generate a master trigger.

PMT signals. In order to obtain absolute times, the difference of the crystal clock time and a GPS clock time is also recorded. The precision of the crystal clock and the GPS clock are 100μsec and 200 nsec, respectively. (During the installation work of the new data acquisition system, the GPS data were not available in the 1997 observations. However, the drift rate of the crystal clock has been tested using data with the GPS information and is observed to be very stable, $\Delta t/t \simeq 10^{-7}$. Although we did not have the absolute times, we could deduce relative times between the events. In the analysis of the periodicity in the 1997 data, we consider this problem further.)

Until October 1996, the data acquisition program was operated on the on board microprocessor, M68020, in which a real time operating system, OS9, was used. In November 1996, a new acquisition system using a Sun SPARC station with Sun OS4.1.3 has been installed [41]. The online program operates the CAMAC crate controller via the VME bus. Output of the CCMs, event times and some flags are led to the CAMAC modules and read by the online program. The data obtained were directly recorded on an 8 mm tape using an EXABYTE device in the old system. In the new system, data are first recorded on the hard disc and

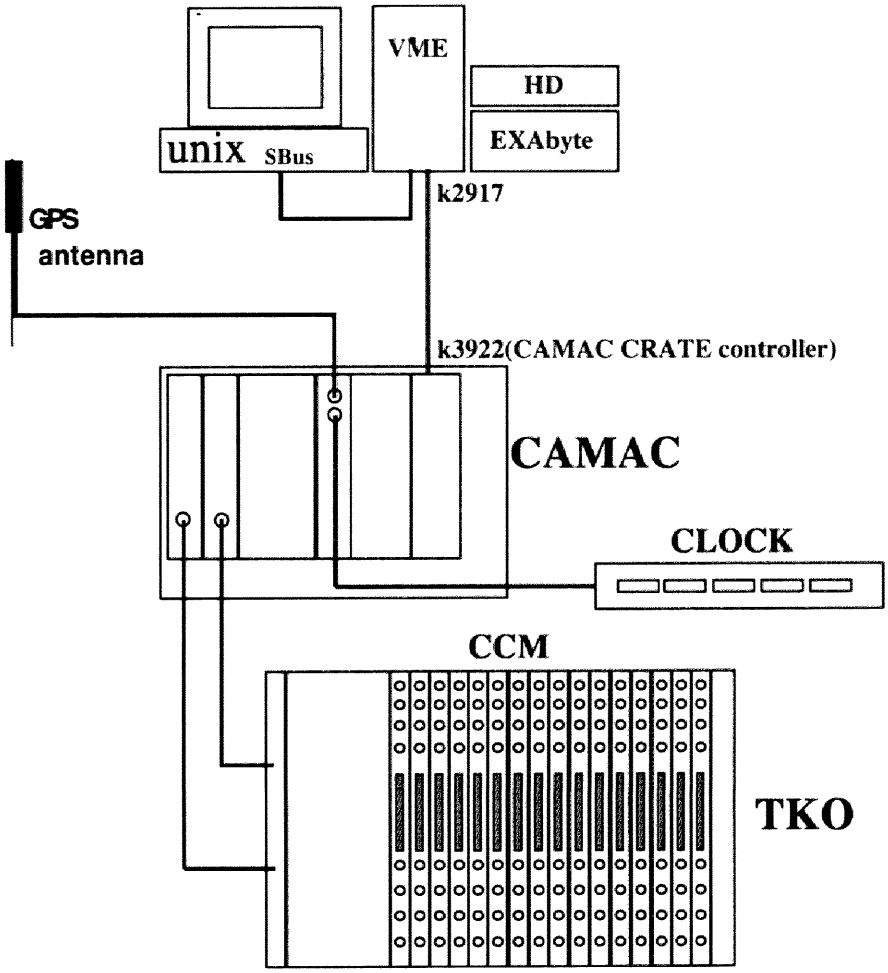

Figure 4.5: Schematic view of the present data acquisition system since November 1996.

copied to the 8 mm tape after each observation. The schematic view of the present data acquisition system is given in Figure 4.5.

4.3 Present Results of the CANGAROO

As mentioned in Chapter 1, the *CANGAROO* group has already established VHE gamma-ray emissions from three pulsar nebulae, namely the Crab [66], the Vela [84] and PSR B1706-44 [34]. Another *EGRET* pulsar PSR B1055-52 has also been observed. Since there was no detectable signal from this object, an upper limit of the gamma-ray flux is obtained. This limit is well below the extrapolation of the *EGRET* energy spectrum [63].

A marginal detection of VHE gamma-rays from the binary pulsar PSR B1259-63 is reported

4 months after the periastron in 1994 [56]. Many observations have been carried out around the latest periastron in May 1997. Analysis to confirm this earlier result is in progress.

After the *ASCA* discovery of the synchrotron emission from the shell of SN1006 [36], the *CANGAROO* have carried out observations on this supernova remnant. VHE gamma-ray emission is detected from the X-ray bright NE rim [22] [67]. No positive result is obtained from another supernova remnant W28.

In spite of the several detections and evidences of VHE gamma-ray emission from the Galactic sources, only upper limits are obtained so far for gamma-ray emission from some of the AGNs [54]. However, observations are being continued on some of these AGNs to detect any outbursts, which are common to AGNs which have been detected by other Čerenkov telescopes to emit VHE gamma-rays.

Many other possible VHE gamma-ray candidates were observed and analyses of these data are now in progress.

4.4 Observations

4.4.1 General Observations

We are observing not only the candidate object of a VHE gamma-ray source (ON source run) but also a control region to obtain background noises (OFF source run). The OFF source has the same declination as the ON source, but a different right ascension. The observation times and the trajectories of ON and OFF sources are adjusted to match in each night within the allowance of observation conditions. By the word "conditions", we mean the weather conditions, existence of bright stars in the field, time of the moon rise or moon set and so on. At the beginning of each run (ON source run and OFF source run) and the end of each observation, two kinds of calibration run are performed. One is to obtain the pedestal value of ADC (pedestal run). In this run, using artificially generated trigger pulses from a pulse generator, "no-image" data are recorded. The other run is made to examine the uniformity of the gain of PMTs. Lights pulses with widths of 20nsec from a blue LED, set at the center of the mirror, illuminate the camera uniformly and the "uniform-images" are recorded. Both kinds

of calibration data are obtained for about 2000 triggers in each run and used to normalize the ADC values obtained in the actual shower observations.

4.4.2 Observations of PSR B1509-58

In the ON source run, the axis of the telescope is pointed to (right ascension, declination ; both J2000 coordinates)= ($15^h13^m55^s.62$, $-59°\ 08'\ 08''.9$), which is the pulsar position listed by Taylor, Manchester and Lyne [68] (latest information is available by the anonymous ftp service described in this reference). The observation times of PSR B1509-58 are summarized in Table 4.1. For the raw data, some data reductions are applied in the pre-analysis, which is described in Section 5.1. The times after this procedure are also summarized in Table 4.1.

Table 4.1: Total observation times of PSR B1509-58. The total times selected for the analysis in this thesis are also presented.

Observation	ON Source		OFF Source	
Period	Raw	Selected	Raw	Selected
1996 (Total)	$53^h\ 35^m$	$40^h\ 32^m$	$50^h\ 30^m$	$42^h\ 10^m$
1997 (Total)	$42^h\ 44^m$	$32^h\ 08^m$	$41^h\ 09^m$	$32^h\ 08^m$
1997 (March)	$6^h\ 10^m$	$5^h\ 45^m$	$6^h\ 10^m$	$5^h\ 45^m$
1997 (April)	$13^h\ 04^m$	$9^h\ 58^m$	$11^h\ 19^m$	$9^h\ 58^m$
1997 (May)	$23^h\ 30^m$	$16^h\ 25^m$	$23^h\ 40^m$	$16^h\ 25^m$

Some comments are needed for these particular observations. As already mentioned, the reflectivity of the 3.8 m mirror is different between the observations of 1996 and 1997. It means that the threshold energies of two years' observations are different. In the observations of 1996, there was a severe electrical noise problem. Moreover, weather conditions, which were worse than the usual, made it difficult to match the observation times of ON and OFF sources each night. Although the total observation and selected times of the 1996 data are similar, the trajectories of ON and OFF source runs were not matched. Finally, in the 1997 observations, when the GPS clock data were not recorded, the absolute arrival times of the events were not available. However, since the crystal clock is proved to be very stable, the relative times of the events can be used for the periodicity analysis in each observation period (in this case, March, April and May).

Chapter 5

Analysis and Results

In this Chapter, the analysis methods and their results are presented for both the 1996 and 1997 data. Detailed discussions of these results, especially the statistical discussions, are presented in Chapter 6.

5.1 Pre-Analysis (Image Reconstruction)

5.1.1 Calibrations of PMT Properties.

Before the *image parameters* are calculated, some properties of each PMT are derived using the data from calibration runs. First, *ADC pedestal* values are deduced as the averaged ADC values obtained in the pedestal runs. An *ADC signal* is defined as an excess ADC count over the *ADC pedestal* value. Standard deviations of the *ADC pedestal* value are also calculated. Typical value of the standard deviation is $\simeq$10 ADC counts, which corresponds to $\simeq$1 photoelectron. Next, the averaged ADC values obtained in the LED runs are calculated and the excess counts above the *ADC pedestal* values, *gains*, are deduced for each PMT. Here, because we are assuming that the LED uniformly illuminates the whole camera, the *gain* values ideally should be identical. Actual variations of the *gain* values are used to normalize the *ADC signals* obtained in the shower observations. When ADC_i, ADC_i^{ped}, $GAIN_i$ are defined as the ADC value including shower Čerenkov light, the *ADC pedestal* and the *gain* value obtained above for a PMT number i,

$$SIG_i^{norm} \equiv (ADC_i - ADC_i^{ped}) \times \frac{< GAIN_i >}{GAIN_i} \tag{5.1}$$

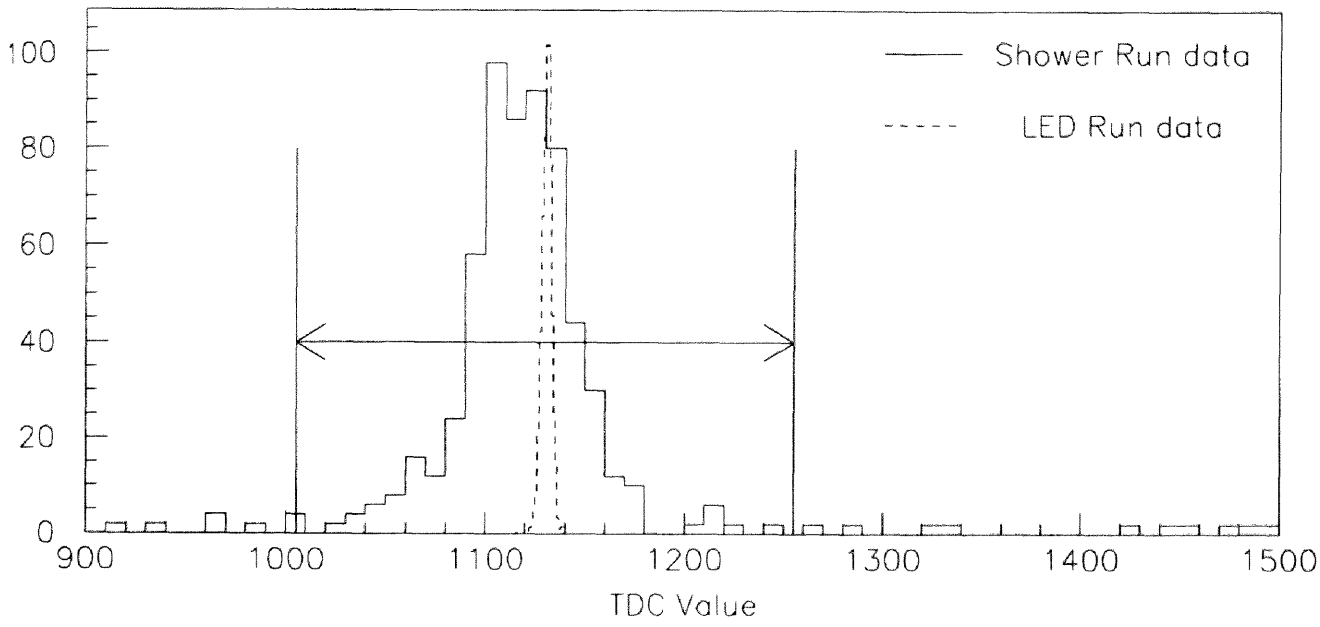

Figure 5.1: Distribution of TDC values of a PMT in a shower run as well as that in an LED run.

is used to calculate the normalized *ADC signal*, SIG_i^{norm}. In the above formula, $< GAIN_i >$ means the averaged $GAIN_i$ over all the PMTs.

TDC value is useful to remove noises (see below) caused by the night sky background, stars or electrical fluctuations, which are distributed with random timing. A distribution of TDC value for a PMT obtained in a shower run is shown in Figure 5.1. Riding above a uniform distribution, we can find a clear peak, which corresponds to the signals caused by Čerenkov lights emitted from air showers. As shown in Figure 5.1, the timing of the LED pulse is adjusted to have the same TDC peak with shower peak. The averaged TDC values obtained in the LED run are used as the *TDC pedestal*.

5.1.2 Criteria to Deduce Image Parameters

To select the PMT pixels, which include Čerenkov light signals (*hit pixel*), the criterion below are applied.

$$ADC_i - ADC_i^{ped} \geq RMS_i^{ped} \tag{5.2}$$

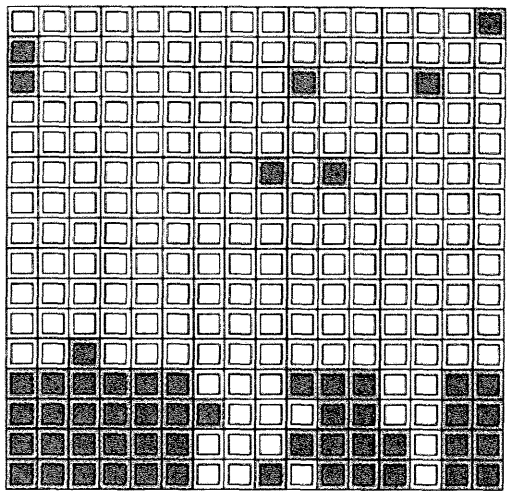

Figure 5.2: Positions of PMTs, having some problems, which were masked in the analysis of the 1996 data.

$$|TDC_i - TDC_i^{ped}| \leq 120\ counts \tag{5.3}$$

RMS_i^{ped}, TDC_i and TDC_i^{ped} are the standard deviation of the *ADC pedestal*, observed TDC value and the *TDC pedestal*, respectively for the ith PMT. The half width of the TDC window, 120, corresponds to 30 nsec. The pixels, which do not satisfy both the above two criteria, are thought to be "no signal" pixels and SIG_i^{norm} are set to be zero for those pixels.

In addition to the "no signal" criteria above, a cut which we describe as the "isolate" cut is applied. If a *hit pixel* has no *hit pixel* in its 8 neighborhoods, the "isolated" *hit pixel* is also regarded as a "no signal" pixel.

Some PMTs became inefficient or noisy during later times under the harsh climate conditions. Such tubes found in the calibration runs are regarded as "dead tubes", and SIG_i^{norm} are also set to be zero. In the observations of 1996, there were severe electric noise problems. In the analysis of the 1996 data, 54 pixels are masked as "dead tubes" to avoid such a noise. As shown in Figure 5.2, a large number of "dead tubes" are concentrated in the lower part of the camera. It mostly affects to reduce the effective area.

Using the normalized signal, SIG_i^{norm}, of *hit pixels*, the image parameters are calculated.

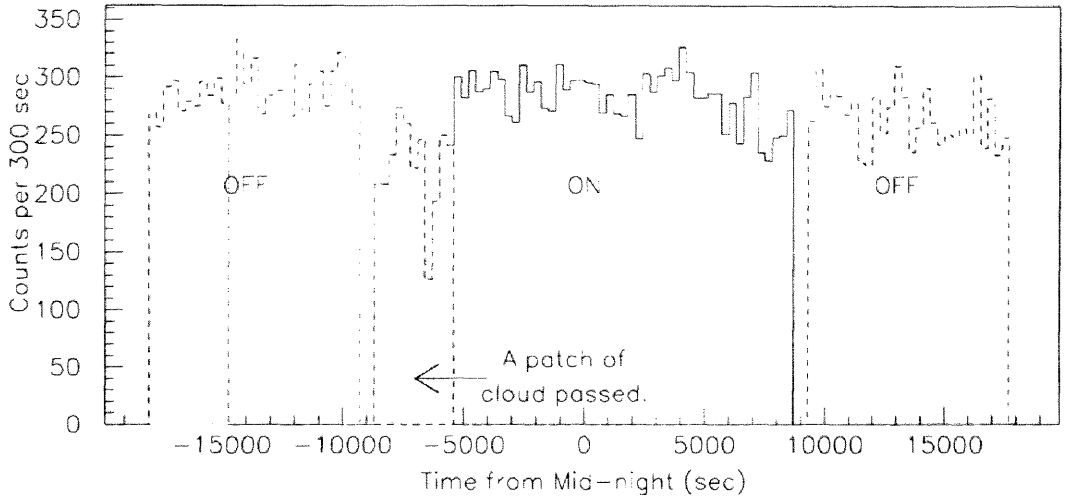

Figure 5.3: Variation of the trigger rate in a night. At the beginning of the ON source run, a patch of cloud passed in front of the target and the trigger rate decreased. The data during the cloudy time are removed from the analysis. The corresponding OFF source data, which have the same trajectory as that of the removed ON source data, are also removed from the analysis. Both the removed times are indicated by shaded areas.

5.1.3 Event Reduction

After reconstructing the image parameters, the counting rates are examined. Observations are usually carried out under the fine conditions, but sometimes unavoidable changes of the condition (passing of cloud in the field of view, electrical noise and so on) happen. An example of the variation of the counting rate in a certain night is shown in Figure 5.3. A significant decrease of the counting rate is seen at the beginning of the ON source run. It is consistent with the record in the logbook, where a passing of a patch of cloud is recorded. Like in this case, when a sudden change of the counting rate is found with a certain reason, the events during that time are removed from the analysis. At the same time, the events, having same trajectory as the removed period in the corresponding run (OFF(ON) source run against ON(OFF) source run), are also removed. This procedure is also shown in Figure 5.3. In the observations of 1996, there were so many sudden changes of the conditions. That made it impossible to match the trajectory between the ON and OFF source runs night by night.

The total observation times after these data reduction are summarized in Table 4.1. These data are used in the successive sections.

5.2 Conventional Analysis at the Pulsar Position

To deduce the *orientation parameters*, the *alpha*, *distance*, *asymmetry*, the origin of the coordinate system should be defined first. Hereafter, the origin is called the *assumed source position*. In this case, it is the pulsar position in the field of view. Although the tracking error of the telescope is less than 0°.01, there could be an error in adjusting the camera center on the tracking axis. This error is found to be about 0°.10 at the maximum. The position of the real tracking center on the camera is calculated by a calibration program [83] using the rotation of the bright stars in the field. The accuracy depends on the condition of the field (the number, the track lengths and the magnitudes of the stars), but in the case of PSR B1509-58, the error could be well less than 0°.02. The tracking centers are deduced for each night using the ON source data and the *orientation parameters* are calculated with respect to the tracking centers.

The *shape* and *orientation parameters* calculated with reference to the pulsar position are shown in Figures 5.4 and 5.5 for the ON and OFF sources for the 1996 and 1997 data, respectively. The 1996 OFF source data were multiplied by a factor 0.961 to take the difference of the ON source and OFF source observation times into account. The distributions of the parameters well agree with the simulated ones shown in Figure 2.6. Two parameters, the *distance1* and *distance2*, are defined as the distances from the center of the camera and the assumed source position, respectively. The images located near the edge of the camera will not show the correct values of the parameters because part of such an image is outside of the camera. To remove those events, the *distance1* is used. It owes to the property of the detector. On the other hand, the *distance2* represents the nature of the EASs and the distribution depends on the directions and the core distances of the EASs. The distribution of *distance2* of Monte Carlo gamma-ray images without an effect of the finite size of the camera is shown in Figure 5.6. It is important when an assumed source position offset by a large value from the camera center is examined.

To reduce the number of events caused by hadron background and enhance the weak gamma-ray signals, the selection criteria below are adopted for the *image parameters*.

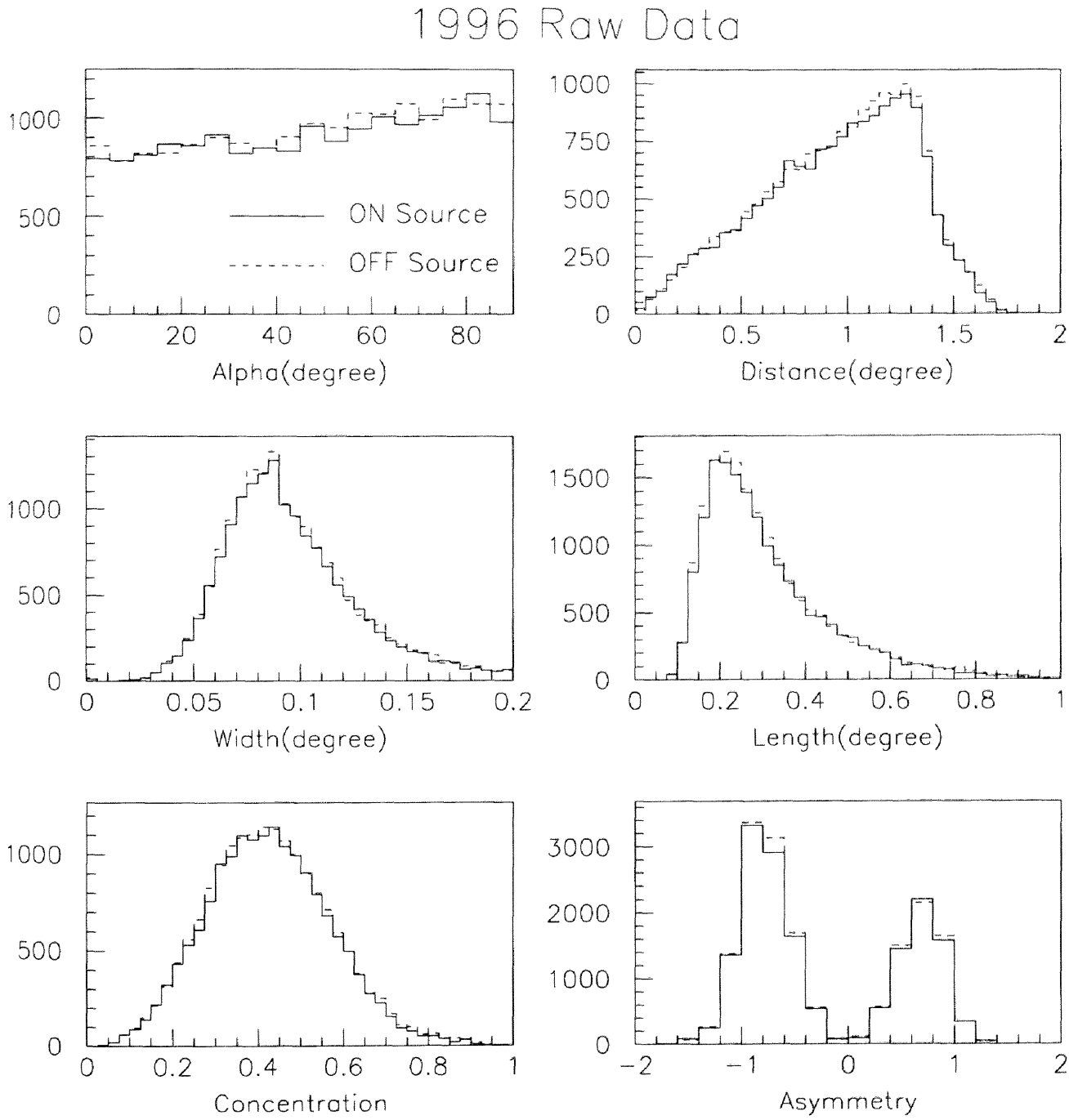

Figure 5.4: Distributions of the *image parameters* of the 1996 data. Solid lines show the distributions of the ON source data. Dashed lines show those of the OFF source data. A factor 0.961 is used to multiply the OFF source counts to take the difference of the observation times of the ON and OFF source runs into account.

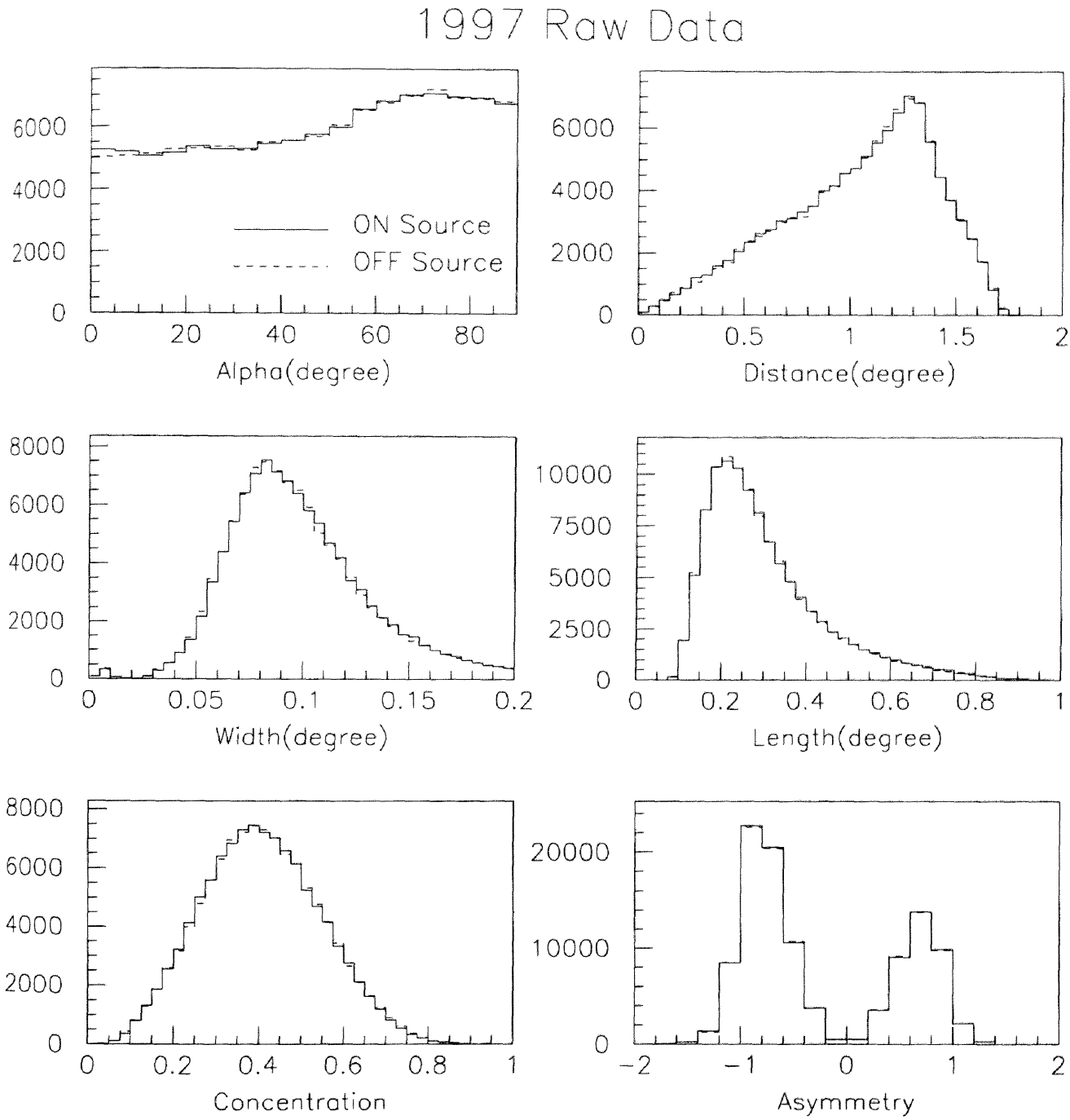

Figure 5.5: Distributions of the *image parameters* of the 1997 data.

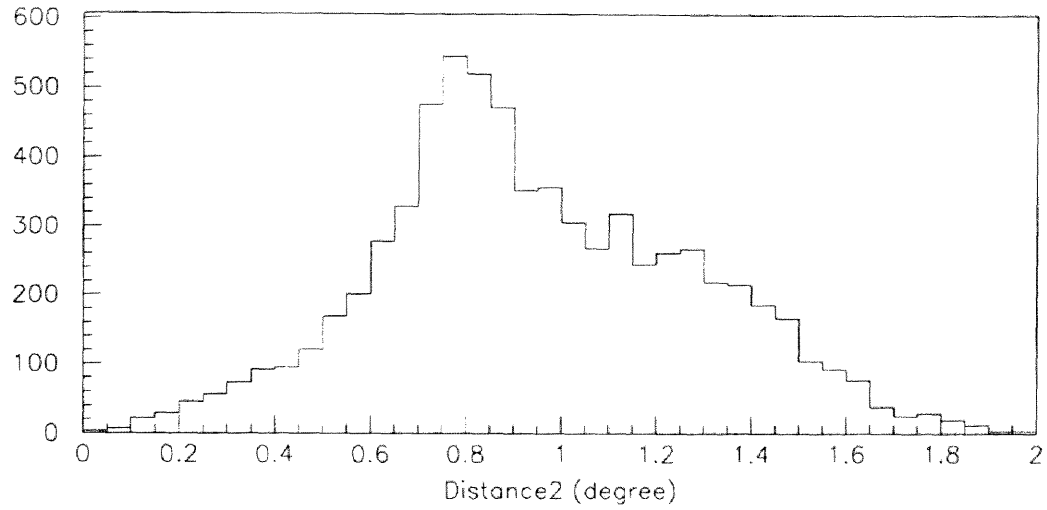

Figure 5.6: Distribution of the *distance2* parameter, which is defined to avoid the effect of the edge of the camera. Actually, an angular size of 10° × 10° camera is assumed to obtain this distribution.

$$
\begin{aligned}
&\textit{Number of hit tube} \geq 5 \\
&\textit{Total photoelectron} \geq 20 \\
&\textit{distance1} \leq 1°.05 \\
&0°.60 \leq \textit{distance2} \leq 1°.30 \\
&0°.04 \leq \textit{width} \leq 0°.09 \\
&0°.10 \leq \textit{length} \leq 0°.40 \\
&0.35 \leq \textit{concentration} \leq 0.70
\end{aligned} \tag{5.4}
$$

The number of events at each stage of the cuts are listed in Table 5.1, 5.2 for the 1996 and 1997 data, respectively. In order to show the power of the image cuts, the ratio of the number of the OFF source counts after the cuts to the number before any cuts are made is given. The ratio is normalized for the counts before the *distance1* cut. The statistical significances of the excess in the ON counts are also calculated for the total counts after each cut and counts at $alpha \leq 10°$.

The distributions of the *alpha* parameter after all the cuts are shown in Figure 5.7. In the 1997 result, an excess of counts is found in the ON source data at $alpha \simeq 0°$. This means

Table 5.1: The number of events at each stage of the cuts for the 1996 data. No clear excess of the ON source counts is found.

Cut	ON Source		OFF Source		Significance		N_{OFF}
	Total	*alpha* $\leq 10°$	Total	*alpha* $\leq 10°$	Total	*alpha* $\leq 10°$	ratio
N_{hit} *and*							
Total p.e.	16447	1574	17624	1702	-2.70	-1.09	1.00
*distance*1	9073	979	9550	1080	-0.78	-1.32	0.541
*distance*2	6083	635	6388	697	-0.51	-0.97	0.362
width	2783	315	2895	321	0.01	0.26	0.164
length	2367	281	2460	279	0.04	0.55	0.139
concentration	2078	248	2170	246	-0.11	0.53	0.123
alpha	248		246		0.53		0.013

Table 5.2: The number of events at each stage of the cuts for the 1997 data. We can see the excess of the ON source counts at *alpha* $\leq 10°$ becomes progressively more significant with each additional cut. After all the cuts, the backgroud events are reduced to be 1% of the data before *distance* cut.

Cut	ON Source		OFF Source		Significance		N_{OFF}
	Total	*alpha* $\leq 10°$	Total	*alpha* $\leq 10°$	Total	*alpha* $\leq 10°$	ratio
N_{hit} *and*							
Total p.e.	107495	10464	107574	10111	-0.17	2.46	1.00
*distance*1	48511	5650	48052	5401	1.47	2.37	0.446
*distance*2	33510	4005	33249	3712	1.01	3.34	0.309
width	14564	1806	14528	1606	0.21	3.42	0.135
length	12145	1586	12113	1369	0.20	3.99	0.112
concentration	10644	1388	10696	1180	-0.35	4.10	0.099
alpha	1388		1180		4.10		0.010

an evidence for the detection of VHE gamma-ray signals from the source. The enhancement of the gamma-ray like signals is also seen in Table 5.2 with each additional cut. On the other hand, in the 1996 result no significant excess is found at *alpha* $\simeq 0°$.

The significance of excess is defined as [37],

$$significance = \frac{N_{ON} - kN_{OFF}}{\sqrt{N_{ON} + k^2 N_{OFF}}} . \tag{5.5}$$

N_{ON} and N_{OFF} are the summed counts of the ON and OFF source data at *alpha* $\leq 10°$. k is the normalization factor to multiply N_{OFF} to take into account of the difference of the observation times between the ON source and the OFF source. In our cases, $N_{ON} = 248$, $N_{OFF} = 246$ and $k = 0.961$ for the 1996 data and $N_{ON} = 1388$, $N_{OFF} = 1180$ and k is unity for the 1997 data.

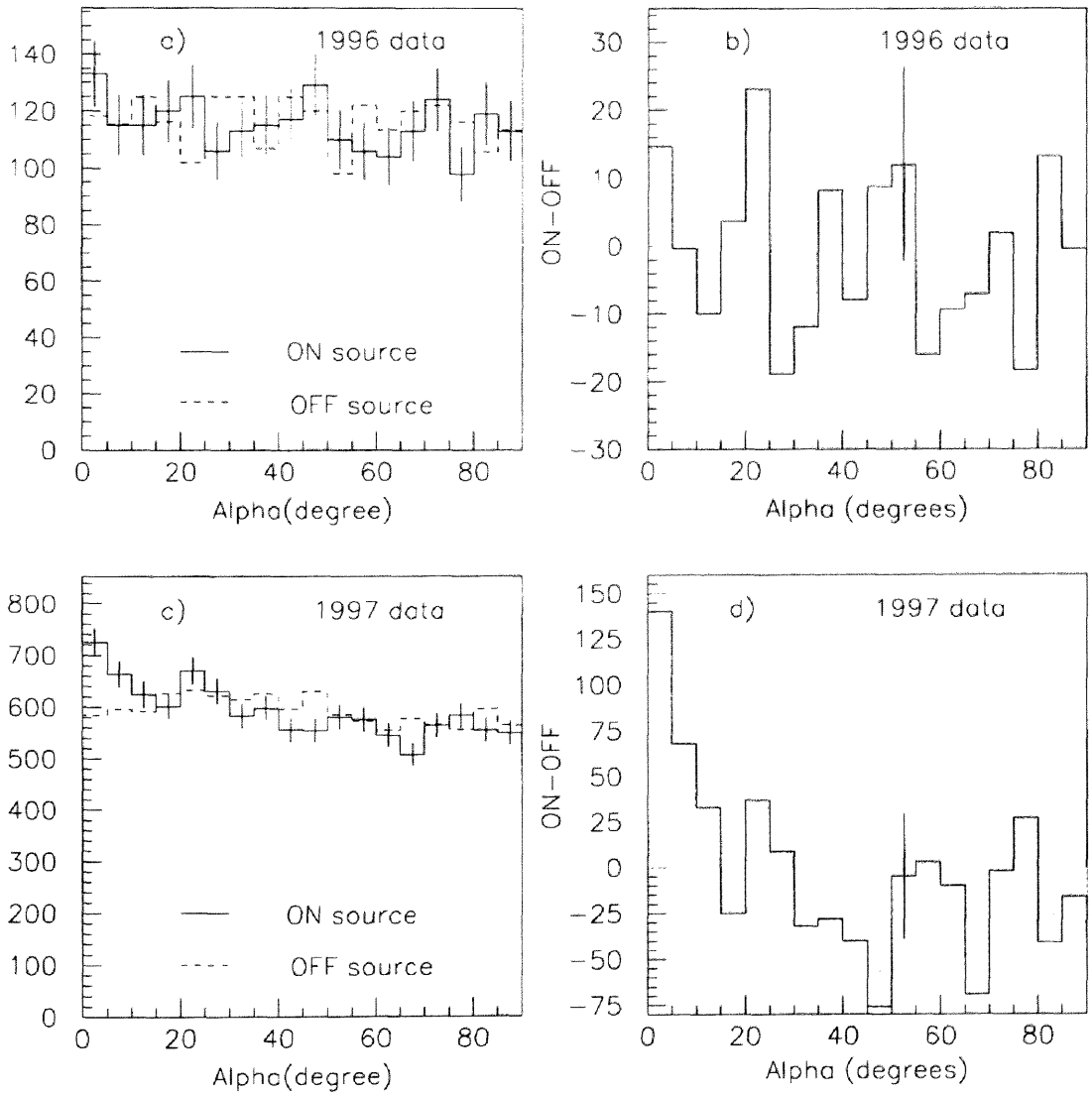

Figure 5.7: Distributions of the *alpha* parameter after all the image cuts. In the 1997 data (c,d), an excess at *alpha* $\simeq 0°$ is clearly found. It indicates a possible detection of gamma-ray signals. On the other hand, there is no excess seen in the 1996 data (a,b).

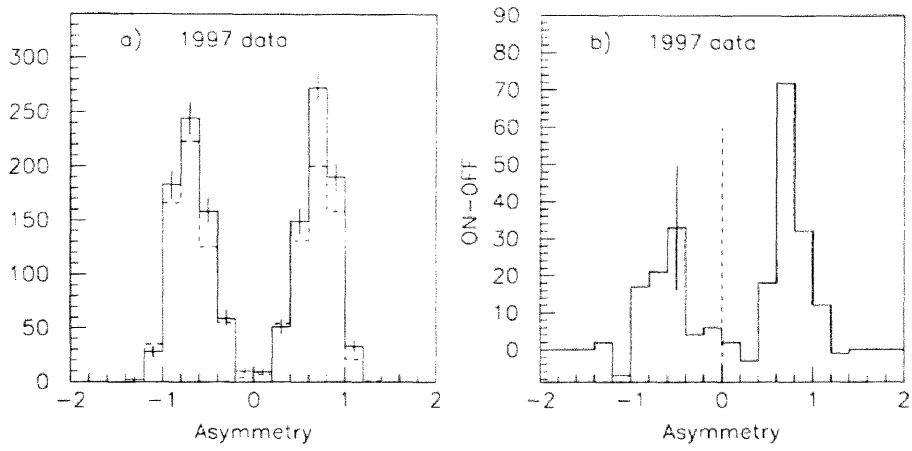

Figure 5.8: Distributions of the *asymmetry* parameter of the 1997 data after all the image cuts and *alpha* $\leq 10°$. Excess of the ON source counts in the positive values shows a tendency of gamma-ray signal.

The resultant significances are 0.53 σ and 4.10 σ for the 1996 and 1997 results, respectively.

To confirm the positive result of the 1997 data, the *asymmetry* parameter is examined. The *asymmetry* parameter reflects the direction of the shower development with respect to the assumed source position. As shown in Figure 2.7, the *asymmetry* parameter of Monte Carlo gamma-ray images has an excess in the positive value because the showers develop outward from the source position. On the other hand, for the isotropic hadron showers, the *asymmetry* value obtained from Monte Carlo calculations distributes evenly in the positive and negative values. The distributions of the *asymmetry* values are shown in Figure 5.8 using the events having *alpha* $\leq 10°$. In the right-hand side panel of Figure 5.8, which shows ON − OFF counts, an excess of events in the positive value of the *asymmetry* parameter is seen. Although the excess is not strong like the one obtained from a Monte Carlo calculation, this result represents the tendency of VHE gamma-ray signal. A statistical argument for this result is presented in Section 6.1.1.

The consistency between the 1996 and 1997 results are discussed in Section 6.2.2.

5.3 Source Position Studies (Standard Method)

In the previous section, we assumed that the source position was the same as the pulsar position. However, since the environment around the pulsar is complicated, it is possible that

the VHE gamma-ray emission is not from the pulsar position. To examine this possibility, a search for the emission position has been carried out. The $2° \times 2°$ field centered on the pulsar is divided into 41×41 matrix. Every mesh point is considered to be an assumed source position to calculate the *orientation* parameters(*alpha*, *distance2* and *asymmetry*). For each mesh point, a distribution of the *alpha* parameter is obtained like the one in Figure 5.7. The criteria for the *shape* parameter cuts are the same as those adopted in the previous section. Statistical significance is calculated for each point and the maps of the significance are shown in Figure 5.9 for the 1996 and 1997 data.

In the significance map of the 1996 data, no significant excess is found not only at the pulsar position but at any other position in the whole field of the map. In the 1997 result, we can find a clear excess of the significance around the pulsar position. The position of the maximum excess is found at 0°.10 west and 0°.05 south from the pulsar position. The distance between the pulsar and the maximum excess position is 0°.11. A typical precision to determine the source position using an imaging air Čerenkov telescope is thought to be $\simeq$ 0°.1. However, because it depends on the individual case, a detailed estimation of the precision to determine the source position is postponed to Section 6.1.2. The statistical significance at this position is calculated to be 4.90 σ using Equation (5.5). (N_{ON}=1393, N_{OFF}=1146 are actual counts at *alpha* $\leq$ 10° and k=1.) A more proper value of the significance taking into account of the degrees of freedom in the source search is also estimated in Section 6.1.3.

5.4 Source Probability Density Function

To examine the source position of the 1997 data more precisely, analyses using the *Source Probability Density Function (SPDF)* method proposed by Yoshikoshi [83] and the extended *SPDF* method proposed in this thesis are applied in this section.

5.4.1 Original SPDF

In the method used in the previous section, the candidate position of the source for each shower is located uniformly in the area of 0° < *alpha* $\leq$ 10° and 0°.60 < *distance2* $\leq$ 1°.30. However, the probability for the existence of the source should be a function of the position

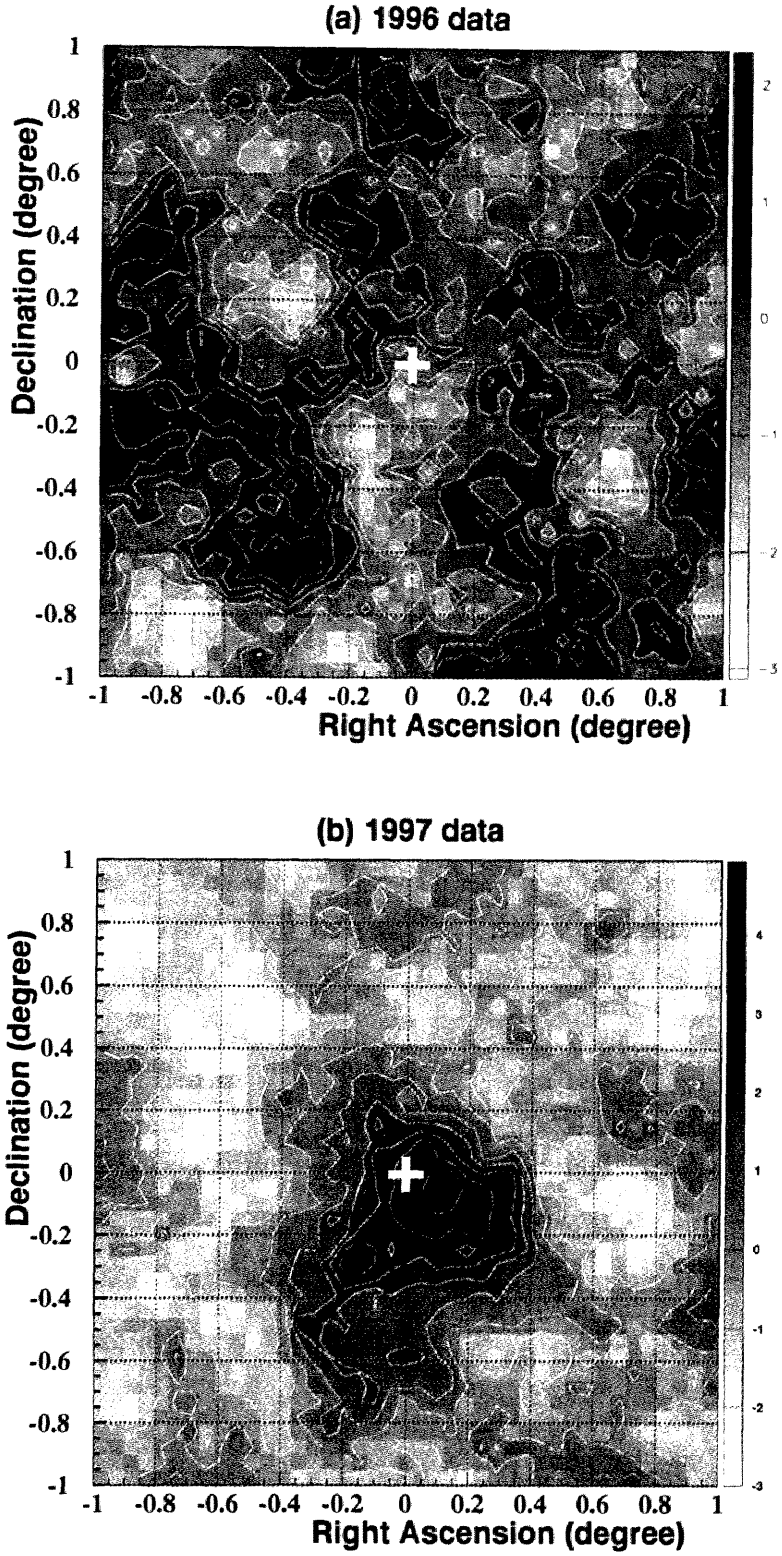

Figure 5.9: Statistical significance maps of the 1996 data (a) and the 1997 data (b). The field of view is 2° × 2° centered at the pulsar position (indicated by the cross in the figures).
The darker the shade, the more significant is the signal. The inner-most contour in (b) has a statistical significance of 4.5σ and the contour level separation is 1.0σ.

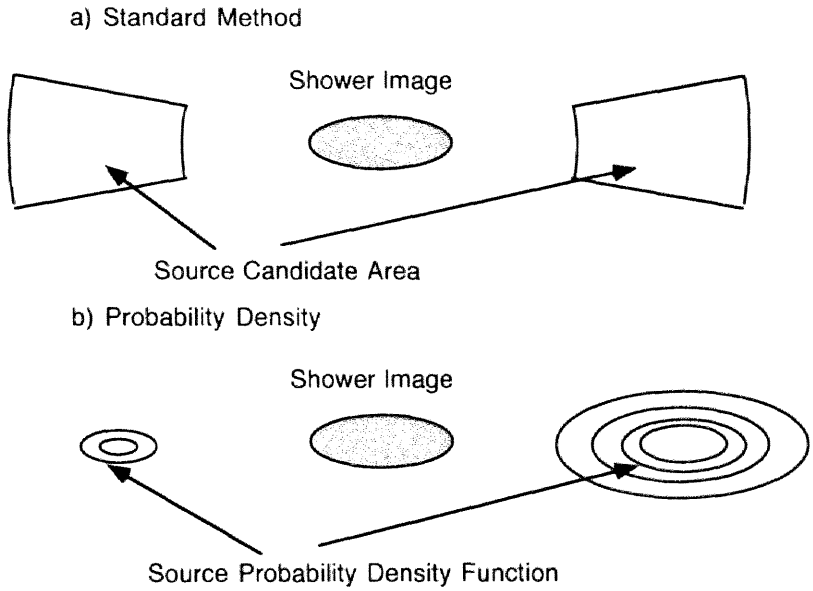

Figure 5.10: Difference of the *standard* method and the *SPDF* method for a source search.

with respect to the shower image. This function is named the *SPDF* and it is determined using Monte Carlo images of gamma-rays. The difference between these two methods is schematically drawn in Figure 5.10. The *SPDF* was defined in the coordinate system, which has the x-axis along the major axis of the shower image and the y-axis perpendicular to the x-axis. The centroid of the Monte Carlo shower images are set to be the origin of the coordinate system and the distribution of the corresponding source positions is fitted to a two dimensional Gauss function. Since the nature of the gamma-ray shower is asymmetric with respect to the y-axis, the *SPDF* has asymmetrical feature. The positive direction of the x-axis is defined as a region having larger probability density. The *SPDF* is symmetric with respect to the x-axis. The actual form of the *SPDF* proposed by Yoshikoshi [83] is,

$$
\begin{aligned}
P(x,y) \;=\; & \frac{f}{2\pi\sigma_{x1}\sigma_{y1}} exp\left[-\frac{1}{2}\left\{\left(\frac{x-d_1}{\sigma_{x1}}\right)^2+\left(\frac{y}{\sigma_{y1}}\right)^2\right\}\right] \\
& +\frac{1-f}{2\pi\sigma_{x2}\sigma_{y2}} exp\left[-\frac{1}{2}\left\{\left(\frac{x+d_2}{\sigma_{x2}}\right)^2+\left(\frac{y}{\sigma_{y2}}\right)^2\right\}\right] . \qquad (5.6)
\end{aligned}
$$

f is the fraction of the events, which has positive *asymmetry* value. d_1 and d_2 are the mean distances from the center of the image to the source along the x-axis in positive and negative

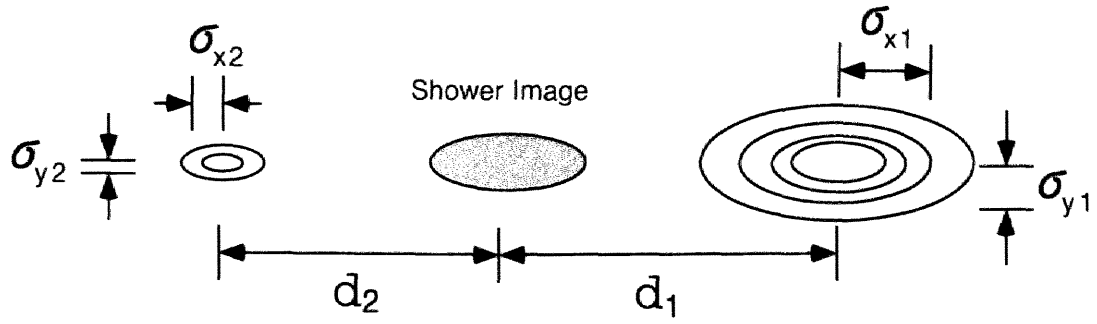

Figure 5.11: Definitions of the parameters used in the *SPDF* analysis. These values are obtained using Monte Carlo gamma-ray images.

values, respectively. σ_{x1}, σ_{x2}, σ_{y1} and σ_{y2} are the standard deviations along the x-axis and y-axis (Figure 5.11). These *SPDF parameters* are determined using Monte Carlo calculations to be,

$$\begin{aligned} f &= 0.829 \\ d_1 &= 0°.931,\ \sigma_{x1} = 0°.248,\ \sigma_{y1} = 0°.083 \\ d_2 &= 0°.981,\ \sigma_{x2} = 0°.266,\ \sigma_{y2} = 0°.107. \end{aligned} \tag{5.7}$$

To deduce a significance map using the *SPDF*, the probability density $P(x,y)$ is calculated for each mesh point for each event. When the summations of the $P(x,y)$ and $P^2(x,y)$ over all the selected events $(k = 1, ..., n)$ are defined as,

$$S(i,j) = \sum_{k=1}^{n} P(x_{(i,j),k}, y_{(i,j),k}) \tag{5.8}$$

$$\sigma^2(i,j) = \sum_{k=1}^{n} P^2(x_{(i,j),k}, y_{(i,j),k}) \tag{5.9}$$

$$\tag{5.10}$$

The significance at the $(i,j)th$ mesh point is expressed as,

$$significance = \frac{S_{ON}(i,j) - S_{OFF}(i,j)}{\sqrt{\sigma^2_{ON}(i,j) + \sigma^2_{OFF}(i,j)}}. \tag{5.11}$$

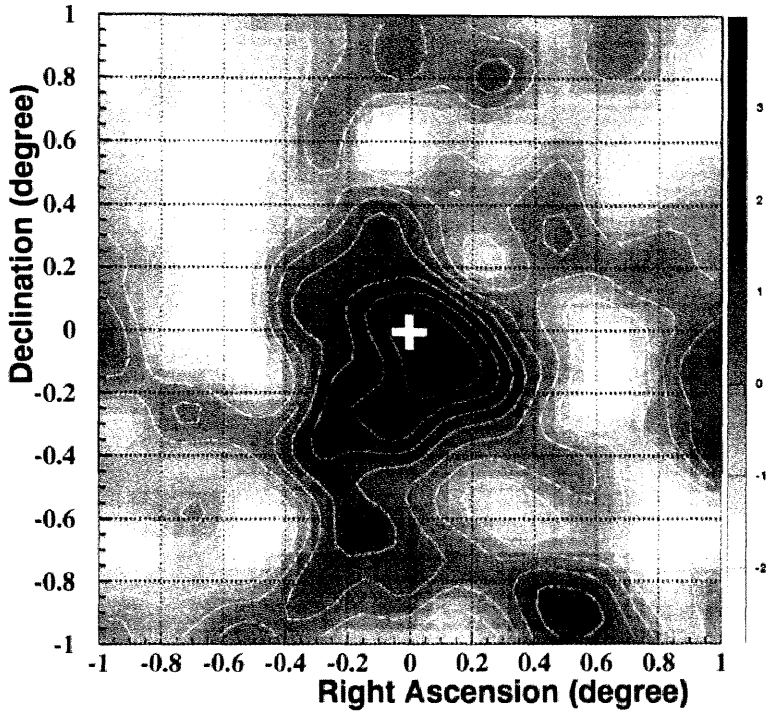

Figure 5.12: Statistical significance map for the 1997 data obtained using the *SPDF* method. The position of the pulsar is also indicated by a cross. The inner-most contour has a significance of 3.5 σ.

The significance map obtained using the *SPDF* is shown in Figure 5.12. No significant difference in the source position can be found compared with the *standard* method analysis (see Figure 5.9) described in the previous section. Unfortunately, as mentioned in Section 5.2, the distribution of the *asymmetry* did not *ideally* represent the expectation of the Monte Carlo calculations. It, therefore, results in a decrease of the significance because the asymmetrical feature is included in the *SPDF*. Since the problem of the *asymmetry* parameter will be discussed in Section 6.1.1, a step-up of the *SPDF* is proposed here for a more improved source localization.

5.4.2 Extended SPDF

As a natural extension of the *original SPDF*, an *image parameter* dependence of the *SPDF parameters* is examined. (In the *original SPDF*, the *SPDF parameters* are treated as constants.) As illustrated in Figure 5.13, it can be imagined that the *SPDF parameters* will depend on the *length* parameter. A gamma-ray shower having a small core distance makes an image near the source position on the focal plane. Such an image tends to have a small *length* value. It

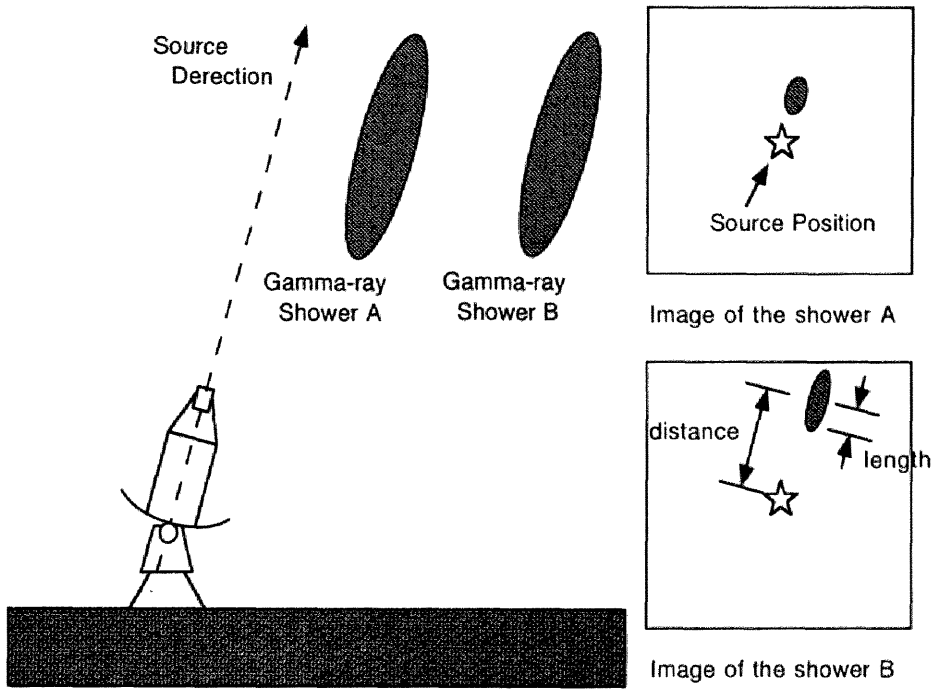

Figure 5.13: Concept to introduce the *extended SPDF*. Correlation between the *distance* and the *length* parameters is expected.

means the d and σ_x parameters in the *SPDF* become smaller than the averaged values over a wide range of the possible core distance of EASs. For an EAS with a large core distance, all the arguments above become opposite. The d and σ_x parameters as well as the σ_y parameter are determined as "functions of the *length* parameter". In the procedure to determine these functions, the Monte Carlo images of gamma-ray initiated showers are divided every 0°.04 of the *length* parameter. Examples of the distributions of the source distance projected on to the x-axis (D_1 and D_2) and y-axis (d_{y1} and d_{y2}) are shown in Figure 5.14 for a range of the *length* parameter, $0°.14 < length \leq 0°.18$. As mentioned in Section 5.2, a sufficiently large camera is assumed in these calculations to avoid the effect of the edge of the camera. All the distributions are fitted to Gaussian and the resultant mean values and standard deviations are listed in Table 5.3. These values as well as the f value are fitted again to the functions of the *length* parameter (Figure 5.15). The finally obtained functions are,

$$d_1 = -0.147 + 5.95 \times length - 5.27 \times length^2$$

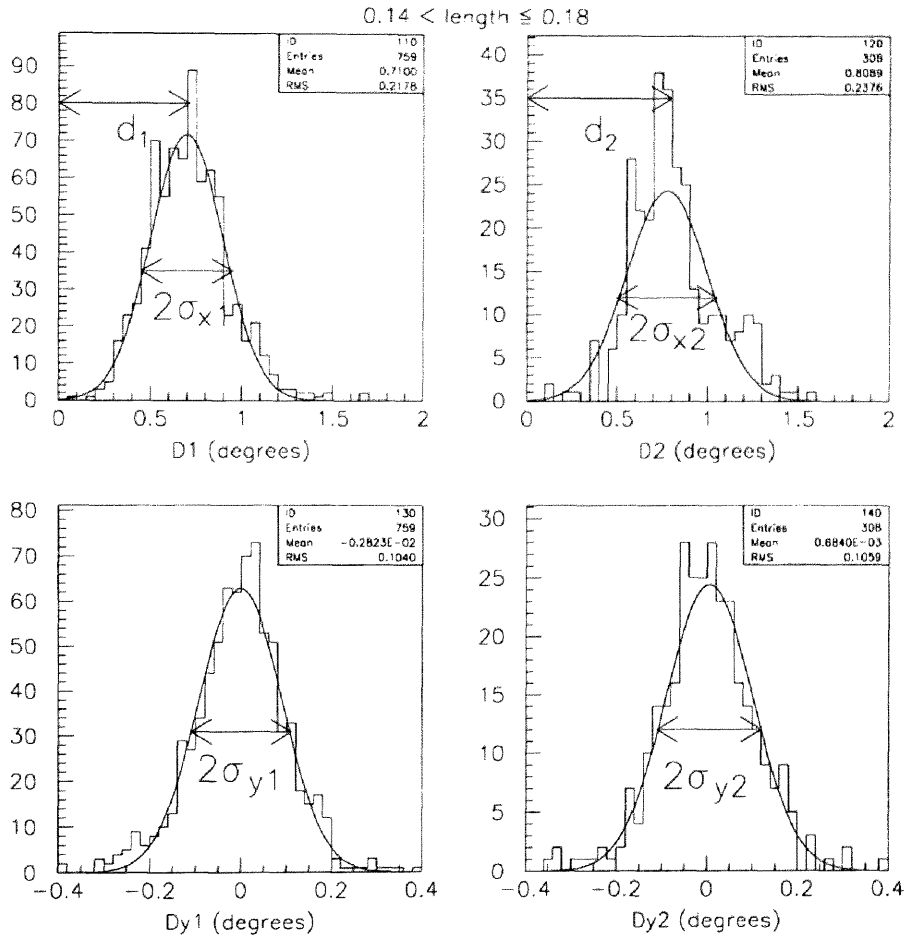

Figure 5.14: Distributions of the source distances projected on the x-axis and y-axis for the Monte Carlo gamma-ray events with $0°.14 < \textit{length} \leq 0°.18$ (as an example).

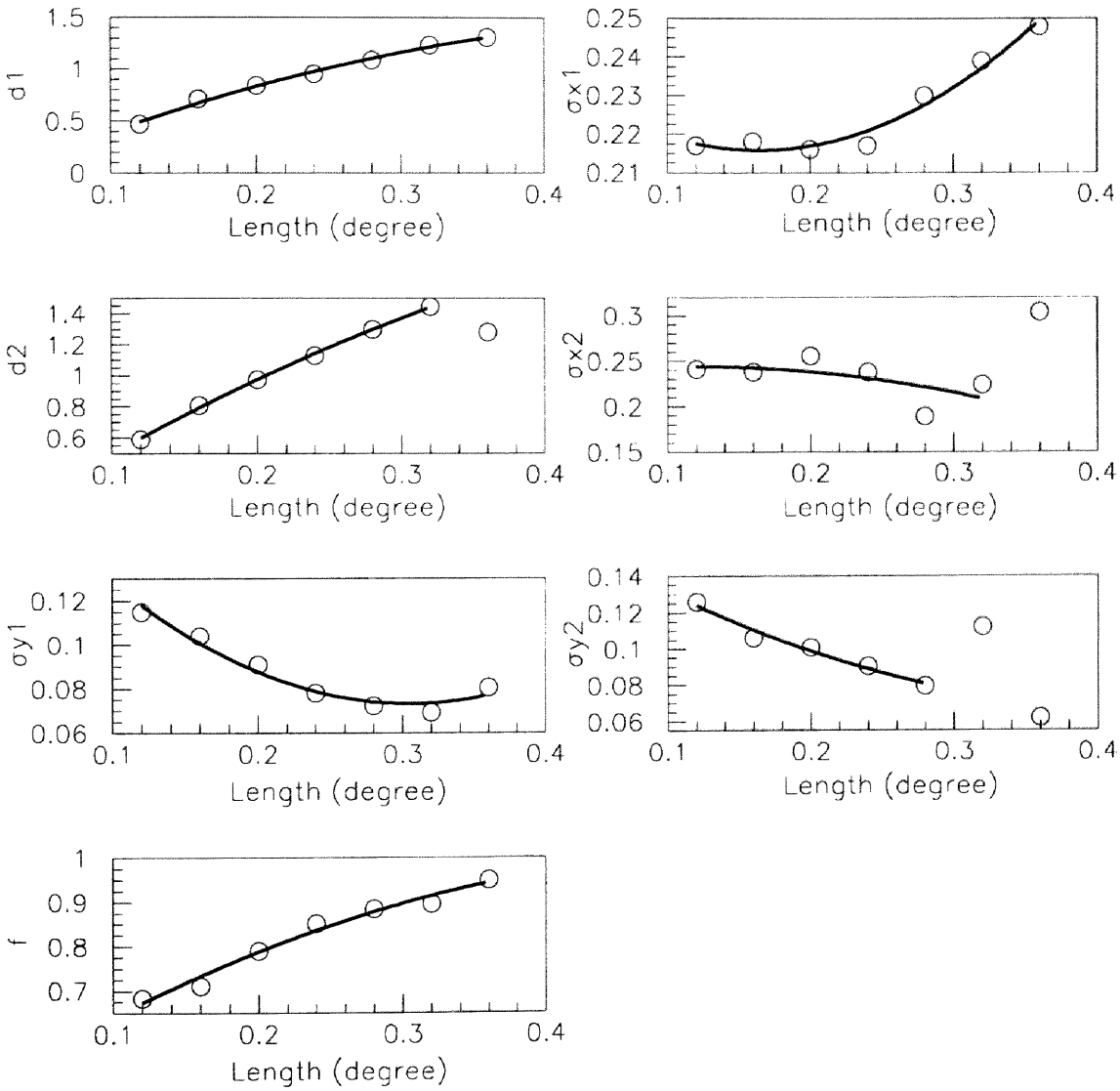

Figure 5.15: Fitting of the *SPDF* parameters as functions of the *length* parameter.

Table 5.3: Parameters of the *exteded SPDF* as functions of the *length* parameter. Values in parentheses are not used to obtain the fit curves 5.12 because the precisions in fitting were not good.

Range of length	d_1	d_2	σ_{x1}	σ_{x2}	σ_{y1}	σ_{y2}	f
$0°.10 \sim 0°.14$	$0°.466$	$0°.590$	$0°.217$	$0°.241$	$0°.115$	$0°.126$	0.683
$0°.14 \sim 0°.18$	$0°.710$	$0°.809$	$0°.218$	$0°.238$	$0°.104$	$0°.106$	0.711
$0°.18 \sim 0°.22$	$0°.840$	$0°.976$	$0°.216$	$0°.256$	$0°.0911$	$0°.101$	0.790
$0°.22 \sim 0°.26$	$0°.953$	$1°.131$	$0°.217$	$0°.238$	$0°.0781$	$0°.0906$	0.852
$0°.26 \sim 0°.30$	$1°.087$	$1°.298$	$0°.230$	$0°.189$	$0°.0723$	$0°.0796$	0.884
$0°.30 \sim 0°.34$	$1°.234$	$1°.445$	$0°.239$	$0°.224$	$0°.0694$	$(0°.112)$	0.896
$0°.34 \sim 0°.38$	$1°.311$	$(1°.282)$	$0°.248$	$(0°.304)$	$0°.0806$	$(0°.0602)$	0.950

$$
\begin{aligned}
d_2 &= -0.0609 + 5.98 \times length - 4.02 \times length^2 \\
\sigma_{x1} &= 0.240 - 0.292 \times length + 0.885 \times length^2 \\
\sigma_{x2} &= 0.232 - 0.204 \times length - 0.871 \times length^2 \\
\sigma_{y1} &= 0.195 - 0.797 \times length + 1.31 \times length^2 \\
\sigma_{y2} &= 0.175 - 0.496 \times length + 0.563 \times length^2 \\
f &= 0.452 + 2.08 \times length - 1.97 \times length^2. \qquad (5.12)
\end{aligned}
$$

The functions of the *SPDF parameters* are substituted for the *constant SPDF parameters* in Equation (5.6).

The significance map calculated using the *extended SPDF* is shown in Figure 5.16. As in the case of the *original SPDF*, the significance decreases compared with the result obtained from the *standard* method analysis. However, the peak position has shifted from those obtained in the previous two analysis methods towards the pulsar position.

5.5 Periodicity Analysis

For the events selected with Criteria (5.4) and $alpha \leq 10°$, a periodicity of the event times modulated with the pulsar period is examined. The recorded arrival time of each event was corrected to the Solar System Barycenter (SSBC) arrival time using the solar system ephemeris based on epoch 2000 (DE200) [62]. This time was then used to calculate the pulsar phase using

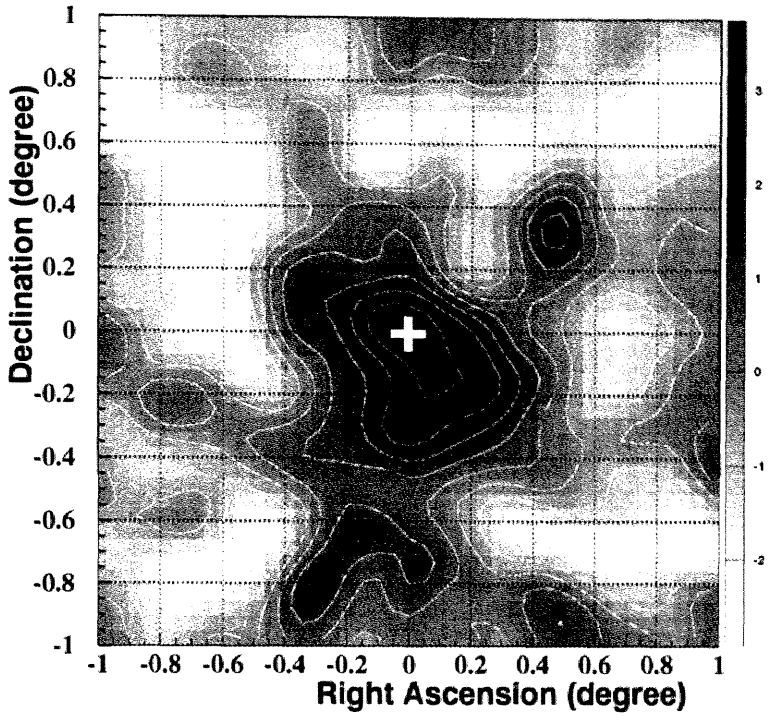

Figure 5.16: Statistical significance map of the 1997 data obtained from the *extended SPDF* method The inner-most coutour has a significance of 3.0σ. At the pulsar position, the significance is 3.7σ, which is the maximum significance in the map.

the standard formula,

$$\phi(t) = \phi_0 + \nu_0(t - t_0) + \frac{1}{2}\dot{\nu}_0(t - t_0)^2 + \frac{1}{6}\ddot{\nu}_0(t - t_0)^3. \tag{5.13}$$

Here $\nu_0, \dot{\nu}_0$ and $\ddot{\nu}_0$ are the pulsar frequency and its first and second derivatives defined at the epoch t_0 and t is the SSBC arrival time of the event. We used for t_0, ν_0, $\dot{\nu}_0$ and $\ddot{\nu}_0$ the values obtained from the Princeton University data base on radio pulsar timing solutions [31]. The values used in the present analysis are listed in Table 5.5. As mentioned in Section 4.4.2, during the observations of 1997, information from the GPS time was not available. Although the absolute times were not obtained in these periods, the relative time between events is accurate enough to carry out periodicity analysis for each observation period (March, April and May in this case). Therefore, the results of 1997 are divided into 3 separate observational periods. The resultant phase histograms are shown in Figure 5.17. No apparent periodicity is found in any of these histograms. Statistical arguments are presented in Section 6.2.3.

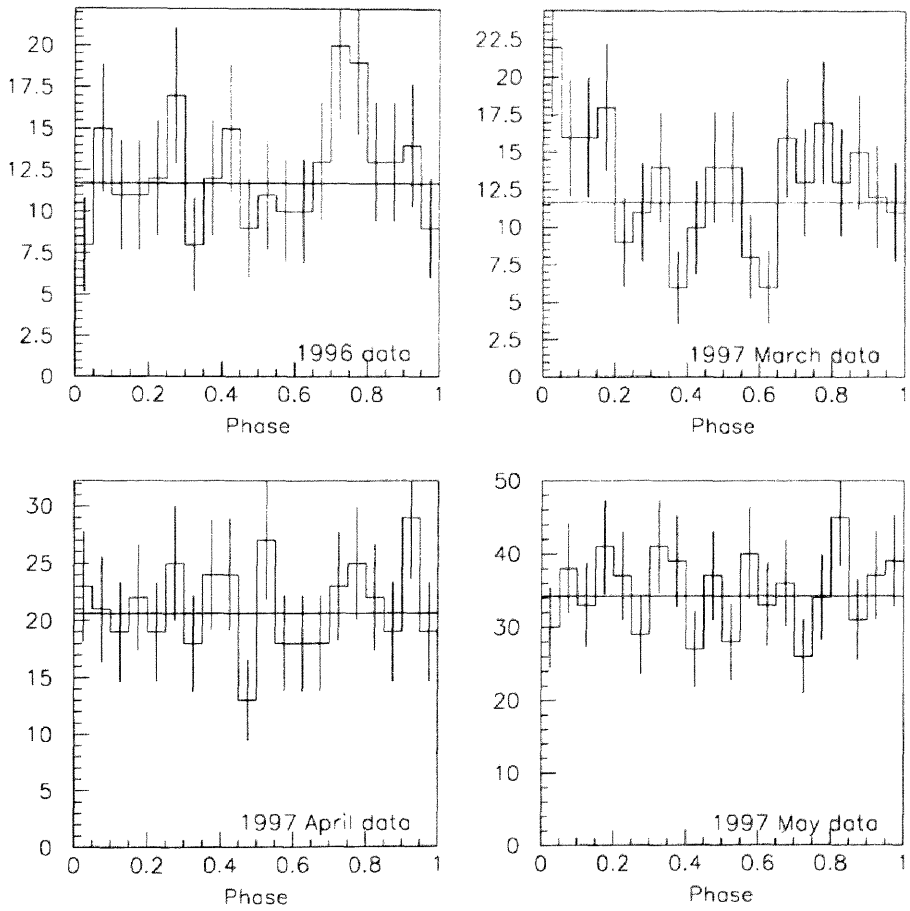

Figure 5.17: Phase histograms of the event arrival times. The 1997 data are divided into 3 observational periods because of the clock problem (see the text for details).

Table 5.4: Parameters used in the period analysis.

MJD1	MJD2	MJD(t_0)	ν_0 (s^{-1})	$\dot{\nu}_0$ ($\times 10^{-11} s^{-2}$)	$\ddot{\nu}_0$ ($\times 10^{-21} s^{-3}$)
50114	50296	50205.000000764	6.6267743270631	-6.73824	1.95
50242	50462	50352.000000582	6.6259186740744	-6.73579	1.95

MJD1 : First date of the period used to obtain parameters
MJD2 : Last date of the period used to obtain parameters
MJD(t_0) : Geocentric arrival time of the pulse with infinite frequency
ν_0 : Pulsar rotation frequency
$\dot{\nu}_0$: First derivative of pulsar frequency
$\ddot{\nu}_0$: Second derivative of pulsar frequency

Chapter 6

Discussion

Results obtained in Chapter 5 are discussed in greater detail in this Chapter. First, some statistical arguments touched upon in Chapter 5 are described. Because the positive results are obtained in the data taken in a relatively short observation time (32^h), a careful consideration of statistics is important for assessing the significance of the limited information. Following those statistical tests, physical values of the results from the source are deduced.

6.1 Statistical Arguments

6.1.1 Result of the Asymmetry Parameter

In the 1997 data, an excess of the *asymmetry* parameter was found in the positive value. Although it indicates a tendency of VHE gamma-rays, the excess was not as strong as expected from a Monte Carlo calculation. The ON – OFF distribution of the *asymmetry* parameter is compared with the distribution obtained for the Monte Carlo gamma-ray images, which are selected with Criteria (5.4) and $alpha \leq 10°$. This Monte Carlo distribution is noted "gamma-ray hypothesis". At the same time, a comparison with the Monte Carlo proton images should be carried out. However, to obtain enough amount of the Monte Carlo proton images, which survive all the image cuts, one has to spend a large computation time. Therefore, the observational distribution of the OFF source run is assumed as a distribution of "no source hypothesis".

The total number of events in the distributions of the two hypotheses are normalized to the observed total number of events in the ON–OFF distribution. χ^2 for the two hypotheses

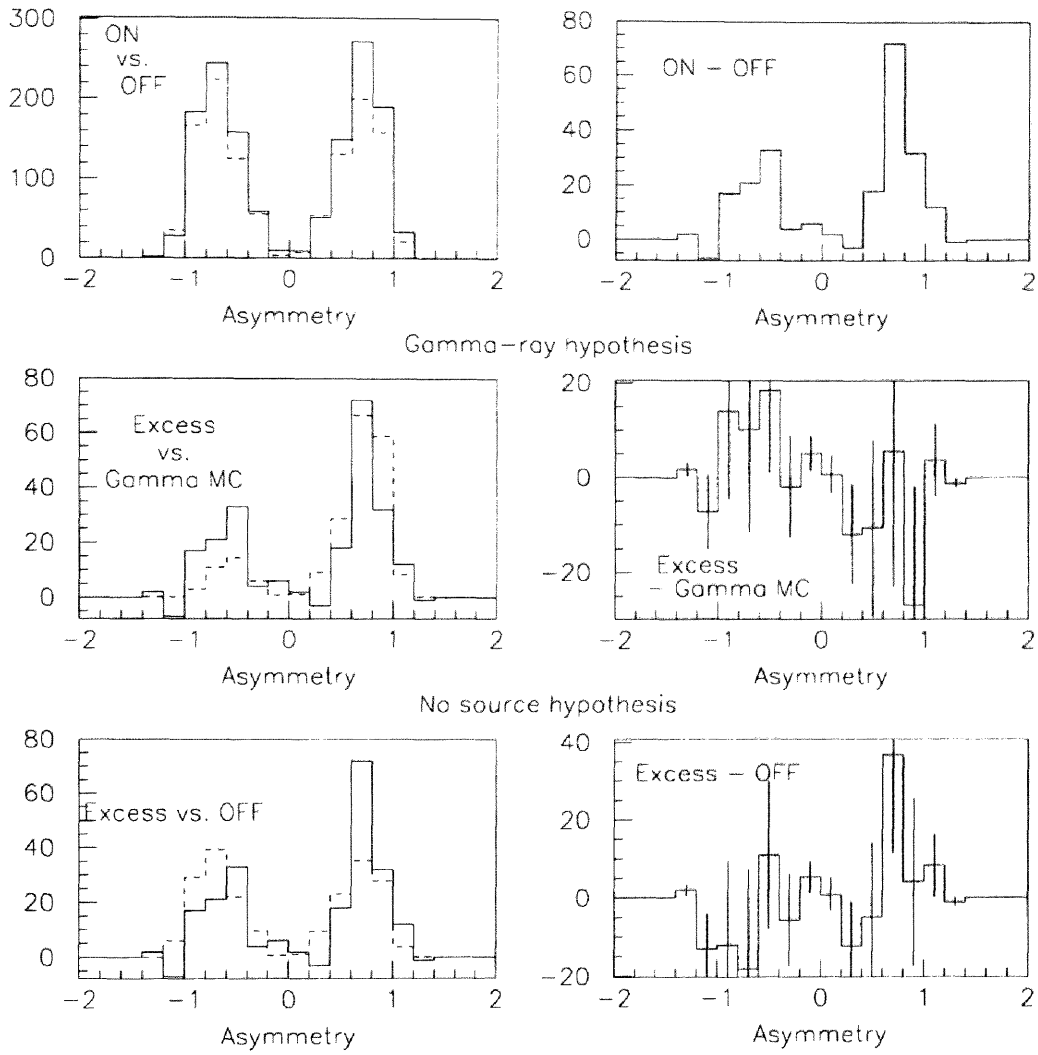

Figure 6.1: χ^2 tests for the *asymmetry* distribution obtained from the 1997 data. Two hypotheses, *gamma-ray hypothesis* and *no source hypothesis*, are examined.

are calculated to be, χ^2=10.8 (for the "gamma-ray hypothesis") and χ^2=11.8 (for the "no source hypothesis") with 14 degrees of freedom. This χ^2 test, then, admits both the hypotheses (Figure 6.1).

6.1.2 Source Localization Error

The precision of the source localization in the *standard* method analysis applied in Section 5.3 depends on the individual case, *i.e.*, the number of the events of the ON source and the OFF source. To estimate this error, a large amount of the imaginary source search should be carried out using Monte Carlo calculations. In order to save the time of the Monte Carlo calculations,

some simplified assumptions are applied.

For the background events, imaginary images are assumed to have only two characteristics, the position and the direction of the axis. Because they represent uniform and isotropic hadronic background, the positions and the directions of the imaginary images are randomly distributed in the ranges of $distance1 \leq 1°.05$ and $0° \leq alpha < 90°$ with respect to the camera center. The number of background events distributed for both the imaginary ON and OFF source data is 15925. This number is the actual count of the OFF source data after *shape* cuts and *distance1* cut. These cuts do not affect the determination of the source position. In the actual calculations, the number of the background events was fluctuated according to a Gaussian distribution out to $\pm 3\sigma$ with respect to the mean number.

The imaginary gamma-ray events also have the same characteristics. However, the distribution of these two parameters are not uniform and isotropic. Assuming a gamma-ray source is at the pulsar position, a density function was determined using Monte Carlo images of gamma-rays. This function shows an event density as a function of the *distance1* and the *alpha*. Imaginary gamma-ray images are distributed following this function to make 208 excess counts at $alpha \leq 10°$ at the pulsar position. The excess count 208 is also the observed number of ON – OFF events at the pulsar position. An imaginary ON source data is obtained by adding these gamma-ray images on the previously obtained background events.

For each pair of the imaginary ON and OFF source data, the *standard* source search is carried out. A total number of 100 source searches were carried out with these data. In each trial, the position having the maximum significance is recorded. Naturally, the pulsar position, which is the gamma-ray source in this test, has the maximum significance most often. The two dimensional histogram of the maximum significance positions is shown in Figure 6.2. To examine the lateral extension in Figure 6.2, the total number of the trials included in a radius r from the pulsar position is calculated. The result is listed in Table 6.1. If the source localization error is defined as a 1 σ circle, which includes 68 % of the trials within the area, it becomes $\simeq 0°.10$. The observational significance map obtained in Section 5.3 is again shown in Figure 6.3 along with the source localization error circles obtained here.

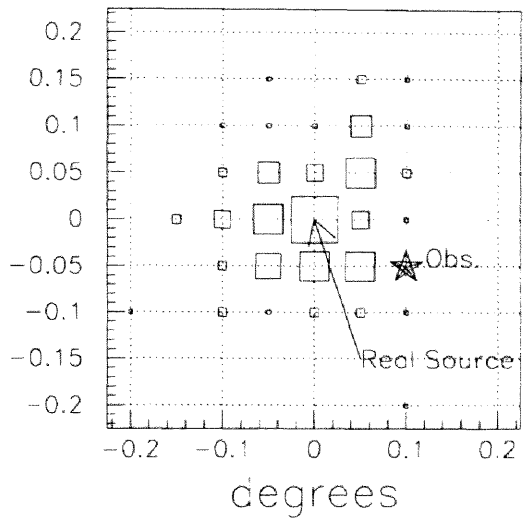

Figure 6.2: Test of the source localization error. In the Monte Carlo calculaions, gamma-ray source is located at the center of the field of view. Histogram shows the number of the trials, which have the maximum excess at the position. Our result obtained from the 1997 data is indicated by the star mark.

As a result of this study, the gamma-ray source position obtained in this thesis is consistent with the pulsar position. Because significant pulsations were not found in our data, the emission is probably from the compact synchrotron nebula around the pulsar.

6.1.3 Correct Significance in the Source Search

In the significance map shown in Figure 6.3, the maximum significance, 4.9 σ, is found at the position consistent with the pulsar nebula. However, in this significance value, the degrees of freedom for the source search are not considered. To include this effect and obtain a more correct significance value, Monte Carlo calculations are again used. In this case, the fluctuation of the significance value is examined with no gamma-ray source assumption. The observational 4.9 σ should be compared with this fluctuation.

Following the same method described in the previous section, many pairs of imaginary data are made. Here, both the imaginary data correspond to OFF source data. For each pair of the OFF sources, a significance map is calculated. The maximum significance in the $2^\circ \times 2^\circ$ field is again recorded for each trial. A total number of 1088 source searches were carried out with these data. The distribution of the maximum significance values is shown in Figure 6.4. This result gives the probability of a 4.9 σ excess appearing by chance in the field. Because the

Table 6.1: Source localization error. N(≤r) is the number of trials, which resulted the maximum significance within a radius r from the pulsar. A total number of 100 trials are examined.

r	N(≤r)
0°.00	11
0°.05	33
0°.07	58
0°.10	66
0°.11	81
0°.14	86
0°.15	91
0°.18	92
0°.20	94

mean and standard deviation of the distribution in Figure 6.4 are 2.96 and 0.49, respectively, 4.90 σ can be converted into $(4.90 - 2.96)/0.49 = 3.96\sigma$ as a maximum significance in the field. This is the strictest (pessimistic) estimate of the maximum significance.

The fact that the maximum significance is found near the error circle of the source candidate must be considered in the estimation. The probability that the maximum significance accidentally appears within 0°.50 from the pulsar position is 0.17. (For much narrower region, the number of Monte Carlo trial is not sufficient.) In this narrow region, the distribution of the maximum significance value has the mean of 2.96 and the standard deviation of 0.49 (Figure 6.5). Because these values are same with the previous case, the 4.9 σ excess is decreased into 3.96 σ. Combining the probability of 0.17 and 3.96 σ, the resultant significance is obtained to be 4.3 σ. For a much narrower region, the significance should become a larger value.

Finally, considering all the results described above, it is concluded that an excess of the VHE gamma-ray signal is obtained from the position consistent with the pulsar nebula position with a significance of more than 4.3 σ.

6.1.4 The Precision of the SPDF

Two kinds of the *SPDF* are introduced in Chapter 5 for precise localizations of the source. Since these functions reflect the nature of the EASs more than the *standard* method, the precisions of the source localization will be better than 0°.10 in this case. For the detailed

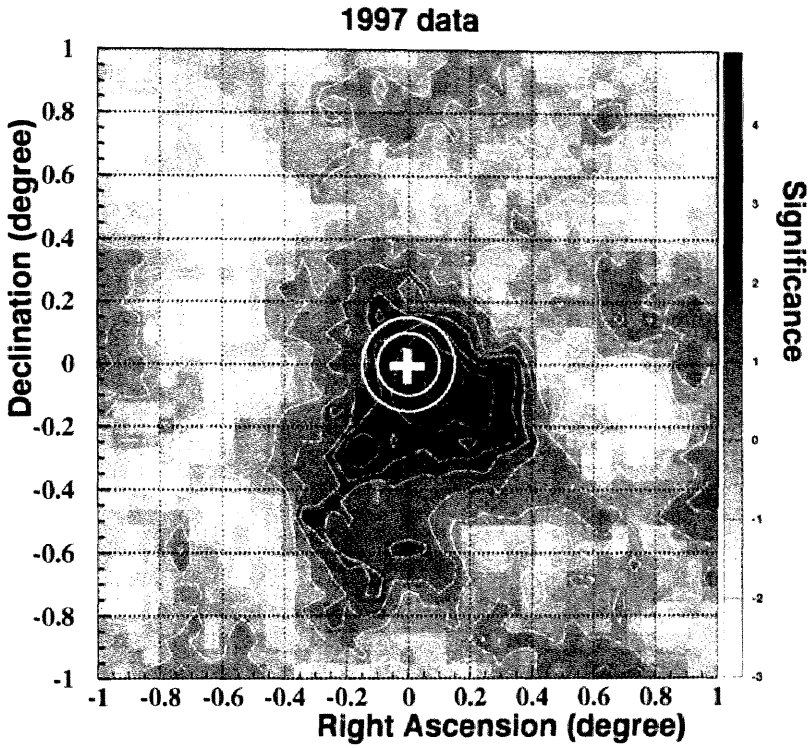

Figure 6.3: Statistical significance map of the 1997 data with the source localization error circles (66% and 91%).

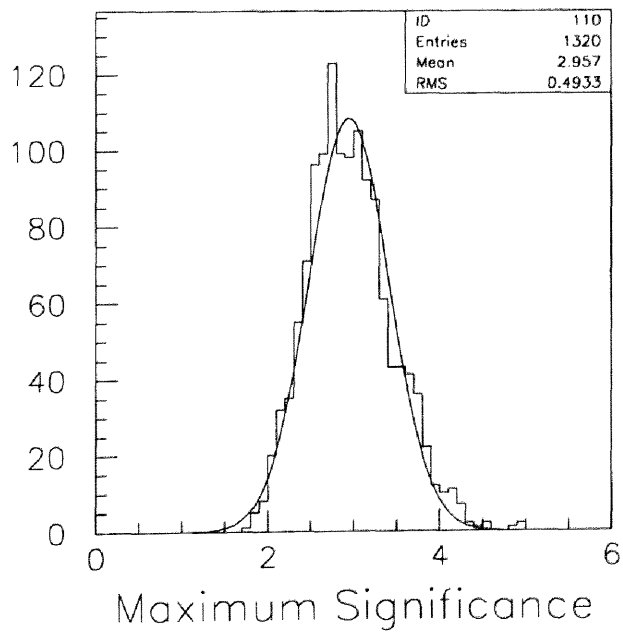

Figure 6.4: Distribution of the maximum significance in the 2° × 2° field of view with "no source assumption."

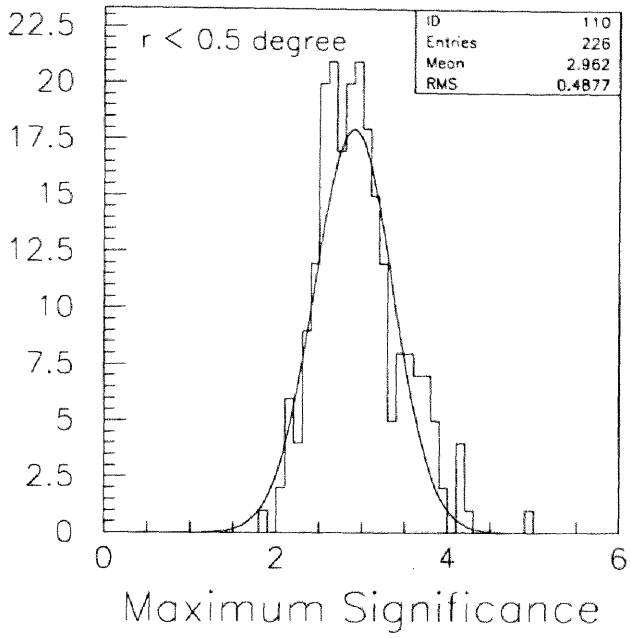

Figure 6.5: Distribution of the maximum significance at the *distance* $< 0°.50$ with "no source assumption."

estimation, full Monte Carlo calculations or much sophisticated modeling are needed. Due to the limited computation power and time, such estimations cannot be carried out here at the present time.

Another way for estimating the localization error is to use an obvious point source like AGNs. Unfortunately, the *CANGAROO* has not found any AGN as yet.

6.2 Physical Arguments relating to the Source

According to the arguments in the previous section, we proceed, hereafter, taking the position that the gamma-ray emission *is* from the synchrotron nebula around the pulsar.

6.2.1 Flux and Upper Limit

In order to calculate the flux of VHE gamma-rays from the 1997 result and the upper limit to the flux from the 1996 result, the effective collection areas are deduced using Monte Carlo calculations. The effective areas for the two years as functions of the primary gamma-ray energy are shown in Figure 6.6. The effects of the event selections in the analysis are included

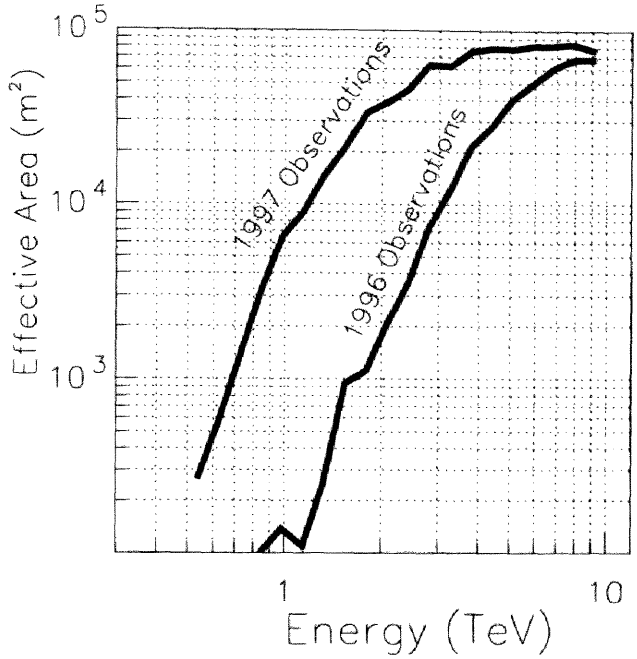

Figure 6.6: Effective areas of the observations in 1996 and 1997. All the cuts are adopted to Monte Carlo events to obtain these functions.

in calculating these areas. If the differential spectrum of the gamma-ray is represented as $dF(E)/dE$, the expected excess counts (ON - OFF), ΔN, is expressed as,

$$\Delta N = T \int_0^\infty \frac{dF(E)}{dE} S(E)\, dE\ . \tag{6.1}$$

Here, T is the observation time and S(E) is the effective area as a function of the primary energy shown in Figure 6.6. For the 1997 data, $\Delta N = 208$, $T = 115680^s$ and a single power law with a differential spectral index of -2.5 are used. The excess number of counts is that obtained at the pulsar position. The integral flux $F(E > E_{thresh})$ is calculated to be,

$$F(E > E_{thresh}) = (3.1 \pm 0.8) \times 10^{-12} cm^{-2} s^{-1} \quad ; E_{thresh} = (1.5 \pm 0.5)\ TeV\ . \tag{6.2}$$

The estimation of the threshold energy (E_{thresh}) is described below. The error is 1 σ of the excess counts obtained from the raw counts of the ON and OFF source data, N_{ON}=1388 and N_{OFF}=1180.

In the 1996 data, N_{ON}=248, N_{OFF}=246 and the normalization factor is $k = 0.961$. The observation time of the ON source is $T = 145920^s$. Supposing there is a detectable gamma-ray signal, which causes an excess ΔN above the normalized background kN_{OFF}, but due to the fluctuation it decreased to the observed counts N_{ON}. If this is a 3 σ fluctuation, the following equation is obtained.

$$\frac{(kN_{OFF} + \Delta N) - N_{ON}}{d(kN_{OFF} + \Delta N - N_{ON})} = 3 \tag{6.3}$$

Here,

$$d(kN_{OFF} + \Delta N - N_{ON}) = \sqrt{k^2 N_{OFF} + \Delta N + N_{ON}} \tag{6.4}$$

From the equations above, ΔN=82 and the corresponding flux, which is regarded as the 3 σ upper limit, becomes,

$$F_{3\sigma}(E > E_{thres}) < 2.0 \times 10^{-12} cm^{-2} s^{-1} \quad ; \; E_{thresh} = (4.0 \pm 1.3)\; TeV\;. \tag{6.5}$$

The threshold energy is defined as the energy at which the *detected* (or potentially *detectable*) photon flux becomes maximum. To obtain the spectrum of the *detected* (*detectable*) photons, the effective area $S(E)$ is multiplied the differential flux $dF(E)/dE$. The resultant spectra are shown in Figure 6.7 for the 1996 and 1997 observations. The peaks are found at the energies of 4.0 TeV and 1.5 TeV, respectively. These values of the threshold energy are sensitive to the assumed value of the spectral index of the primary gamma-ray. A range of indices, -2.5 ± 1.0 are examined (see Figure 6.8 for the 1997 observations) and the corresponding variations are regarded as errors in the threshold energies. These variations correspond to $\simeq \pm 30\%$ of the threshold energy obtained with the index of -2.5.

6.2.2 Consistency between the 1996 and the 1997 Data

The excess counts of the 1997 data are plotted in Figure 6.9 as a function of the minimal threshold of the photoelectron counts for an event to be acceptable. At the same time, the

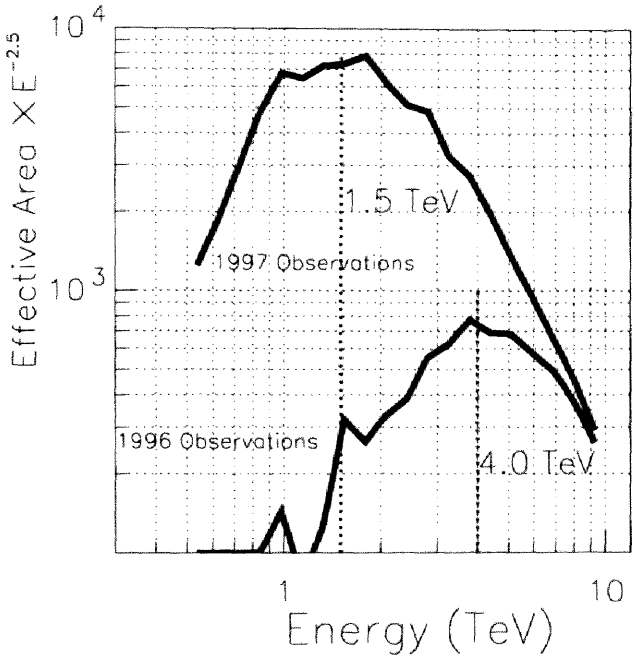

Figure 6.7: Threshold energies of the observations in 1996 and 1997. Differential index of -2.5 is assumed as a spectrum of the primary gamma-rays.

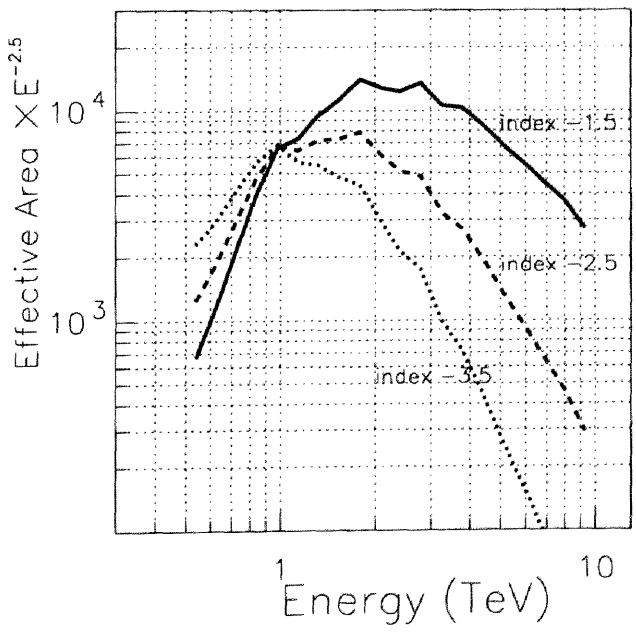

Figure 6.8: Differential indices of the primary gamma-rays are varied in the range of -1.5 and -3.5.

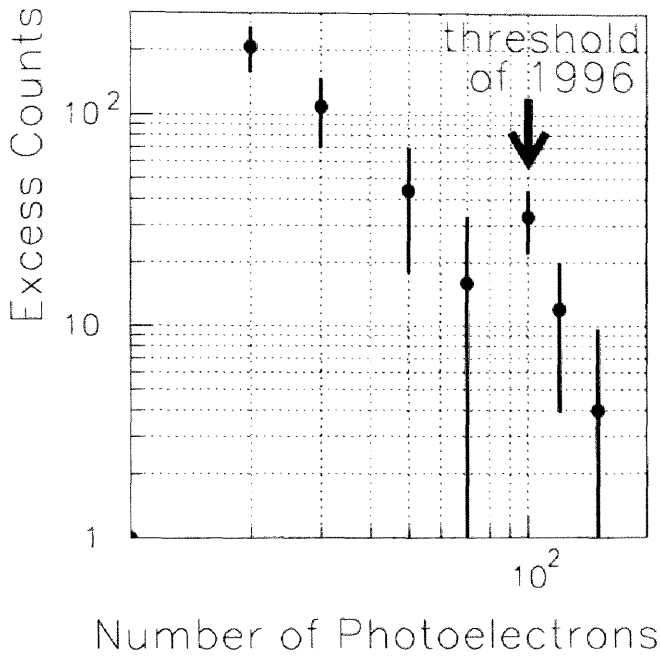

Figure 6.9: Excess counts of the 1997 data, including large number of photoelectrons. Horizontal axis shows the lower threshold of the number of photoelectrons. Arrow shows the position where the threshold energy of the 1997 data becomes 4TeV, which is the threshold energy of the 1996 observations.

threshold energies are calculated for some values of this lower threshold (Figure 6.10). As seen in Figure 6.10, the threshold energy of the 1997 data, including more than 100 photoelectrons, is $\simeq$ 4 TeV, same as the threshold energy of the 1996 observations. Although the excess with this photoelectron threshold in the 1997 data is only 3.0 σ (N_{ON}=77 and N_{OFF}=44), the corresponding flux can be calculated to be,

$$F(E > E_{thresh}) = (1.6 \pm 0.5) \times 10^{-12} cm^{-2} s^{-1} \quad ; \; E_{thresh} = (4.0 \pm 1.3) \; TeV \; . \tag{6.6}$$

This value is lower than the upper limit obtained from the 1996 data. Moreover, as imagined from Figure 6.9, the excess counts at this photoelectron threshold in the 1997 data may be an overestimate of the expected excess counts.

From the arguments above, two independent measurements of the flux from the 1997 data at $E > 4.0$ TeV and the upper limit from the 1996 data at the same energy are consistent with each other.

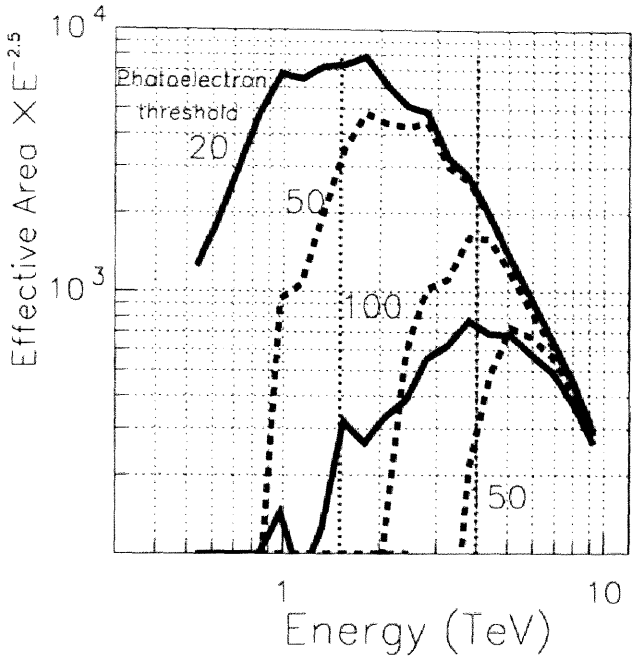

Figure 6.10: Threshold energies of the 1997 data as a function of the lower limit of photoelectron counts. The data, having more than 100 photoelectrons, have a threshold energy of 4TeV, which is the threshold energy of the 1996 data.

6.2.3 Limits for the Pulsed Flux

To the apparently uniform distributions of the light curves shown in Figure 5.17, statistical tests are applied and the upper limits are calculated. The χ^2 test, the Z_2^2 test [6] and the H-test [26] are applied to the phase distribution of events to calculate the chance probabilities for a uniform distribution (*i.e.* null hypothesis). The results are summarized in Table 6.2.

Table 6.2: Results of period analysis. χ^2 are obtained for the histograms with 20 bins.

Observation		Z_2^2 test		H-test		flux upper limit (3σ)
Period	χ^2	Z	P(>Z)	H	P(>H)	($\times 10^{-12} cm^{-2} s^{-1}$)
1996	17.0	3.18	0.53	3.18	0.28	1.6
March 1997	31.4	6.65	0.16	6.28	0.08	6.4
April 1997	14.1	1.43	0.83	0.65	0.77	3.3
May 1997	16.2	0.90	0.92	0.71	0.75	2.6

Again, no evidence for the periodicity is found either in the 1996 data or any of the 3 seasons of the 1997 data, as can be seen in Table 6.2. To calculate the flux upper limit for the pulsation,

a formula given by de Jager [28] is used. In the calculation, the duty cycle of the pulse (δ) was assumed to be 0.3 using the X-ray observation by Ulmer *et al.* [77] (Figure 3.8). The 3σ upper limits for the pulsed VHE gamma-ray emission are also shown in Table 6.2.

6.2.4 Magnetic Field Strength in the Nebula

The flux from the 1997 data and the upper limit from the 1996 data are shown in Figure 6.11 along with the prediction of du Plessis *et al.*[47]. From a comparison of our results with the predicted fluxes, the magnetic field strength in the pulsar nebula is constrained to be $5 \sim 6\mu G$. This prediction is based on the simple estimation argued in Section 3.3.

In the equation,

$$\frac{P_{iC}}{P_{sync}} = \frac{U_{soft}}{U_B} , \tag{6.7}$$

P_{iC}/P_{sync} can be equated to I_{iC}/I_{sync}, if the emissions are isotropic, here I is energy flux received at the Earth in units of ergs $cm^{-2}s^{-1}$. $I_{iC} = 0.72 \times 10^{-11}$ ergs $cm^{-2}s^{-1}$ is obtained from our 1997 result assuming all the detected gamma-rays in the present result have the same energy of 1.5 TeV. When the *ROSAT* result is taken to obtain the I_{sync} value, $I_{sync} = 7.2 \times 10^{-11}$ ergs $cm^{-2}s^{-1}$ [76]. If, on the other hand, one assumes that the target photons for inverse Compton scattering are only the 2.7K Microwave Background Radiation (MBR), then $U_{soft} = U_{2.7K} = 3.8 \times 10^{-13}$ ergs cm^{-3}. Using this value in Equation (6.7), the magnetic field strength is deduced to be $B \simeq 10\mu G$. Because this argument based on energy fluxes incident on the Earth could involve an uncertainty about a factor of $\simeq 2$, the detailed calculation of du Plessis *et al.* [47] and the simple estimation made here are consistent with each other.

These value agree well with the equipartition value of the magnetic field $B \simeq 7\mu G$, estimated by Seward *et al.* [59].

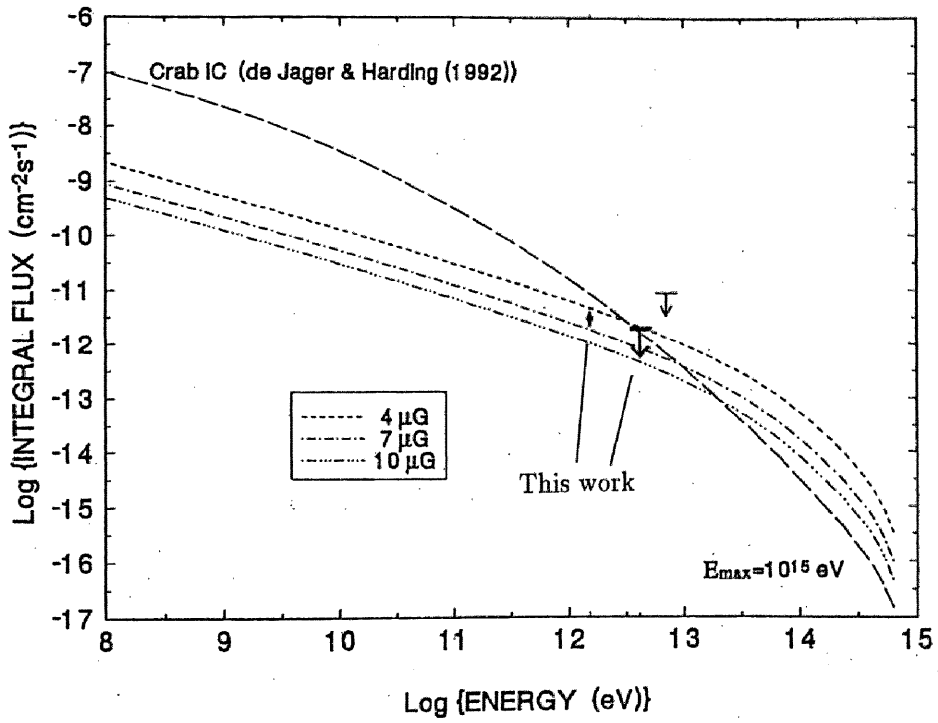

Figure 6.11: Results obtained in this thesis are plotted on the predicted spectrum of du Plessis *et al.* [47].

Chapter 7

Conclusions

After numerous studies of VHE gamma-ray emission from the *EGRET* pulsars, it is now recognized that VHE gamma-rays are emitted not from the pulsar magnetosphere but the pulsar nebula surrounding the pulsar. It led us (the *CANGAROO* collaboration) to observe a synchrotron nebula driven by a young spin-powered pulsar. PSR B1509-58 and its surrounding nebula appeared to be the best candidates to examine this new criterion for VHE gamma-ray source search.

Evidence of VHE gamma-ray emission from the direction of the PSR B1509-58 is found at 4.10 σ from the observations of 1997. The integral photon flux is obtained to be,

$$F(E > E_{thresh}) = (3.1 \pm 0.8) \times 10^{-12} cm^{-2} s^{-1} \quad ; E_{thresh} = (1.5 \pm 0.5)\ TeV \qquad (7.1)$$

with an assumption of the power law index of -2.5. The error of the threshold energy is based on the possible range of the power law index of -1.5 to -3.5. Although the *asymmetry* parameter analysis supports the tendency of the gamma-ray signal, the χ^2 tests permit both the hypotheses of gamma-ray signal and hadron background.

Since the threshold energy in the 1996 observations was higher than that in 1997, only an upper limit (3σ) is obtained from the 1996 data. This upper limit is,

$$F_{3\sigma}(E > E_{thresh}) < 2.0 \times 10^{-12} cm^{-2} s^{-1} \quad ; E_{thresh} = (4.0 \pm 1.3)\ TeV.$$

A subset of the 1997 data, with a larger threshold of number of photoelectrons, are selected. When the subset is chosen to have the same threshold energy as that of the 1996 observations

(> 100 photoelectrons), the flux corresponding to the small excess in the 1997 data is found to be lower than the upper limit (from the 1996 data). It proves the consistency between the two independent observations in the years 1996 and 1997.

A source position search is carried out in the 2° × 2° field of view around the pulsar. The resulting position of the maximum significance is 0°.11 shifted towards south-west from the pulsar position. However, using Monte Carlo calculations the source localization error is estimated for this particular case to be 0°.10 at 1 σ. The emission position is concluded to be consistent with the pulsar position. The maximum significance of 4.9 σ is obtained using a conventional formula. If the degrees of freedom in the source search are considered, this value is reduced to be 4.0 σ with a pessimistic estimation. Taking the fact that the maximum significance is found near the error circle of the candidate into account, the significance is raised to a value of more than 4.3 σ.

The *Source Probability Density Function* and its extended form are examined for a more precise source localization. Although the *original SPDF* showed almost same result with the *standard* method, the *extended SPDF* resulted in the maximum significance at the pulsar position. However, the precision of this new method is not estimated due to lack of huge computing power and time. The precision should be examined for a definite point source like AGNs in future studies.

No significant pulsation modulated with the pulsar period (P=150 ms) was found in both the 1996 and 1997 data. This fact and the result that the emission position is consistent with the pulsar (*i.e.* the south nebula) position lead to the conclusion that the VHE gamma-rays are probably emitted from the synchrotron nebula around the pulsar.

From a comparison of the present results with the predictions of du Plessis et al. [47], the magnetic field strength in the synchrotron nebula, $B = 5 \sim 6\mu G$, is resulted. This value agrees well with that obtained from the equipartition between the energy of particles and the magnetic field. This independent measurement of the magnetic field strength will provide a key for the studies of the pulsar wind and the evolution problem of the PSR B1509-58/MSH15-52 complex.

The work presented in this thesis is the first evidence of VHE gamma-ray emission from

the direction of a non-*EGRET* pulsar. This result has proved the importance of hard X-ray information for the future VHE gamma-ray seaches. The *ASCA* satellite has revealed 11 synchrotron nebulae associated with the pulsars using its high sensitivity in the energy range at 2 – 10 keV. Recently, the *ASCA* has also discovered two new pulsars in the non-thermal nebulae [75]. These newly discovered non-thermal X-ray sources are possible candidates of VHE gamma-ray source as was the case with PSR B1509-58. At the same time, VHE gamma-ray observations are indispensable to understand the nature of pulsar nebulae, which are certainly a class of giant accelerators operating in the universe.

Chapter 8

Future Observations

Now it has become clear that synchrotron radiation and inverse Compton scattering are important mechanisms when non-thermal emission from a pulsar nebula is considered. Luminosities emitted through the two mechnisims are ralated by a simple formula (3.9).

$$\eta = \frac{P_{iC}}{P_{sync}} = \frac{U_{soft}}{U_B} \,. \tag{3.9}$$

The η value in formula (3.9) signifies not only the ratio of the luminosities but also the ratio of the energy densities of low energy photon and magnetic fields. It is one of the important parameters to understand a nebula environment. The X-ray luminosities of the various pulsar nebulae observed in the *ASCA*'s energy band are summarized in Table 8.1 [60] [14].

Table 8.1: X-ray luminosities of pulsar nebulae measured in the *ASCA*'s energy band.

Pulsar Name	log(L_X) log(erg s^{-1})	d (kpc)	log(Age) log(year)
Crab	37.18	2.0	3.10
Vela	>33.43	0.50	4.05
Geminga	30.63	0.15	5.53
PSR B1706-44	32.82	1.8	4.24
PSR B1509-58	35.35	4.2	3.19
PSR B1951+32	33.81	2.5	5.03
PSR B1055-52	32.56	1.5	5.72
PSR B1046-58	32.90	2.9	4.31
PSR B1929+10	30.45	0.17	6.49
PSR B0656+14	30.64	0.76	5.04
PSR B1853+01	33.52	3.3	4.30
PSR B1610-50	34.41	7.2	3.87

The luminosities measured in the X-ray energy band and the observed VHE gamma-ray luminosities or the upper limits are plotted in Figure 8.1. The values for gamma-ray luminosities or upper limits from observations having the threshold energies at a few TeV, *i.e.* Vela [84], PSR B1706-44 [34], PSR B1509-58 and PSR B1055-52 [63], are taken from the respective references. In the cases of Crab, Geminga and PSR B1951+32, which were observed with conditions having the threshold energies different from a few TeV, the gamma-ray luminosities are converted to correspond to the energy above 1.5 TeV. For Geminga [1] and PSR B1951+32 [61], the photon index is assumed to be -2.5 in the conversion. For the Crab nebula, the spectrum (index=-2.53) given by Tanimori *et al.* [67] is used.

The four flux values and the three upper limits shown in Figure 8.1 indicate that η lies in the range 10^{-2} to 10. Difference in the η values is large even among the four detected VHE sources. It means that the pulsar nebula has a variety of environments in individual sources. At the same time, the number of the sources is obviously too small to make a general discussion on nebula environment. Figure 8.1 already compares the X-ray luminosities with the observed VHE gamma-ray luminosities (or upper limits) in the case of the top 7 X-ray pulsar nebulae listed in Table 8.1. What about the remaining (bottom 5) X-ray pulsar nebulae listed in Table 8.1? Can the future VHE gamma-ray observations of these objects throw any light on those X-ray pulsar nebulae? Two values are assumed to consider this problem. One is that the spectral index in the VHE gamma-ray energy range is -2.5. The other is that the sensitivity of an Imaging Air Čerenkov Telescope is 1.0×10^{-12} cm^{-2} s^{-1} above 1.5 TeV. Using the known parameters, L_X (X-ray luminosity measured in the *ASCA*'s energy band) and r (distance between the assosiated radio pulsar and the Earth), the lowest value of the detectable gamma-ray luminosity above 1.5 TeV can be obtained. The entire set of the X-ray nebulae listed in Table 8.1 are shown in Figure 8.2. The five new points (shown by filled circles) be in the range η=1 to 10. This, then, means that the future VHE observations of these X-ray sources can give us meaningful information about the general conditions in the nebular environment even if the VHE luminosities are only upper limits. And if the environments of these objects are similar to that of PSR B1706-44, *i.e.* $\eta \sim 10$, four of the five candidates can be easily

detected in VHE gamma-rays. There is a good case for making VHE gamma-ray observations on all the remaining five X-ray pulsar nebulae.

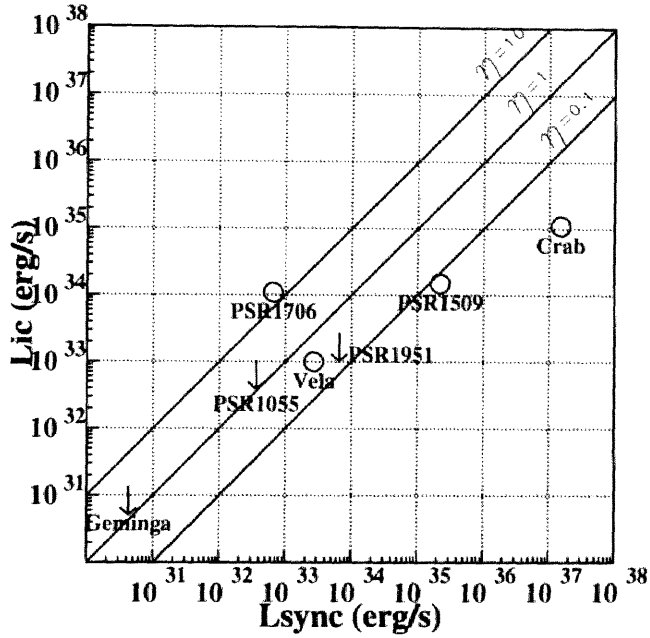

Figure 8.1: Luminosities of synchrotron and inverse Compton radiations of the pulsar nebulae, which are already observed in VHE gamma-ray.

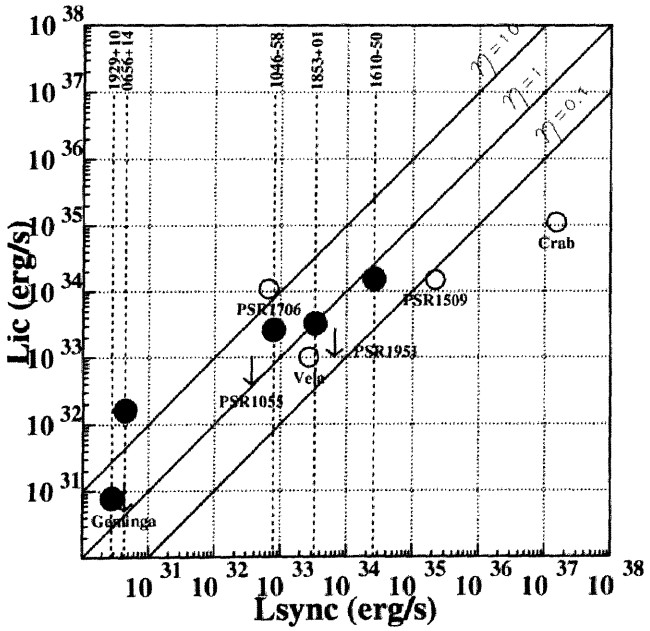

Figure 8.2: Luminosities of synchrotron and inverse Compton radiations of the pulsar nebulae. For the objects as yet unexplored in VHE gamma-rays, minimum detectable luminosities are plotted (filled circles).

Acknowledgement

I would like to thank to my supervisor, Prof. Y. Muraki for giving me a chance to study not only gamma-ray astronomy but also many other experiments and experiences. I also thank Prof. Y. Matsubara for helping and encouraging my work.

I am grateful to Prof. T. Kifune (Institute for Cosmic Ray Research, University of Tokyo) and Prof. T. Tanimori (Tokyo Institute of Technology). They gave me the opportunity to observe PSR B1509-58 and always gave me fruitful suggestions for my works. Prof. J. R. Patterson (University of Adelaide) has always helped me in the observations in Woomera. Thanks to Dr. T. Yoshikoshi for much advise on details of the analysis. I would like also thank to Prof. P. V. Ramanamurthy for a careful reading of my manuscript and for some suggestions to improve my results. In Woomera, Prof. J. R. Patterson, Prof. T. Tanimori, Prof. Y. Mizumoto, Prof. T. Yoshida, Prof. K. Nishijima, Dr. M. D. Roberts, Dr. T. Naito, Mr. S. A. Dazeley, Mr. K. Sakurazawa, Mr. H. Muraishi and Miss R. Suzuki have carried out observations with me or observed PSR B1509-58 instead of me. Thanks to their instructions and helps, I could obtain good data used in this thesis. I am also grateful to all the other CANGAROO collaborators.

My positive result in this thesis was realized due to the mirror re-coating work at the Anglo Australian Observatory. For this successful work, I thank the staff at the AAO.

I also thank the members in the cosmic ray group in the Solar-Terrestrial Environment laboratory as well as graduates, Prof. S. Shibata (Chubu University), Dr. T. Koi, Mr. T. Nishiyama, Mr. T. Yanagisawa, Mr. T. Murata, Mr. T. Matsuoka (graduate), Mr. I. Imaida, Mr. H. Tsuchiya, Mr. T. Hoshida, Miss Y. Naruse, Miss S. Noda and Mr. T. Sumi. And also to the staff in the laboratory, I express my great thanks.

Finally, when I was looking for my target to observe, I came across an interesting parer predicting VHE gamma-ray emission from PSR B1509-58. I thank the authors, du Plessis *et al.*, for encouraging my work.

Appendix A

Definitions of the Image Parameters

The definitions of the *image parameters* are presented here.

First, we define the position and the intensity of signal for the i th PMT to be $(x_i,\ y_i)$ and s_i (Figure A.1-(a)). Here, s_i is same with SIG_i^{norm} in Chapter 5. When the long axis of the ellipse of the shower image is expressed by $y = ax + b$, using the Least Square Method, a and b are obtained as,

$$a = \frac{(\sigma_{y^2} - \sigma_{x^2}) + \sqrt{(\sigma_{y^2} - \sigma_{x^2})^2 + 4\sigma_{xy}^2}}{2\sigma_{xy}} \tag{A.1}$$

$$= \frac{d + z}{2\sigma_{xy}} \tag{A.2}$$

$$b = < y > -a < x > \tag{A.3}$$

The following definitions are used in the formulae here.

$$< x > \equiv \frac{\sum s_i x_i}{\sum s_i},\ < y > \equiv \frac{\sum s_i y_i}{\sum s_i}, \tag{A.4}$$

$$< x^2 > \equiv \frac{\sum s_i x_i^2}{\sum s_i},\ < xy > \equiv \frac{\sum s_i x_i y_i}{\sum s_i},\ < y^2 > \equiv \frac{\sum s_i y_i^2}{\sum s_i}, \tag{A.5}$$

$$< x^3 > \equiv \frac{\sum s_i x_i^3}{\sum s_i},\ < x^2 y > \equiv \frac{\sum s_i x_i^2 y_i}{\sum s_i},\ < xy^2 > \equiv \frac{\sum s_i x_i y_i^2}{\sum s_i},\ < y^3 > \equiv \frac{\sum s_i y_i^3}{\sum s_i}. \tag{A.6}$$

$$\sigma_{x^2} \equiv < x^2 > - < x >^2,\ \sigma_{xy} \equiv < xy > - < x >< y >,\ \sigma_{y^2} \equiv < y^2 > - < y >^2, \tag{A.7}$$

$$\sigma_{x^3} \equiv < x^3 > -3 < x^2 >< x > +2 < x >^3,\ \sigma_{y^3} \equiv < y^3 > -3 < y^2 >< y > +2 < y >^3, \tag{A.8}$$

$$\sigma_{x^2 y} \equiv < x^2 y > -2 < xy >< x > +2 < x >^2 < y > - < x^2 >< y >, \tag{A.9}$$

$$\sigma_{xy^2} \equiv < xy^2 > -2 < xy >< y > +2 < x >< y >^2 - < x >< y^2 > . \quad \text{(A.10)}$$

$$d \equiv \sigma_{y^2} - \sigma_{x^2}, \; z \equiv \sqrt{d^2 + 4\sigma_{xy}^2}. \quad \text{(A.11)}$$

$(< x >, \; < y >)$ shows the center of the image.

The *length* and *width* parameters are defined as the second moments along the long axis and the short axis of the ellipse, respectively.

$$length = \sqrt{\frac{\sigma_{x^2} + \sigma_{y^2} + z}{2}} \quad \text{(A.12)}$$

$$width = \sqrt{\frac{\sigma_{x^2} + \sigma_{y^2} - z}{2}} \quad \text{(A.13)}$$

When the distance vector, $\boldsymbol{D}$, is defined as,

$$\boldsymbol{D} = (x_s - < x >, \; y_s - < y >) \quad \text{(A.14)}$$

the *distance* parameter is expressed as,

$$distance = |\boldsymbol{D}| = \sqrt{(x_s - < x >)^2 + (y_s - < y >)^2}. \quad \text{(A.15)}$$

Here, $(x_s, \; y_s)$ is the position of the assumed source in the field of view (Figure A.1-(b)).

Using the *miss* parameter, which is the distance from the assumed source position to the long axis, the *alpha* parameter can be defined (Figure A.1-(b)).

$$miss = \frac{|ax_s + b - y_s|}{\sqrt{a^2 + 1}} \quad \text{(A.16)}$$

$$alpha = \sin^{-1}\left(\frac{miss}{distance}\right) \quad \text{(A.17)}$$

A unit vector, $\boldsymbol{u}$, along the long axis can defined as (Figure A.1-(c)),

$$\boldsymbol{u} = \left(\sqrt{\frac{z-d}{2z}}, \; \text{sign}(\sigma_{xy})\sqrt{\frac{z+d}{2z}}\right). \quad \text{(A.18)}$$

Using the $\boldsymbol{u}$ vector, the asymmetry vector, $\boldsymbol{A}$, is defined (Figure A.1-(d)).

$$\boldsymbol{A} = -\sigma_A \boldsymbol{u} \tag{A.19}$$

Here σ_A^3 is the third moment along the long axis (x' axis in Figure A.1-(c)). When the position of the i th PMT in the x' coordinate is expressed as $(x_i',\ y_i')$, σ_A^3 is defined as,

$$\sigma_A^3 \equiv \frac{\sum s_i (x_i' - < x_i >')^3}{\sum s_i} . \tag{A.20}$$

If the angle between the x-axis and the x'-axis is defined as ϕ (Figure A.1-(c)), σ_A^3 can be rewritten to be,

$$\sigma_A^3 = \sigma_{x^3} \cos^3\phi + 3\sigma_{x^2y} \cos^2\phi \sin\phi + 3\sigma_{xy^2} \cos\phi \sin^2\phi + \sigma_{y^3} \sin^3\phi . \tag{A.21}$$

After all, the *asymmetry* parameter is defined as,

$$asymmetry = \mathrm{sign}(\boldsymbol{A} \cdot \boldsymbol{D}) \frac{|\sigma_A|}{length} . \tag{A.22}$$

Using the largest and second largest s_i (S_1 and S_2), the *concentration* parameter is defined as,

$$concentration = \frac{S_1 + S_2}{\sum s_i} . \tag{A.23}$$

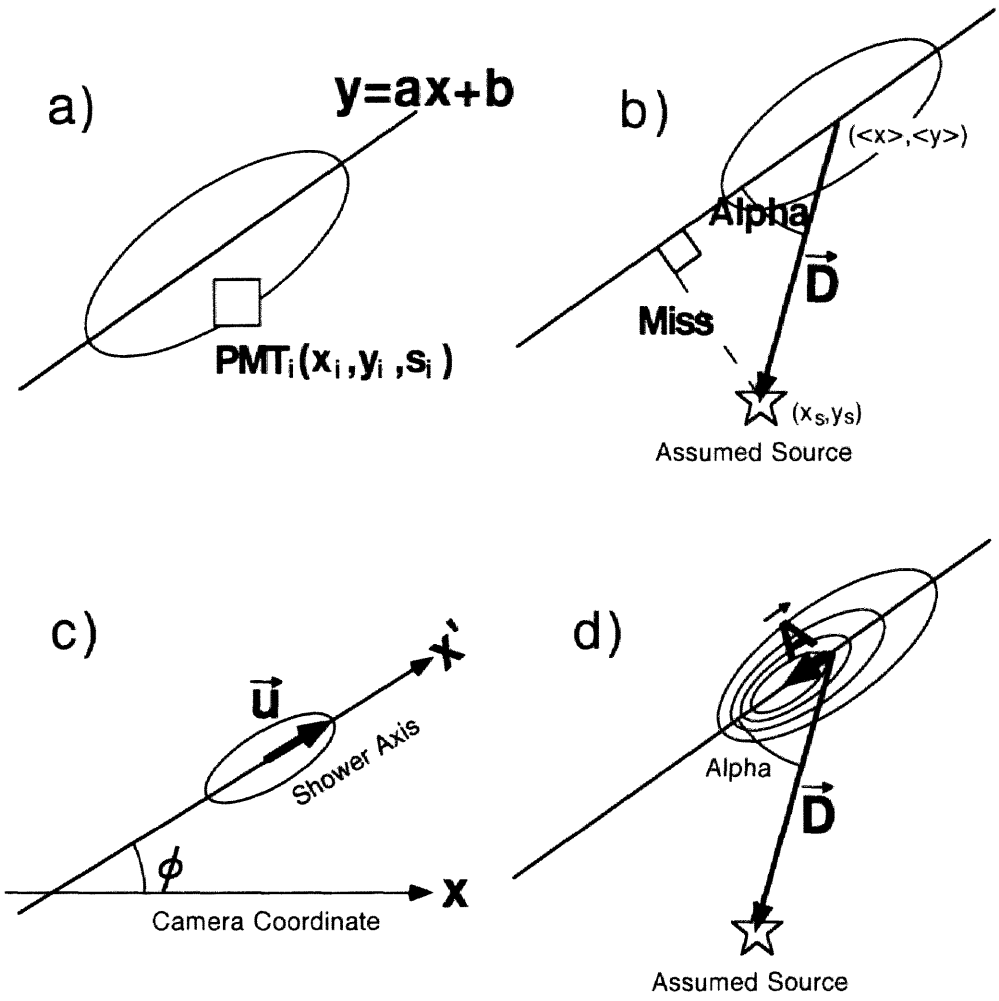

Figure A.1: Parameters used in obtaining the *image parameters*. a) The major axis of the shower image is expressed as $y = ax + b$. The position and the intensity of the signal in the i th PMT are defined as (x_i, y_i, s_i). b) The definitions of the distance vector, the *alpha* parameter and the *miss* parameter. These *orientation parameters* depend on the position of the assumed source in the field of view, (x_s, y_s). c) The definitions of the x' axis and the unit vector along the axis. d) The definition of the asymmetry vector. It shows the 3rd moment of the intensity along the x' axis and directs to the true source.

Bibliography

[1] Akerlof, C. W., *et al.*, 1993, *Proc. 23rd Internat. Cosmic Ray Conf., Calgary*, 1, 305

[2] Arendt, R. G., 1991, *Astron. J.*, 101(6), 2160

[3] Bennett, K., 1994, *Astrophys. J. Suppl.*, 90, 823

[4] van den Bergh, S. and Kamper, K. W., 1984, *Astrophys. J. Lett.*, 280, L51

[5] Brazier, K. T. S., *et al.*, 1994, *Mon. Not. R. Astron. Soc.*, 268, 517

[6] Buccheri, R., *et al.*, 1983, *Astron. Astrophys.*, 128, 245

[7] Caraveo, P. A., Mereghetti, S. and Bignami, G. F., 1994, *Astrophys. J. Lett.*, 423, 125

[8] Carramiñana, A. and Bennett, K., 1995, *Adv. Space. Res.*, 15, 5, (5)65

[9] Chadwick, P. M., *et al.*, 1997, *Proc. 25th Internat. Cosmic Ray Conf., Durban*, 3, 189

[10] Cheng, K. S., Ho, C. and Ruderman, M., 1986, *Astrophys. J.*, 300, 500

[11] Clark, D. H. and Caswell, J. L., 1976, *Mon. Not. R. astr. Soc.*, 174, 267

[12] Esposito, J. A., *et al.*, 1996, *Astrophys. J.*, 461, 820

[13] Fierro, J. M., 1995, PhD thesis, Stanford University

[14] Finley, J. P., *et al.*, 1998, *Astrophys. J.*, 493, 884

[15] Greiveldinger, C., *et al.*, 1995, *Astrophys. J.*, 454, 855

[16] Goldreich, P. and Julian, W. H., 1969, *Astrophys. J.*, 157, 869

[17] Hara, T., *et al.*, 1993, *Nucl. Inst. Meth. Phys. Res. A*, 332, 300

[18] Harding, A. K., 1990, *Nucl. Phys. B*, 14A, 3

[19] Harding, A. K., 1996, *Space Sc. Rev.*, 75, 257

[20] Harding, A. K., Baring, M. G. and Gonthier, P. L., 1997, *Astrophys. J.*, 476, 246

[21] Hayakawa, S., 1952, *Prog. Theor. Phys.*, 8, 571

[22] Hayami, Y., 1997, M.Sc thesis, Tokyo Institute of Technology

[23] Hayashida, N., *et al.*, 1994, *Phys. Rev. Lett.*, 73, 3491

[24] Hill, D. A. and Porter, N. A., 1961, *Nature*, 191, 690

[25] Hillas, A. M., 1985, *Proc. 19th Internat. Cosmic Ray Conf., La Jolla*, 3, 445

[26] de Jager, O. C., Swanepoel, J. W. H. and Raubenheimer, B. C., 1989, *Astron. Astrophys.*, 221, 180

[27] de Jager, O. C., 1988, *Astrophys. J.*, 329, 831

[28] de Jager, O. C., 1994, *Astrophys. J.*, 436, 239

[29] de Jager, O. C., *et al.*, 1996, *Astrophys. J.*, 457, 253

[30] de Jager, O. C. and Harding, A. K., 1992, *Astrophys. J.*, 396, 161

[31] Kaspi, V. M., *et al.*, 1994, GRO/radio timing data base, Princeton University.

[32] Kawai, N. and Tamura, K., 1996, in "Pulsars: Problems and Progress", ASP Conference series Vol105 eds. S. Johnston, M. A. Walker and M. Bailes, 367

[33] Kennel, C. F. and Coroniti, F. V., 1984, *Astrophys. J.*, 283, 694

[34] Kifune, T., *et al.*, 1995, *Astrophys. J. Lett.*, 438, L91

[35] Konishi, T., 1997, M.Sc. thesis, Kobe University

[36] Koyama, K., *et al.*, 1995, *Nature*, 378, 255

[37] Li, T. P. and Ma, Y. Q., 1983, *Astrophys. J.*, 272, 317

[38] Macomb, D. J., *et al.*, 1995, *Astrophys. J. Lett.*, 449, L99

[39] Manchester, R. N., Tuohy, I. R. and D'Amico, N., 1982, *Astrophys. J. Lett.*, 262, L31

[40] Marsden, D., *et al.*, 1997, preprint

[41] Matsuoka, T., 1997, M.Sc. thesis, Nagoya University

[42] Matz, S. M., 1994, *Astrophys. J.*, 434, 288

[43] Milne, D. K., Caswell, J. L. and Haynes, R. F., 1993, *Mon. Not. R. Astron. Soc.*, 264, 853

[44] Morrison, P., 1958, *IL Nuovo Cimento.*, 7, 858

[45] Nel, H. I., *et al.*, 1992, *Astrophys. J.*, 398, 602

[46] Ostriker, J. P. and Gunn, J. E., 1969, *Astrophys. J.*, 157, 1395

[47] du Plessis, I., *et al.*, 1995, *Astrophys. J.*, 453, 746

[48] Punch, M. B. E., 1993, PhD thesis, National University of Ireland

[49] Quinn, J., *et al.*, 1997, *Proc. 25th Internat. Cosmic Ray Conf., Durban*, 3, 249

[50] Ramanamurthy, P. V. and Wolfendale, A. W., 1993, in "Gamma-ray astronomy", Cambridge Univ. Press

[51] Ramanamurthy, P. V., et al,, 1995, *Astrophys. J. Lett.*, 447, L109

[52] Ramanamurthy, P. V., et al,, 1996, *Astrophys. J.*, 458, 755

[53] Rees, M. J. and Gunn, J. E., 1974, *Mon. Not. R. astr. Soc.*, 167, 1

[54] Roberts, M. D., *et al.*, 1998, in preparation

[55] Ruderman, M. A. and Sutherland, P. G., 1975, *Astrophys. J.*, 196, 51

[56] Sako, T., *et al.*, 1997, *Proc. 25th Internat. Cosmic Ray Conf., Durban*, 3, 193

[57] Seward, F. D. and Harnden, F. R., 1982, *Astrophys. J. Lett.*, 256, L45

[58] Seward, F. D., *et al.*, 1983, *Astrophys. J.*, 267, 698

[59] Seward, F. D., *et al.*, 1984, *Astrophys. J.*, 281, 650

[60] Shibata, S., 1996, Proceedings of '*Very High Energy Astrophysics*' Conference at Tokyo Metropolitan University, 49.

[61] Srinivasan, R., *et al.*, 1997, *Proc. 25th Internat. Cosmic Ray Conf., Durban*, 3, 205

[62] Standish, E. M., 1982, *Astron. Astrophys.*, 114, 297

[63] Susukita, R., 1997, PhD thesis, Kyoto University

[64] Swanenburg, B. N., *et al.*, 1981, *Astrophys. J. Lett.*, 243, L69

[65] Tamura, K., *et al.*, 1996, *PASJ*, 48, L33

[66] Tanimori, T., *et al.*, 1994, *Astrophys. J. Lett.*, 429, L61

[67] Tanimori, T., *et al.*, 1998, *Astrophys. J. Lett.*, 492, L33

[68] Taylor, J. H., Manchester, R. N. and Lyne, A. G., 1993, *Astrophys. J. Suppl.*, 88, 529

[69] Thompson, D. J., *et al.*, 1993, *Astrophys. J. Suppl.*, 86, 625

[70] Thompson, D. J., *et al.*, 1994, *Astrophys. J. Lett.*, 436, 229

[71] Thompson, D. J., *et al.*, 1995, *Astrophys. J. Suppl.*, 86, 629

[72] Thompson, D. J., *et al.*, 1996, *Astrophys. J. Suppl.*, 107, 227

[73] Thornton, G. J., *et al.*, 1994, in "Towards a Major Atmospheric Cerenkov Detector III, Tokyo, Japan(1994)", 125, ed. T. Kifune, University Academy Press, Inc.

[74] Thorsett, S. E., 1992, *Nature*, 356, 690

[75] Torii, K., 1997, presented at the "Neutron Stars and Pulsars" symposium (November, 1997) at Rikkyo University, Japan.

[76] Trussoni, E., *et al.*, 1996, *Astron. Astrophys.*, 306, 581

[77] Ulmer, M. P., *et al.*, 1993, *Astrophys. J.*, 417, 738

[78] Vacanti, G., *et al.*, 1991, *Astrophys. J.*, 377, 467

[79] Weekes, T. C., 1981, *Proc. 17th Internat. Cosmic Ray Conf., Paris*, 8, 34

[80] Weekes, T. C., *et al.*, 1989, *Astrophys. J.*, 342, 379

[81] Weekes, T. C., 1996, *Space Sc. Rev.*, 75, 1

[82] Wilson, R. B., *et al.*, 1993, in "Isolated Pulsars" ed. K. van Riper, R. Epstein and C. Ho, Cambridge Univ. Press, 257

[83] Yoshikoshi, T., 1996, PhD thesis, Tokyo Institute of Technology

[84] Yoshikoshi, T., *et al.*, 1997, *Astrophys. J. Lett.*, 487, L65